UNIVERSITY OF THESSALY
SCHOOL OF ENGINEERING
DEPARTMENT OF MECHANICAL ENGINEERING

Diploma thesis

Electrochemical sensors based on solid electrolytes for gas detection at high temperatures

by

Sidiropoulos Dimitrios

Supervisor

Prof. Tsiakaras Panagiotis

Submitted in partial fulfillment of the requirements for the degree of Diploma in Mechanical Engineering at the University of Thessaly

Volos, 2022

ΠΑΝΕΠΙΣΤΗΜΙΟ ΘΕΣΣΑΛΙΑΣ
ΠΟΛΥΤΕΧΝΙΚΗ ΣΧΟΛΗ
ΤΜΗΜΑ ΜΗΧΑΝΟΛΟΓΩΝ ΜΗΧΑΝΙΚΩΝ

Διπλωματική Εργασία

Ηλεκτροχημικοί αισθητήρες στερεού ηλεκτρολύτη για την ανίχνευση αερίων σε υψηλές θερμοκρασίες

υπό

Σιδηρόπουλος Δημήτριος

Επιβλέπων

Καθηγητής Τσιακάρας Παναγιώτης

Υπεβλήθη για την εκπλήρωση μέρους των απαιτήσεων για την απόκτηση του Διπλώματος Μηχανολόγου Μηχανικού

Βόλος, 2022

Εγκρίθηκε από τα μέλη της Τριμελούς Εξεταστικής Επιτροπής:

1st Examiner: Dr. Tsiakaras Panagiotis (Supervisor)
Professor
Department of Mechanical Engineering
School of Engineering
University of Thessaly

2nd Examiner: Dr. Charalampous Georgios
Assistant Professor
Department of Mechanical Engineering
School of Engineering
University of Thessaly

3rd Examiner: Dr. Brouzgou Angeliki
Assistant professor
Department of Energy systems
Faculty of Technology
University of Thessaly

ACKNOWLEDGMENTS

Initially, I would like to express my gratitude to Professor Panagiotis Tsiakaras for giving me the opportunity to investigate the present thesis. His effort, interest, guidance, support, and patience not only contributed to the accomplishment of the thesis but also help me to broaden my knowledge.

Moreover, I would like to thank the members of the examination committee, Dr. Angeliki Brouzgou and Dr. Georgios Charalampous, for reading and evaluating my thesis.

Lastly, I would like to express my gratitude to my beloved parents, Maria and Stefanos, for their love, encouragement, trust, and financial support during the formation of this thesis and throughout my studies at the Department of Mechanical Engineering in University of Thessaly.

ΕΥΧΑΡΙΣΤΙΕΣ

Πρώτα από όλα, θα ήθελα να εκφράσω την ευγνωμοσύνη μου στον καθηγητή κύριο Παναγιώτη Τσιακάρα για την ευκαιρία που μου έδωσε να ασχοληθώ με την παρούσα διπλωματική εργασία. Η προσπάθειά του, το ενδιαφέρον του, η καθοδήγησή του, η υποστήριξή του και η υπομονή του όχι μόνο συντέλεσαν στην ολοκλήρωση της εργασίας, αλλά με βοήθησαν στο να διευρύνω τις γνώσεις μου.

Επιπλέον, θα ήθελα να ευχαριστήσω τα μέλη της εξεταστικής επιτροπής Δρ. Αγγελική Μπρούζγου και Δρ. Γεώργιο Χαραλάμπους για τον χρόνο που αφιερώνουν για την μελέτη και την αξιολόγηση της εργασίας μου.

Τέλος, θα ήθελα να εκφράσω την ευγνωμοσύνη στους γονείς μου, Μαρία και Στέφανο, για την αγάπη του, την ενθάρρυνσή τους, την εμπιστοσύνη τους και την οικονομική και ηθική υποστήριξή τους κατά τη διάρκεια των σπουδών μου στο Τμήμα Μηχανολόγων Μηχανικών του Πανεπιστημίου Θεσσαλίας.

Abstract

The unprecedented technological achievements over the past two centuries have conspicuously raised our living standards. However, the strong dependence of humanity on fossil fuels (coal, oil, natural gas), which possess about 85 % of global energy sources, has created severe environmental issues. More precisely, the combustion of these fuels produces hazardous pollutants, specifically CO, CO_2, NO_x, SO_x, and hydrocarbons, which are responsible for health problems and environmental catastrophes (acid rain, greenhouse effect). Thus, the development of gas sensors able to detect these toxic gases directly after the combustion processes is among the issues of the highest importance. Electrochemical gas sensors are included in the widely used technologies that not only provide in situ information about the target gas content but also contribute to the optimization of combustion processes.

In the present thesis, the electrochemical gas sensors that use solid electrolytes for the detection of combustible gases at high temperatures are presented. The first chapters describe basic concepts of electrochemistry, such as the electrochemical cell, potential difference, and Nernst equation. In addition, the fundamentals of solid electrolytes are discussed, focusing on oxygen ion and proton conductors. The 4^{th} chapter contains a brief description of existing electrochemical devices used for energy production and storage (fuel cells, batteries, and capacitors). Last, some of the widely used experimental techniques, specifically electrochemical and physicochemical techniques that are employed for the characterization of a studied device are presented. The last three chapters are devoted to electrochemical gas sensors, analyzing principles and different types. Next, the solid-state electrochemical sensors detecting combustible gases, such as CO, CO_2, and hydrocarbons, are reviewed. Last, emphasis is given to hydrogen gas sensors based on solid electrolytes for high-temperature detection. The discussed sensors operate at high temperatures and are analyzed through I-V curves.

ΠΕΡΙΛΗΨΗ

Τα άνευ προηγουμένου τεχνολογικά επιτεύγματα των τελευταίων 2 αιώνων έχουν αυξήσει αισθητά το ανθρώπινο βιοτικό επίπεδο. Ωστόσο, η ισχυρή εξάρτηση του ανθρώπου από τα ορυκτά καύσιμα (άνθρακας, πετρέλαιο, φυσικό αέριο), τα οποία καταλαμβάνουν το 85% των παγκόσμιων ενεργειακών πηγών, έχει δημιουργήσει σοβαρά περιβαλλοντικά ζητήματα. Ειδικότερα, η καύση αυτών των ορυκτών καυσίμων παράγει επικίνδυνους ρύπους, συγκεκριμένα CO, CO_2, NO_x, SO_x και υδρογονανθράκων, είναι υπεύθυνη για προβλήματα στην ανθρώπινη υγεία και για περιβαλλοντικές καταστροφές (όξινη βροχή, φαινόμενο του θερμοκηπίου). Συνεπώς, η ανάπτυξη αισθητήρων αερίων που είναι ικανοί να ανιχνεύσουν τοξικά αέρια απευθείας μετά την διεργασία της καύσης είναι ανάμεσα στα ύψιστης σημασίας ζητήματα. Οι ηλεκτροχημικοί αισθητήρες αερίων είναι μία τεχνολογία που χρησιμοποιείται ευρέως, παρέχοντας πρωτίστως επιτόπου πληροφορίες για την σύσταση του εξεταζόμενου αερίου αλλά και συμβάλλοντας στην βελτιστοποίηση της διεργασίας της καύσης.

Η παρούσα διπλωματική εργασία ασχολείται με τους ηλεκτροχημικούς αισθητήρες στερεού ηλεκτρολύτη για την ανίχνευση αερίων που παράγονται από την διεργασία της καύσης σε υψηλές θερμοκρασίες. Τα πρώτα κεφάλαια περιγράφουν τις βασικές ιδέες της ηλεκτροχημείας, όπως το ηλεκτροχημικό κελί, τη διαφορά δυναμικού και την εξίσωση του Νερνστ. Επιπλέον, περιγράφονται οι αρχές που διέπουν τους στερεούς ηλεκτρολύτες εστιάζοντας στους αγωγούς ιόντων οξυγόνου και υδρογόνου. Το 4^{ο} κεφάλαιο περιέχει μια σύντομη περιγραφή των ηλεκτροχημικών συσκευών για την παραγωγή και αποθήκευση ενέργειας (κυψέλες καυσίμων, μπαταρίες, πυκνωτές). Στο τέλος των εισαγωγικών κεφαλαίων παρουσιάζονται κάποιες από τις πλέον χρησιμοποιημένες πειραματικές μεθόδους, συγκεκριμένα οι ηλεκτροχημικές και φυσικοχημικές μέθοδοι, για την ανάλυση μιας συσκευής. Τα τελευταία 3 κεφάλαια αφιερώνονται στους ηλεκτροχημικούς αισθητήρες αερίων αναλύοντας τις αρχές τους και τα διαφορετικά είδη. Εν συνεχεία, παρουσιάζονται οι ηλεκτροχημικοί αισθητήρες στερεού ηλεκτρολύτη για την ανίχνευση αερίων όπως CO, CO, CO_2 και υδρογονανθράκων. Τέλος, δίνεται έμφαση δίνεται στους αισθητήρες στερεού ηλεκτρολύτη για την ανίχνευση υδρογόνου σε υψηλές θερμοκρασίες. Όλοι οι αισθητήρες που αναλύονται στην παρούσα διπλωματική εργασία λειτουργούν σε υψηλές θερμοκρασίες και αναλύονται με βάση τα διαγράμματα τάσης-ρεύματος.

TABLE OF CONTENTS

List of tables

List of figures

Chapter 1

Introduction

1.1 Importance of gas sensors

Since the industrial revolution, the fields of technology and science have made colossal strides, raising noticeably our living standards. On the other side of the coin, several environmental issues have occurred together with these developments. Gaseous pollutants, such as NO_x, SO_x, CH_4, CO_2, and CO released from industrial processes and automobiles, are responsible for detrimental phenomena such as the greenhouse effect and acid rain. Hence, devices that can detect these hazardous gases are essential for environmental safety and human health. Along with the reduced emissions, there is a need for energy saving due to the limited fossil fuel reserves. Gas sensors analyze in real time the composition of combustion emissions contributing to the optimization of the combustion process.

Several industrial fields, such as power generation, metallurgy, automotive, and petrochemical, require sensors able to work effectively in harsh environments. These environments are characterized by high temperatures and pressures, corrosive conditions, and high velocities of exhaust fumes. High-temperature gas sensors play a vital role in these operating systems because they can monitor the combustion process under aggressive environments. The products of combustion contain hazardous gases, forcing the governments to implement austere policies concerning the limits of these emissions. For this reason, the development of robust and miniaturized gas sensors with decent thermal stability and high sensitivity is a challenge of paramount importance [1].

1.2 Solid-state gas sensors

The global energy crisis and the environmental footprint of fossil fuels have created an unprecedented demand for cleaner energy production and storage. Following this line, electrochemical devices for energy production and storage, such as fuel cells, batteries, as well as electrochemical gas sensors for controlling emissions, offer a suitable solution for tackling these problems. Despite the development of technology and science, many steps are required for reaching an optimal solution. The further development of these devices is inextricably bound up with the properties and the features of materials applied to them. Electrolytes are of great significance in the operation of electrochemical devices, as they support the movement of ions and block the movement of electrons through them, preventing the creation of short circuits. Liquid electrolytes are usually applied in electrochemical devices due to their high ionic conductivities. However, solid electrolytes have been extensively studied in the last decades resulting in their exponential growth. Solid electrolytes tend to replace liquid electrolytes in several electrochemical devices, such as gas sensors, batteries, and fuel cells, as they can achieve ionic conductivities commensurate with those of applied liquid electrolytes.

The utility of solid electrolytes in electrochemical gas sensors offers several advantages against other proton-conductive materials, including high sensitivity, simple operation, and real-time response. Additionally, they can combine high ionic conductivities with adequate thermal, thermodynamic, and mechanical stability in aggressive environments. Thus, serious environmental problems related to gas emissions can be addressed by the promising solid-state gas sensors technology. Their operation is based on an electrical signal which provides direct information about the target gas. The most famous and frequently used gas sensor is the oxygen sensor (lambda sensor), applied in gasoline vehicles for the past four decades. This sensor is conventionally employed with yttria-stabilized zirconia (YSZ) electrolyte and platinum (Pt) electrodes. YSZ is still the dominant solid oxide electrolyte due to its high stability and effectiveness. However, the spectacular improvement of technology along with extensive scientific research can lead to new solid electrolytes with better efficiency [2].

Chapter 2

Theoretical background

Abstract

In the present chapter, the theoretical background of two different scientific fields is described. Firstly, the basic concepts of electrochemistry such as the electrochemical cell, potential difference, Faraday's law, and Nernst's equation are presented. Subsequently, gas diffusion mechanisms are analyzed, focusing on application in porous media.

2.1 Fundamentals of electrochemistry

2.1.1 Introduction

Electrochemistry is the science investigating the relationship between chemical reactions and electron transfer at the electrolyte/electrode interface. Although electron was discovered in the late 19th century, Alessandro Volta has already laid the foundations of electrochemistry since 1800. In particular, he created the first battery consisting of copper and zinc plates separated by paper disks and soaked in acid solutions. By 1835, Michael Faraday had introduced essential notions of electrochemistry, such as cathode, anode, electrolyte, electrode, and ion. Currently, electrochemistry interests the scientific and industrial communities due to its sustainable applications, including fuel cells and electrochemical gas sensors [3].

2.1.2 Electrochemical cell

The electrochemical cell is the key element of every electrochemical application. It is a system that consists of electrodes and an electrolyte, where the electric current is generated by the chemical reactions taking place in the system or applied in the system to drive chemical changes. The voltaic and electrolytic cells are the two kinds of electrochemical cells. The distinction between the two kinds is that in the voltaic cell, a spontaneous chemical

reaction generates the electrical current, while in the electrolytic cell the electrical current is applied to activate a nonspontaneous chemical reaction.

The voltaic cell, also known as the galvanic cell, is a device producing electrical current via chemical energy. It comprises two half-cells that are electrically connected, allowing the movement of electrons from one half-cell to another via an external circuit. Each half-cell includes the anode and the cathode electrode, where the redox chemical reactions occur. Generally, electrons and ions are generated at the anode by the oxidation half-reaction. The electrons moving via the external circuit and the ions flowing through the electrolyte are transferred to the cathode to drive the reduction half-reaction [4].

Oxidation: Reductant agent⟶ Ox. Product $+e^-$

Reduction: Oxidant agent $+e^-$⟶ Red. Product

Redox: Reductant agent + Oxidant agent⟶ Ox. Product + Red. Product

Zinc-copper galvanic cell is a typical as well as an instructive example of a voltaic cell. This system is composed of a zinc electrode (anode), a copper electrode (cathode), and a salt bridge (electrolyte). The zinc electrode includes a solution of zinc salt, in which a zinc metal strip is dipped. Similarly, the copper electrode comprises a copper metal strip immersed in a solution of copper salt. Zinc is an element that has a stronger tendency to lose electrons than copper, so zinc atom oxidizes producing electrons and zinc ions. These electrons are transferred to the cathode (copper electrode), where they react with the copper ions forming copper metal atoms. However, the production of zinc ions and copper metal atoms creates a positive charge at the zinc electrode and a negative charge at the copper electrode, respectively. For this reason, the constant generation of electrical current requires the movement of positive ions from the zinc electrode to copper electrode and the movement of negative ions from copper electrode to zinc electrode. Salt bridge takes on this role operating like an electrolyte without mixing the two solutions. For instance, a salt bridge can contain K^+ and Cl^- to complete the electric circuit. The zinc-copper galvanic cell is demonstrated in **Figure 1a,** and the reactions regulating this system are [4]:

(Oxidation): $Zn(s) \rightarrow Zn^{2+}(aq) + 2e^-$ (2.1)

(Reduction): $Cu^{2+}(aq) + 2e^- \rightarrow Cu(s)$ (2.2)

(Overall reaction): $Zn(s) + Cu^{2+}(aq) \rightarrow Zn^{2+}(aq) + Cu(s)$ (2.3)

2.1.3 Potential difference and electromotive force

Generally, the movement of electric charge starts from a point of higher electric potential to a point of lower electric potential. The same phenomenon takes place in a pipe, where the water flows from a high-pressure point to a low-pressure point. Thus, the water in a pipe and the electric charge require a pressure difference and a potential difference to move, respectively. The potential difference, also known as voltage, can be defined as the difference in electric charge between two points and it is measured in volts (V). Additionally, the work required for the movement of an electric charge through a conductor is strongly associated with the potential difference and the total charge moved. On the other hand, the maximum potential difference measured across the electrodes of a galvanic cell is the electromotive force (EMF), or cell potential (E_{cell}). The potential difference between the electrodes during normal operation of the galvanic cell is less than the maximum expected (EMF). This happens due to the energy expenditure required for the movement of electric charge in a cell. The increase of current leads to a decrease in cell voltage, reflecting this expenditure. Therefore, the maximum value of a voltaic cell is achieved when no current flows through the cell. The electromotive force also expresses the efficiency of the cell reaction. This reaction is divided into the oxidation half-reaction and the reduction half-reaction. Consequently, the cell potential includes the contribution from the anode and the cathode. The former expresses the ability of the oxidation to lose electrons and the latter expresses the ability of the reduction to gain electrons. The Electromotive force of a galvanic cell operating under standard state conditions is called standard cell potential (E^0_{cell}). The standard cell potential is given by the equation [4]:

$$E^0_{cell} = E^0_{cathode} - E^0_{anode} \tag{2.4}$$

2.1.4 Nernst's equation

In electrochemistry, Nernst's equation is of paramount importance because it correlates the cell potential to the concentration of electroactive species. Generally, the redox reactions taking place in a cell can be expressed by the following formula,

$$O + ne^- \leftrightarrows R \tag{2.5}$$

where O and R are the oxidized and reduced species respectively, and n is the number of electrons involved in the reaction. The concentration of oxidized and reduced species is related to the free energy change ΔG, by the equation (2.6),

$$\Delta G = \Delta G^0 + R \cdot T \cdot \ln \frac{[R]}{[O]} \quad (2.6)$$

where ΔG^0 is the standard free energy-change, R ($8.314 \frac{\mathrm{J}}{\mathrm{mol}^{-1}} \cdot \mathrm{K}^{-1}$) is the gas constant, and T the is the absolute temperature. It is known that the maximum useful work of a reaction, namely the electrical work in the case of a voltaic cell, equals the free energy change. This relationship is expressed by the following equation under standard conditions,

$$\Delta G^0 = -n \cdot F \cdot E^0_{cell} \quad (2.7)$$

where F is Faraday's constant (96,485 C/mol e^-) and E^0_{cell} is the standard cell potential. Consequently, Nernst's equation occurs by combing the equations (2.5-2.7). It is a well-known mathematical expression that is frequently used to calculate the cell potential or the concentrations of unknown species [3,4].

$$E_{cell} = E^0_{cell} + \frac{R \cdot T}{n \cdot F} \cdot \ln \frac{[O]}{[R]} \quad (2.8)$$

2.1.5 Faraday's law

Faraday's law affiliates the amount of total electric charge, Q, passed through a cell with the amount of produced substance N[mol]. It is given by the equation,

$$Q = n \cdot F \cdot N \quad (2.9)$$

where n is the total number of electrons moving in the cell per mole of product. This law has several practical applications even in industry. For instance, it can be used for the calculation of the electric charge needed for electrolysis of a compound (coulometry) and the amount of the product deposited at electrodes (electrogravimetry) [3].

2.1.6 Kinetics

Overpotential

Overpotential is defined as the difference between the applied potential (E) and the equilibrium potential (E_{eq}). It is given by the equation [3]:

$$\eta = E - E_{eq} \quad (2.10)$$

Butler-Volmer equation

Butler-Volmer equation correlates the current of a system with the overpotential, and it is expressed by the equation,

$$i = i_0 \cdot \left(exp\left(\frac{a_a \cdot F \cdot \eta \cdot z}{R \cdot T}\right) - exp\left(-\frac{a_c \cdot F \cdot \eta \cdot z}{R \cdot T}\right)\right) \quad (2.11)$$

where i [A/cm^2] is the current density, i_0 is the exchange current density, η is the overpotential, z is the number of transferred electrons, α_a, α_c are the charge transfer coefficients for the anode and cathode, respectively. Additionally, R, T, F are the gas constant, absolute temperature, and Faraday's constant, respectively. The exchange current density expresses the state at which the rates of the two half-cell reactions (oxidation and reduction) are equal. In an electrochemical cell, this happens at equilibrium (open-circuit conditions, η=0) because there is no net current and thus, the current of the anode equals the current of the cathode ($i_0=i_a=i_c$). Generally, in the case of one-electron transfer: $z = 1$ and $a_a + a_c = 1$ [3,5].

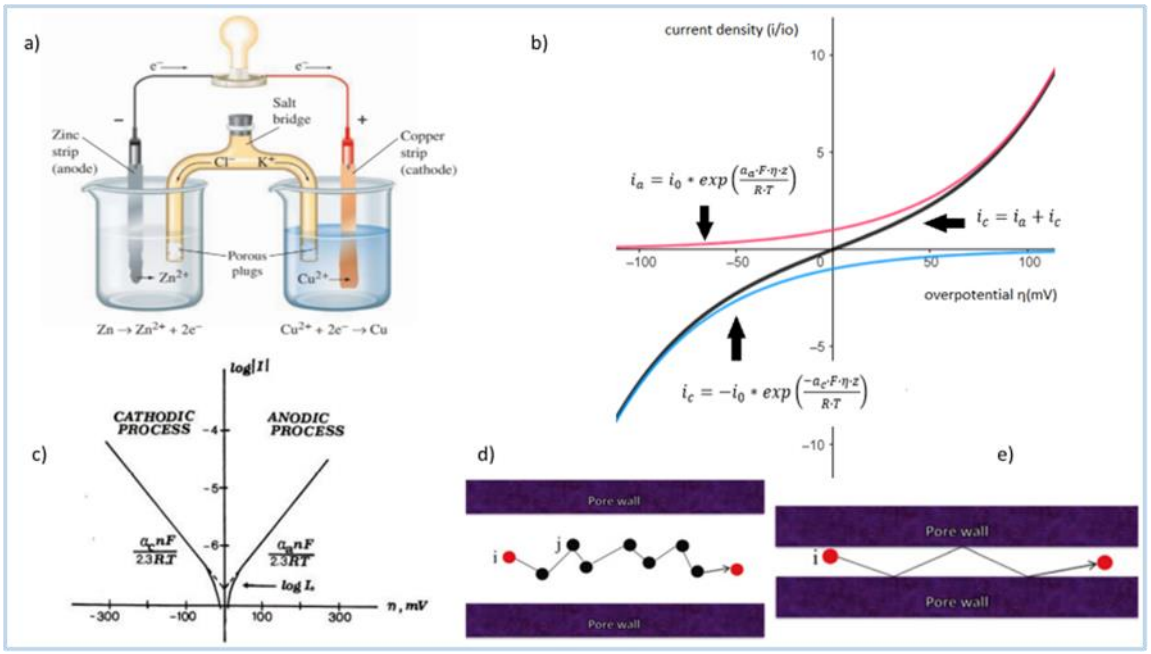

Figure 1: a) Schematic illustration of a zinc-cooper galvanic cell [4]; **b)** The current density plotted against overpotential, according to the Butler-Volmer equation [3]; **c)** Tafel's plot with the slopes of oxidation and reduction [3]; **d)** Schematic illustration of molecular diffusion [6] and **e)** Schematic representation of Knudsen diffusion [6].

According to the Butler-Volmer equation, the current density can be expressed as the algebraic sum of the anodic current i_a and the cathodic current i_c, (equations (2.12-2.14)). The behavior of Butler-Volmer equation is represented in **Figure 1b** for $a_a = a_c = 0.5$ and $T = 298K$. Thus, for positive overpotential (η>50mV) the current density increases exponentially, and the anodic current dominates. Similarly, for negative overpotentials (η<50mV) the current density decreases exponentially, and the cathodic current dominates [3,5].

$$i = i_a + i_c \quad (2.12)$$

$$i_a = i_0 * exp\left(\frac{a_a \cdot F \cdot \eta \cdot z}{R \cdot T}\right) \quad (2.13)$$

$$i_c = -i_0 * exp\left(\frac{-a_c \cdot F \cdot \eta \cdot z}{R \cdot T}\right) \quad (2.14)$$

Tafel equation

The total current corresponds to the anodic current or the cathodic current when the overpotential is big in magnitude. Thus, the equation (2.11) can be redefined using the logarithms, as is shown in equations (2.15-2.16). Tafel's equation occurs by solving the equations (2.15-2.16) for overpotential (2.17). In addition, this equation can also be expressed in the form of the equation (2.18). Tafel's plot is the graphic illustration of $\log|i|$ against overpotential (η), and it is used for the calculation of the exchange current density and the transfer coefficients (**Figure 1c**).

$$\ln i = \ln i_0 + \frac{a_a \cdot F \cdot \eta}{R \cdot T} \quad \eta \gg 0 \quad (2.15)$$

$$ln\, i = ln\, i_0 + \frac{a_c \cdot F \cdot \eta}{R \cdot T} \quad \eta \ll 0 \quad (2.16)$$

$$\eta = \frac{R \cdot T}{a \cdot F} \ln i - \frac{R \cdot T}{a \cdot F} \ln i_0 \quad (2.17)$$

$$\eta = \alpha + b * \log i \quad (2.18)$$

$$\alpha = -\frac{R \cdot T \cdot 2.3 \log i_o}{a \cdot F} \quad (2.19)$$

$$b = \frac{R \cdot T \cdot 2.3}{a \cdot F} \quad (2.20)$$

Tafel's plot contains an anodic and a cathodic branch for positive and negative overpotentials respectively, as is shown in **Figure 1c**. The constants α_c, α_α can be calculated by the oxidation and reduction slopes of the Tafel region, which contains big in magnitude overpotentials. Additionally, the exchange current density can be calculated by finding the y-intercept of the linear regions [3,5].

$$\text{Oxidation slope} = \frac{a_a \cdot F \cdot \eta}{2.3RT} \quad (2.21)$$

$$\text{Reduction slope} = \frac{-a_c \cdot F \cdot \eta}{2.3RT} \quad (2.22)$$

For small values of overpotential ($|\eta| < 100mV$), there is a linear correlation between the current density and the overpotential. Thus, the Butler-Volmer equation can be expressed as [3,5],

$$i = \frac{i_0 (a_a + a_c) F \eta}{RT} \quad (2.23)$$

2.2 Diffusion gas in porous media

2.2.1 Introduction

Gas diffusion is directly involved in the operation of electrochemical devices, such as fuel cells and solid-state gas sensors. The diffusion of gas molecules is a crucial parameter for the response rate of many types of gas sensors. The diffusion barrier of these sensors controls the quantity of gas reaching the electrodes and thus plays a key role in the generated current. During the diffusion through the porous media, the gas molecules collide with the porous media and interact with each other. There are three mechanisms characterizing the gas diffusion depending on the type of diffusing gas and the microstructure of the porous media. These mechanisms are Knudsen diffusion, molecular diffusion, and mixed diffusion. Knudsen number (K_n) is conventionally used to identify the mechanisms that govern gas diffusion. It is given by the equation (2.24), where λ is the gas mean free path and d_p is the diameter of the porous medium. The gas mean free path is calculated by the equation (2.25), where k_B is the Boltzmann constant ($1.3807 \cdot 10^{-27} J/K$), T is the gas absolute temperature, P is the gas pressure, and d_g is the effective diameter of the diffusing gas molecule [6].

$$K_n = \frac{\lambda}{d_p} \tag{2.24}$$

$$\lambda = \frac{k_B T}{\sqrt{2\pi} P d_g^2} \tag{2.25}$$

Consequently, Knudsen diffusion entirely characterizes the gas transport for values of Knudsen number higher than 10. On the other hand, the molecular diffusion dominates at $K_n << 0.1$, as the collisions between gas molecules prevail over these between the porous media and the gas molecules. Lastly, all the mechanisms are involved in the gas diffusion at $0.1 < K_n < 10$.

Gas diffusion is also described in several mathematical models. Among them, Fick's law is the simplest and simultaneously the most important model. Generally, diffusion is advanced from areas with high gas concentrations to areas with low gas concentrations. The diffusion flux is related to the concentration gradient by Fick's law which is expressed by the equation (2.26),

$$J = -D \frac{dC}{dx} \tag{2.26}$$

Where C is the gas concentration, x is the position, J is the diffusion flux, and D is the diffusion coefficient. Concerning applications involving porous media, the diffusion coefficient is usually replaced by a diffusion coefficient that contains porous media factors. The effective diffusivity (D^{eff}) is shown in equation (2.27), where φ is the porosity factor, τ is the tortuosity factor of the porous medium and D is the binary diffusivity [6].

$$D^{eff} = \frac{\varphi}{\tau} D \tag{2.27}$$

2.2.2 Molecular diffusion

Molecular diffusion expresses the interaction between gas molecules and occurs when the Knudsen number is less than 0.1. As it is presented in **Figure 1d**, the pore diameter is at least one order greater than the gas mean free path, resulting in pure molecular diffusion. Thus, the binary diffusivity of the equation (2.28) is calculated by the Chapman-Enskog theory [6],

$$D_{ij} = \frac{0.00186 T^{\frac{3}{2}}}{\sigma_{ij}^2 p \Omega} \sqrt{\frac{1}{M_i} + \frac{1}{M_j}} \tag{2.28}$$

Where p is the absolute pressure, T is the absolute temperature, σ is the collision diameter of gas species, Ω is the collision integral and M is the molecular weight.

2.2.3 Knudsen diffusion

Knudsen diffusion is the dominant mechanism if the pore diameter is at least one order smaller than the gas mean free path. As it is shown in **Figure 1e**, small pore diameter and low pressure are required for the domination of pure Knudsen diffusion [6]. The diffusivity of this mechanism is calculated by the equation (2.29),

$$D_{iK} = \frac{d_p}{3} \sqrt{\frac{8RT}{\pi M_i}} \tag{2.29}$$

In the case of mixed diffusion, namely at Knudsen number ($0.1 < K_n < 10$), both diffusivities of the equations (2.28) and (2.29) must be included in the calculation of the diffusion coefficient [6].

$$\frac{1}{D_i^m} = \frac{1}{D_{ij}} + \frac{1}{D_{iK}} \tag{2.30}$$

Chapter 3

Solid electrolytes

Abstract

In the third chapter, solid electrolytes are thoroughly analyzed in terms of their history, characteristics, and ionic conductivity. Additionally, different types of solid electrolytes are presented according to the types of mobile ions that conduct. The analysis of the present chapter is mainly focused on oxygen ion conductors and proton conductors. More precisely, oxygen-conducting solid electrolytes such as zirconia-based materials, ceria-based materials, and perovskites are discussed. Concerning proton conductors, $BaCeO_3$-based materials and $BaZrO_3$-based materials are reported.

3.1 Introduction

Solid electrolytes play a vital role in the development of solid-state electrochemistry. Solid materials with high ionic conductivity in conjunction with zero or almost zero electronic conductivity are used as solid electrolytes. They are also called fast, superionic, or optimized ion conductors. Solid electrolytes gather momentum because they can show ionic conductivity as high as in liquid electrolytes or molten salts. For this reason, applications such as solid-state batteries, high-temperature fuel cells, high-temperature gas sensors, and supercapacitors tend to replace liquid electrolytes with solid-state electrolytes. The investigation and technology of solid electrolytes is included in the field of solid-state ionics [7,8].

3.2 History

Michael Faraday laid the foundation of solid-state ionics by reporting conductivity in inorganic solids in 1833. Specifically, he discovered that the electrical conductivity of Ag_2S (silver sulfide) and PbF_2 (lead fluoride) increases with the temperature increase. This phenomenon was inconsistent with the behavior of the metallic phase, so it was almost

impossible to be explained at this time. Hittorf in 1851, based on Faraday's observations, studied the conductivity of Cu_2S (copper sulfide) and Ag_2S (silver sulfide) and concluded that an electrolytic conduction mechanism takes place in these materials during current flow. In 1884, Emil Warburg observed the transfer of sodium ions through a soda-lime glass, proving that ion conductivity exists in a solid [9, 10, 11].

The first commercially produced device utilizing solid electrolytes was invented by Walther Nernst in 1897. In particular, he patented an electric lighting device, later named the Nernst lamp that gave an impressive daylight spectrum. The principle of operation is based on Nernst's observation that a ceramic material could conduct electricity at high temperatures. The working body included a ceramic rod able to emit light by the passage of a current after sufficient preheating. Nernst experimented on several materials concluding that the mixed oxides show much higher conductivity than pure oxides at elevated temperatures. Thus, the well-known yttria-stabilized zirconia, with the composition of 85% ZrO_2 and 15% Y_2O_3, was efficiently used as a conductor. The contribution of Nernst to the science of solid oxide electrolytes is tremendous, given that YSZ is still employed in electrochemical devices operating at high temperatures. Although the Nernst lamp could function in ambient air, with no vacuum requirements, it was not convenient in use as it had to be preheated. The nature of the current in this lamp was unknown as there wasn't sufficient knowledge about the mobile species. The belief that the current in such ceramic materials (solid oxide electrolytes) occurs due to ions transport, was embraced after decades. Ultimately, the introduction of the Edison lamp in 1905 displaced the Nernst lamp [9, 10, 11].

In 1943, Carl Wagner identified the conduction mechanism of the Nernst lamp by finding oxygen vacancies in YSZ. These vacancies, formed by yttria additions in ZrO_2, provide the path for the movement of ions. In the 1950s, the first solid-state cells were developed using zirconia stabilized by yttrium oxide or calcium oxide as a solid electrolyte. In 1957, Kiukkola and Wagner first studied the thermodynamic properties of galvanic cells that employ these ceramic materials [12, 13]. The scientific research of this decade gave an important impulse to the progress of zirconia-based electrolytes (oxygen ion conductors) operating at high temperatures. Thus, Ruka and Weissbart, in 1961, patented the first device (oxygen gauge) for the measurement of oxygen using the abovementioned materials in a high-temperature electrochemical cell. [11,14].

Except for oxygen ion conductors, several families of materials that exhibit ionic conductivity with different types of ions were under investigation. For instance, Yao and

Kummer, in 1961, suggested the sodium ion-conducting membrane beta-alumina as a solid electrolyte in sodium-sulfur batteries. Additionally, many more solid electrolytes were discovered in this period, with glasses and polymers being the most important [15].

Proton-conducting electrolytes are included in the latest and most promising discoveries. Historically, Iwahara et al. paved the way by reporting noticeable proton conductivity in doped $LaYO_3$ and $SrZrO_3$ in the 1980s. They also revealed this phenomenon in $SrCeO_3$ doped with Mg, Yb, or Sc. Subsequently, in 1985, Mati and Virkar observed pure ionic conduction in Y-doped and pure $BaCeO_3$ at $Po_2<10^{-6}$, with temperature ranging from 600°C to 1000°C [16]. In 1987, proton conduction was also detected by Mitsui et al. in $BaZr_{0.95}Yb_{0.05}O_{3-\delta}$ and $BaCe_{0.95}Yb_{0.05}O_{3-\delta}$ [17, 18].

3.3 Requirements of a solid electrolyte

Solid electrolytes must meet numerous criteria to be appropriate for application in electrochemical devices. Initially, they must act as a passage for the movement of ions between electrodes. The electrochemical reaction is the driving force that generates or consumes electrons and ions at electrodes. The electrons flow through an external circuit while the ions pass through the electrolyte to maintain charge balance. The ability of an electrolyte to support the ionic current is expressed by the ionic conductivity measured in $S \cdot cm^{-1}$ (S=Siemens) or $ohm^{-1} \cdot cm^{-1}$. The values of ionic conductivity in solid electrolytes range from 10^{-5} $S \cdot cm^{-1}$ to 1 $S \cdot cm^{-1}$ at high temperatures, as it is shown in **Figure 2a**. These values are appreciably low compared with the conductivities of metals in which the electrons carry the current. Generally, an adequate solid electrolyte must show high ionic conductivity, above 10^{-3} $S \cdot cm^{-1}$, at operating temperatures. For instance, a solid electrolyte in SOFCs should exhibit conductivity of approximately 10^{-2} S/cm at 700°C [19, 20, 21].

Additionally, solid electrolytes should present chemical stability in oxidizing and reducing atmospheres and, simultaneously, must be thermodynamically stable over a broad range of operating temperatures and Po_2. It is also important to be electronic insulators because the existence of electronic conduction in the electrolyte can deteriorate the operation of electrochemical devices. Furthermore, the thermal expansion of solid electrolytes must be low and commensurate with that of electrodes and the rest materials of the electrochemical device. Hittorf number is also a parameter that characterizes a solid electrolyte. It is expressed by a fraction in which the numerator is the charge transported by an ion (σ_{ion}) and the denominator is the total charge passed through the electrolyte (σ_{total}). The ionic species must carry the total

charge in solid electrolytes, so this number must be unity [22, 23]. Hittorf number is given by the equation (3.1),

$$t_i = \sigma_i / \sigma_{total} \tag{3.1}$$

3.4 Ionic conductivity

Ionic conductivity in solid occurs due to the movement of ions under the influence of a voltage. It differs from electrical conductivity in terms of the type of species that carries the current, but their magnitude is calculated by the same equation.

$$\sigma = nZe\mu \tag{3.2}$$

where n, Z·e, and μ are the number of charge carriers per unit volume, the charge and the ion mobility, respectively. The movement of ions through the crystal structure of solid electrolytes is feasible due to the defects existing in every crystal. Among the different types of defects, two types are of paramount significance for ion mobility in crystals. The first type is Schottky defects, which include vacant sites in the lattice, and the second type is Frenkel defects, where an ion creates a vacancy by its movement in an interstitial position. These types of defects are also categorized as point defects [24, 25].

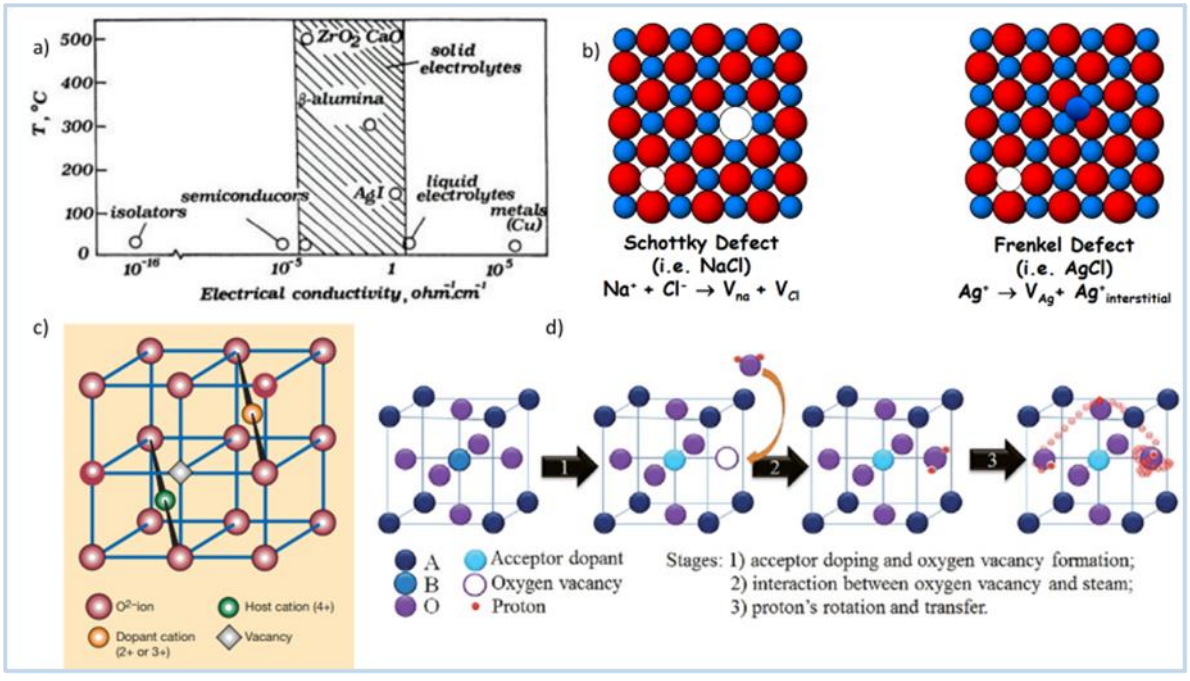

Figure 2: **a)** Conductivities of solid electrolytes, metals and liquid electrolytes at the corresponding temperature [19]; **b)** Schematic illustration of Schottky and Frenkel defect [26]; **c)** Formation of oxygen vacancy in solid oxides [19] and **d)** The stages for the accomplishment of proton conduction in the ABO_3 perovskite structure [29].

Schottky defects comprise pairs of vacancies formed by the detachment of pairs of ions (cations and anions) from the crystal. Frenkel defects include vacancies created by single ions leaving their regular sites but, contrary to Schottky defects, the ions move into an interstitial position in the crystal. As **Figure 2b** shows, NaCl and AgCl are two typical examples of solids in which Schottky and Frenkel defects take place, respectively. It is also remarkable that at a specific temperature, the number of point defects in a crystal can be estimated by the equations:

Schottky defects: $$n_s = N \cdot exp\left(\frac{-\Delta H_s}{2RT}\right) \quad (3.3)$$

Frenkel defects: $$n_F = (N \cdot N_i)^{1/2} \cdot exp\left(\frac{-\Delta H_F}{2RT}\right) \quad (3.4)$$

where n_s, n_F, N, and N_i are the number of Schottky defects, the number of Frenkel defects, the number of available lattice sites, and the number of available interstitial sites, respectively. ΔH_S, ΔH_F are the enthalpies required for the formation of one mole of Schottky and Frenkel defect, respectively. T is the temperature and R is the gas constant [24, 25, 26].

The ionic conductivity in a solid is affected by several factors such as the temperature, the concentration of charge carriers, the availability of defects in the crystal and the activation energy. The latter expresses the energy frontier required to be surpassed by an ion, for a successful jump from one site to another. These factors are correlated by the Arrhenius equation. This equation indicates that the activation energy has a considerable influence on the ionic conductivity due to its exponential dependence. Additionally, it confirms the strong dependence between the ionic conductivity and the temperature, with the former increasing as the temperature also increases. Arrhenius expression is given by the equation:

$$\sigma = \frac{A}{T} exp\left(\frac{-E_a}{kT}\right) \quad (3.5)$$

where E_α is the activation energy, k is the Boltzmann's constant, σ is the ionic conductivity, and T is the temperature. The pre-exponential factor (A) expresses all the remaining parameters affecting the ionic conductivity [25].

3.4.1 Oxide ion (O^{2-}) conductivity

Oxygen ion conductivity in solid electrolytes results due to the movement of oxide ions in the crystal lattice. Oxygen ions migrate in the vacant sites of the crystal through thermally activated jumps directed by the applied electric field. This process requires an equilibrium

between unoccupied sites and occupied oxygen ion sites in the crystal. In addition, the energy barrier for a successful jump of an oxygen ion in a vacant site must be insignificant, namely, less than about 1 eV. Solid oxide electrolytes have gained substantial interest due to their conductivities at high temperatures. Specifically, they can approach high values, close to 1 S/cm, which are commensurable with those of liquid electrolytes [27].

Oxygen vacancies, which are the path of oxygen ions in the crystal, are formulated by substituting the host cation of the lattice with an aliovalent cation. Specifically, as it is shown in **Figure 2c**, the substitution of a host cation (such as Zr^{4+}) with a lower-valent cation (such as Y^{3+}) creates a missing charge. Thus, an oxygen vacancy is formed to balance this charge. Yttria-stabilized zirconia (YSZ) is a representative example of this process formulated by doping Yttrium oxide (Y_2O_3) into Zirconium dioxide (ZrO_2) [27, 28].

3.4.2 Proton (H^+) conductivity

The comprehension of the proton transfer mechanism in oxide materials arises from the features of protons. Firstly, protons (H^+) are elementary particles forming covalent bonds with atoms and ions having negative charges, such as oxygen ions in oxides. Secondly, they are shared between two negatively charged atoms formulating bonds like O–H···O. In solids, free protons cannot occur under equilibrium conditions due to their strong tendency to interact with electronegative oxygen ions. Thus, the realization of proton transport in high-temperature proton conductors (HTPCs) requires the breaking of the O-H bond. This process can be performed by a thermally activated hopping mechanism, also known as the Grotthuss mechanism. According to this mechanism, the proton transport process can be divided into two steps. The first step includes the rapid rotation of the proton around the oxygen ion and the second step includes the proton jump in a neighboring oxygen ion. The first stage is easier to be accomplished due to the low activation barrier (below 0.1 eV). On the other hand, the second stage requires activation energy, about 0.5 eV, constituting the rate determining step of proton migration [18, 29].

Oxygen vacancies in oxides play a vital role in terms of proton conductivity. These vacancies can exist in the crystal structure of the oxide (structural defects), or they can be introduced by acceptor doping (impurity defects). As it is shown in **Figure 2d**, the oxygen vacancies interact with water steam forming new structural elements:

$$H_2O + V_O^{\cdot\cdot} + O_O^x = 2OH_O^{\cdot} \tag{3.6}$$

where $V_O^{\cdot\cdot}$ is the oxygen vacancy, O_O^x is the oxide ion of the crystal structure, and $OH_O^{\cdot}$ is the proton defect. For instance, in a notable proton conducting material, Y-$BaZrO_3$, the oxygen vacancies are created by acceptor, according to the following reaction [18, 29],

$$Y_2O_3 \xrightarrow{BaZrO_3} 2Y'_{Zr} + V_O^{\cdot\cdot} + 3O_O^x \quad (3.7)$$

3.5 Classification of solid electrolytes

Nowadays, electrochemical devices using solid electrolytes constitute a field with growth potential. Thus, a plethora of solid-state materials showing sufficient ionic conductivity is under thorough investigation. Generally, a solid electrolyte can be classified into many categories concerning the type of mobile ions, the substances, and the defect chemistry. Focusing on the nature of mobile ions, a solid electrolyte can be; i) a cation conductor (Li^+, Na^+, Ag^+), ii) an anion conductor (O^{2-}, F^-), or iii) a proton conductor (H^+) [30].

3.5.1 Oxygen ion (O^{2-}) conductors

Fluorite structured oxides

Among the materials that exhibit oxygen ion conductivity, the fluorite structure oxides are the most widespread and reliable concerning applications as electrolytes in electrochemical devices. These materials, with the general formula AO_2, are composed of a cubic oxygen lattice and a large tetravalent cation such as thorium, cerium, or uranium, forming ThO_2, CeO_2 and UO_2, respectively. Additionally, the zirconium dioxide (ZrO_2) can sustain the fluorite structure, but only either at high temperatures or by partial substitution of zirconium with an aliovalent cation. The latter process (doping) ensures charge neutrality and, simultaneously, introduces oxygen vacancies in the lattice, accomplishing an essential requirement for the presence of ionic conductivity in the crystal. Generally, alkaline earth oxides such as (MgO, CaO) or rare earth oxides such as (Y_2O_3, Sc_2O_3) are doped in zirconium dioxide creating solids that present high ionic conductivity [27, 31].

Yttria-stabilized zirconia (YSZ) is an extremely widespread ion conducting material applied in electrochemical devices such as oxygen sensors, solid oxide fuel cells (SOFCs) and solid oxide electrolysis cells (SOECs). This extensive use arises from its high oxygen ion conductivity as well as its thermal and chemical stability, mainly at elevated temperatures. For instance, the temperature range of SOFCs (1200°C-1500°C) makes YSZ the appropriate choice for application as a solid electrolyte. The oxygen vacancies, essential for the movement of oxide ions through the crystal, are created by the dissolution of Y_2O_3 in ZrO_2

(**Figure 3a**). In particular, an oxygen vacancy is generated in order to balance the charge for two Y^{3+} replacing a Zr^{4+} site. This process is expressed by the reaction,

$$Y_2O_3 \xrightarrow{ZrO_2} 2Y'_{Zr} + V_O^{\cdot\cdot} + 3O_O \tag{3.8}$$

As it is observed in **Figure 3b**, the ionic conductivity peaks at low concentrations of Y_2O_3, regardless of the operating temperature. Consequently, 8% mol Y_2O_3 (8YSZ) has prevailed over the Y-Zr ratios in electrochemical devices, showing ion conductivity of about 0.1-0.2 S/cm at 1000°C-1200°C [31, 32, 33].

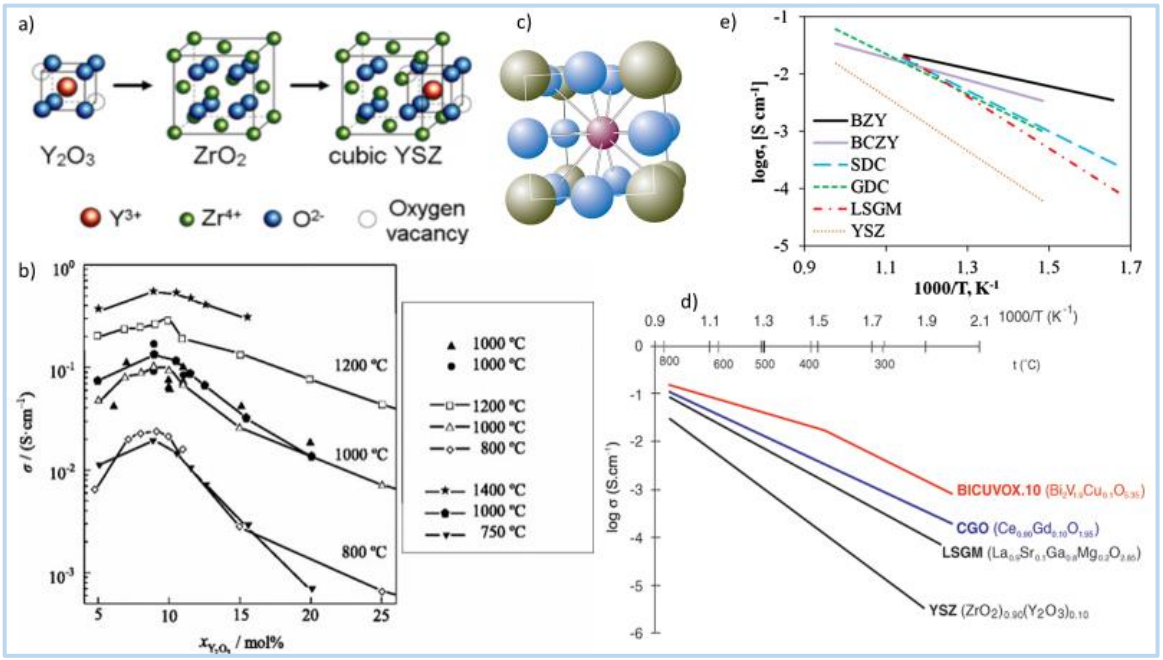

Figure 3: **a)** Schematic illustration of Yttria stabilized zirconia with 12% or more Yttria [32]; **b)** Conductivity of Yttria stabilized zirconia as a function of temperature and content of Y_2O_3 (mol%) [31]; **c)** Schematic illustration of perovskite structure (ABO_3); A-cations, B-cations, oxygen ions are the red, green and blue spheres respectively [27]; **d)** Ion conductivities of main oxygen ion conductors [27] and **e)** Ionic conductivities of proton conductors: $BaZr_{0.8}Y_{0.2}O_{3-\delta}$ (BZY), $BaCe_{0.7}Zr_{0.1}Y_{0.2}O_{3-\delta}$ (BCZY) and oxygen ion conductors: $Ce_{0.8}Gd_{0.2}O_{2-\delta}$ (GDC), $Ce_{0.8}Sm_{0.2}O_{2-\delta}$ (SDC), 8%mol Yttria stabilized zirconia (8YSZ) and $La_{0.8}Sr_{0.2}Ga_{0.8}Mg_{0.2}O_{3-\delta}$ (LSGM) against temperature [53].

Even though the YSZ is the dominant zirconia-based material employed as electrolyte, other alternatives have also attracted scientific research. Scandia oxide (Sc_2O_3) within zirconia oxide (ZrO_2) has gained essential prominence as a solid electrolyte that could diminish the operating temperatures of SOFCs. Generally, YSZ is effectively used in SOFCs at operating temperatures exceeding 850°C. However, at lower temperatures, YSZ shows mechanical and chemical instability, and thus, it isn't appropriate for application in intermediate temperature (IT)-SOFCs. On the contrary, Scandia stabilized zirconia (ScSZ) presents greater ionic conductivity

than YSZ at working temperatures lower than 850°C. Thus, ScSZ is a promising electrolyte and is thoroughly investigated for further improvement of factors such as ionic conductivity, thermal stability, and mechanical properties [34].

As it is mentioned above, ceria forms the fluorite structure like zirconia. Doped ceria materials, with the general formula $Ce_{1-x}M_xO_{2-\delta}$ (M: alkaline-earth or rare-earth ions), have been thoroughly studied due to their promising properties. In particular, doped ceria presents higher ionic conductivity, mainly at intermediate temperatures, compared with zirconia-based materials, and thus, they can find application as solid electrolytes in IT-SOFCs. Besides, doped ceria has a plethora of applications ranging from electrochemical sensors and catalytic membranes to composite electrodes. As it happens in stabilized zirconia, the oxygen vacancies are also the path for the ions in doped ceria. These vacancies are generated by introducing heterovalent cations such as Gd^{3+}, Sm^{3+}, Nd^{3+} and La^{3+}. Among them, gadolinium doped ceria (CGO) and samarium doped ceria (CSO) have been reported as materials showing adequate ionic conductivity. For instance, $Ce_{0.9}Gd_{0.1}O_{1.95}$ presents ionic conductivity of about 0.01 S/cm at 500°C. Concerning its application in SOFCs, doped ceria is chemically stable in the cathode but not in the reduced fuel environment of the anode. Subsequently, electronic conduction appears in the anode due to the reduction of Ce^{4+} to Ce^{3+} [35, 36, 37].

Perovskite structures

Besides the fluorite structure of zirconia and ceria-based materials, other notable structures can also conduct oxygen ions, such as the perovskites (ABO_3). In **Figure 3c**, a perovskite structure is demonstrated, where, generally, (A) is a large cation such as a rare earth metal and (B) is a smaller cation. Among the perovskite oxides, only the materials based on lanthanum gallate ($LaGaO_3$) have been proved as an adequate choice for ionic applications in electrochemical devices. Specifically, doping with strontium (Sr) and magnesium (Mg) at the A-site and B-site respectively develops materials with high ionic conductivity. These materials, with the general stoichiometry $La_{1-x}Sr_xGa_{1-y}Mg_yO_{3-\delta}$ (LSGM), were first reported in the pioneering investigations of Ishihara and his team [38, 39, 40]. The application of LSGM as an electrolyte at intermediate temperatures (650°C-800°C) has gained interest due to its promising performance. The ionic conductivity of LSGM is comparable with that of fluorite structured oxides, and it can be even more improved by the further substitution of Co in the B-site. Additionally, there is decent chemical compatibility between the LSGM-based electrolyte and the mixed conducting material of the cathode during SOFC operation. On the

other hand, the volatility of Ga in reducing environments is a considerable problem that is appeared at high temperatures [27, 41].

Other structures

The evident need for lowering the operating temperatures in electrochemical devices has given a tremendous impulse to the scientific research of new ion-conducting materials. Thus, alternative materials conducting oxygen ions have been developed, except for materials with conventional structures. Apatite-structured oxides are included in the recent developments of oxygen ion conductors. Among the several compositions, lanthanum silicates ($La_{1-x}Si_6O_{26+y}$) and lanthanum germanates ($La_{1-x}Ge_6O_{26+y}$) have been substantially studied due to their high ionic conductivities. In addition, these materials provide a wide range of possible dopants which can further enhance the material properties [42]. LAMOX and BIMEVOX families of oxide ion conductors are also numbered among the new developments. The materials derived from the compound $Bi_4V_2O_{11}$, also known as BIMEVOXs, occur by doping the vanadium site (V) with aliovalent and/or isovalent metal cations (ME), such as Li^+, Cu^{2+}, Fe^{3+}, Ge^{4+}, and Nb^{5+}. The ionic conductivity of this class of materials is considerably higher than the conventional electrolytes, approximately 0.1 S/cm at 600°C. Thus, BIMEVOXs have been considered adequate materials in applications such as low temperature (LT)-SOFCS, oxygen separation membranes**,** and water electrolysers. However, during their application in fuel cells, they present intrinsic instability in the reducing environment [43]. The LAMOX family is based on $La_2Mo_2O_{11}$ and developed at the beginning of this century [44, 45]. Although its promising ionic conductivity, many steps are required, regarding scientific research, for its possible commercial use. The ionic conductivities of some of the abovementioned oxygen ion conductors are presented in **Figure 3d** [27].

3.5.2 Proton (H^+) conductors

Since the transition from fossil fuels to green energy sources constitutes a worldwide goal, there is immense interest in electrochemical devices such as solid oxide fuel cells. The cost of these devices is a critical factor for their commercial use. From this standpoint, the development of new electrolyte materials is an essential requirement for eliminating the operating temperatures and thus, for the decrease of the cost as well. Solid oxide proton conducting materials play a dominant role in this effort because of their distinguished properties, including high proton conductivity and stability. The materials of this class can be classified according to their operating temperature, their transport properties, or their

structure. Concerning the temperature, they can be low temperature (T_w<150), intermediate temperature (150<T_w<350), or high temperature (T_w>400) proton-conducting materials. From them, high-temperature proton conductors (HTPC) have gained prominence as the most promising for application in electrochemical devices. Their utilization ranges from electrolytes in SOFCs, sensors, and electrolysis cells to hydrogen-permeable membranes for hydrogen production. In HTPCs, proton transport occurs through the interaction between oxide compounds and gas components containing hydrogen at elevated temperatures. Additionally, the measurement conditions determine the transport properties in HTPCs. In particular, these materials can be pure protonic conductors, co-ionic (oxygen ionic/protonic) conductors, or mixed conductors combining proton/electron or proton/electron/oxygen-ion conductivity [18, 29].

$BaCeO_3$-based materials

The ever-increasing scientific research during the last decades has revealed proton-conducting materials with different structures such as fluorites, perovskites, brownmillerite, apatite, mayenite, and others. However, only the perovskite structure has shown suitable properties in terms of the concentration and mobility of proton defects. Examples of such a structure are materials based on barium cerate ($BaCeO_3$) and barium zirconate ($BaZrO_3$). $BaCeO_3$-based materials have been on the edge of proton-conducting materials since the 1980s because they demonstrate the highest protonic conductivity. As it is mentioned in 3.4.2, the proton conductivity in these systems results from the interaction between oxygen vacancies and water vapor. In the case of $BaCeO_3$, the oxygen vacancies are generated by doping the basic structure with, usually, trivalent acceptor elements. In particular, barium cerate-based materials are expressed by the general formula $BaCe_{1-x}Ln_xO_{3-\delta}$, where x is the dopant concentration. It is noteworthy that the conductivity maximizes as the dopant concentration reaches values at x=0.1-0.25. Additionally, it was found that the dopants showing the highest conductivity are samarium, yttrium, and gadolinium (Ln= Sm, Gd, Y) [29, 47, 48].

However, not only the conductivity of these materials must be considered the main parameter, but the chemical and thermal stability are also crucial factors for application in electrochemical devices. Several studies have reported the low thermodynamic stability of $BaCeO_3$-based materials during their interaction with H_2O and other acidic compounds. This behavior exhorts researchers to develop materials that exhibit high proton conductivity and, simultaneously,

adequate stability against the environments of the operating conditions. Thus, several strategies have been investigated to create stable materials with satisfactory transport properties. In one of the common methods, known as co-doping, the perovskite structure of $BaCeO_3$ is doped by two cations that support different roles. High ionic conductivity is achieved by one dopant (acceptor element) while stability is enhanced by the other one (donor dopant). Among the several combinations of dopants, zirconium has been reported as the most effective co-dopant at $BaCe_{1-x}Ln_xO_{3-\delta}$ (Ln=Gd, Y). Nevertheless, all these methods result in an inevitable decrease, to some extent, in ionic conductivity. Currently, researchers aim to overcome the problems in terms of the preparation methods of these materials (high synthesis temperature) and the transport, chemical, and thermal properties [47-52]. **Figure 3e** compares some of the most promising oxygen-ion and proton conductors, plotting their ionic conductivities against temperature [53].

$BaZrO_3$-based materials

Materials based on barium zirconate ($BaZrO_3$), along with the barium cerate, are included in the most intricately investigated proton-conducting electrolytes. Barium zirconate demonstrates better chemical stability than barium cerate due to the properties of its crystal structure. Moreover, $BaZrO_3$-electrolytes doped by yttrium, $BaZr_{1-x}Y_xO_{3-\delta}$ (BZY), show high thermodynamic stability at 300°C-600°C. On the other hand, their total proton conductivity is significantly low compared with the barium cerate systems. Another drawback that must be considered is that they require high sintering temperatures [29].

3.5.3 Ag^+ conductors

Silver ion conductors are a class of materials with the remarkable feature of exhibiting high ionic conductivity even at ambient temperatures. In 1914, silver ion-conducting solids were first reported by Tubandt and Lorenz with their studies on silver halides. According to their observations, silver iodide in the a-phase (a-AgI) exhibits ionic conductivities commensurate with those of liquid electrolytes at temperatures higher than 147°C. However, most silver ion conductors show high ionic conductivity, mainly at high temperatures. Thus, the researchers try to enhance the Ag^+ conduction by stabilizing the a-AgI at lower temperatures or creating new conducting phases. An example of the latter strategy is the a-$RbAg_4I_5$ which is among the materials showing the highest ionic conductivity at room temperatures [54].

3.5.4 Na^+ conductors

Sodium-ion conducting solid electrolytes have commanded the attention of many researchers, as they are an attractive choice for electrolytes in solid-state batteries. The most popular Na^+ conductors are the family of β-aluminas, which were widely studied in the 1970s and 1980s. This family of materials consists of two basic crystal structures. The first is β-Al_2O_3 with chemical stoichiometry $Na_2O_{8-11}Al_2O_3$, and the second is β″-Al_2O_3 with chemical stoichiometry $Na_2O_{5-7}Al_2O_3$. Among the two crystal structures, β″-Al_2O_3 shows the highest ionic conductivity reaching values in the range of 0.22-0.35 S/cm at 300°C (polycrystalline β″-Al_2O_3). However, at room temperatures, the ionic conductivity of β″-Al_2O_3 is about 0.002 S/cm. Another sodium ion conductor is the NASICON family of materials with the general formula $Na_{1+x}Zr_2P_{3-x}Si_xO_{12}$ ($0 \leq x \leq 3$). The ionic conductivity for those materials is approximately 10^{-1} S/cm at 300°C and in the order of 10^{-4} at room temperatures. Although beta alumina and NASICON present high ion conductivity and stability, they still have limited efficiency at room temperatures. Consequently, researchers are seeking materials with high performance at ambient temperatures [54, 55].

3.5.5 Li^+ conductors

Since lithium-ion batteries have monopolized the global market, Li^+ ion conductors have attracted scientific and industrial interest. Those batteries use liquid electrolytes, which show adequate ionic conductivity but are flammable. Thus, one of the matters of great importance is to replace the liquid electrolyte with a solid electrolyte to create a solid-state battery without fire risks. Fast ion conduction in Li^+ solid-state materials interests the global scientific community in several discoveries of those materials. However, the ionic conductivities of the existing solid electrolytes cannot reach those of liquid electrolytes. Consequently, many steps are required for the commercialization of solid-state batteries, which combine high ionic conductivity at room temperatures with safety and long cycling life [56].

Chapter 4

Electrochemical devices for energy production and storage

Abstract

In chapter 4, a brief description of electrochemical devices for energy conversion and storage, namely fuel cells, batteries and capacitors, is conducted. These devices are analyzed concerning their principle of operation and the different types. Also, some of the challenges that interest the researchers are discussed.

4.1 Fuel cells

4.1.1 Introduction

Fossil fuels, which mainly cover the energy demands, are a restricted resource and, simultaneously, have an intense environmental impact. Additionally, their unstable prices and the fact that a limited number of countries possess the majority of fossil fuel reserves are problems that can lead to economic and geopolitical crises. Fuel cells are gathering colossal interest due to the unprecedented need for secured and sustainable energy. More precisely, they are electrochemical devices that convert chemical energy into electricity through redox reactions.

Contrary to conventional combustion engines, fuel cells produce electricity without first converting the chemical energy of the fuel into thermal energy. Conventionally, fuel cells are fueled with hydrogen or other H-rich fuels, such as methanol, ethanol, and natural gas. Except for the fuel, they also need an oxidant such as oxygen from ambient air. Fuel cells cover a broad spectrum of applications, including power generation, electronic devices, backup power, military equipment, and transportation [57, 58, 59].

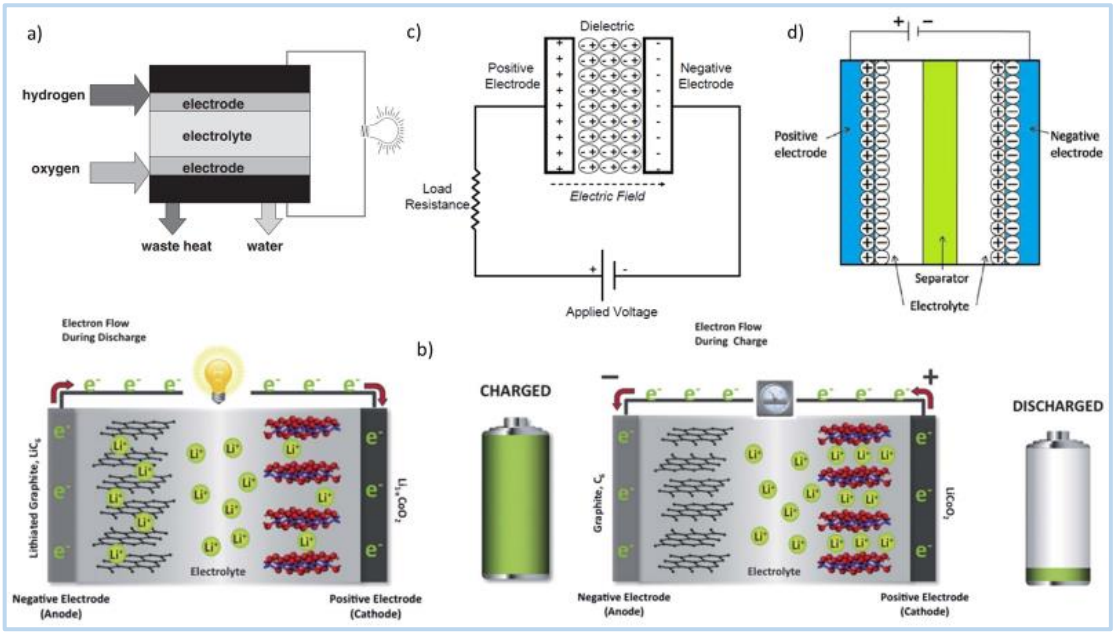

Figure 4: **a)** Schematic illustration of a fuel cell [58]; **b)** Presentation of a typical lithium-ion battery during charge and discharge [83]; **c)** Schematic presentation of a conventional capacitor [95] and **d)** Scheme of charge-discharge mechanism in supercapacitor [96].

Fuel cells have substantial advantages in comparison with conventional energy conversion systems. Firstly, they can achieve over 50% efficiency, while the efficiencies of internal combustion engines average around 20%. From an environmental viewpoint, fuel cells can be featured as a sustainable way of producing electricity, as they attain low or zero emissions of greenhouse gases. In case of pure hydrogen used as fuel, the by-products are water and heat, with the latter being negligible compared with conventional combustion. In addition, they are simpler than combustion engines in terms of structure (no moving parts) and the principle of operation. Thus, they have the potential for widespread commercialization producing energy at a cost commensurate with conventional systems [57, 58, 59, 60].

4.1.2 Principle of operation

As it is shown in **Figure 4a**, a fuel cell is composed of two electrically conductive electrodes and an electrolyte that is sandwiched between them. The fuel, typically hydrogen, is fed to the anode and it is oxidized producing electrons and ions. Additionally, the oxidant, typical oxygen supplied from the air, is fed to the cathode. The electrons move through an external circuit producing useful work and the ions move across the electrolyte. At the cathode, the ions meet the electrons, activating the oxygen reduction reaction and producing water and heat. There are several types of fuel cells distinguished by the used electrolyte, the operating temperature, the type of fuel, the reaction at the electrodes, and the efficiency of the cell

(**Table 1**). For instance, the reactions taking place in the simplest fuel cell (PEM) are given by the following equations.

Anode reaction: $H_2 \rightarrow 2H^+ + 2e^-$ (4.1)

Cathode reaction: $^1/_2\, O_2 + 2H^+ + 2e^- \rightarrow H_2O$ (4.2)

Overall reaction: $H_2 + {}^1/_2\, O_2 \rightarrow H_2O + heat$ (4.3)

4.1.3 Types of fuel cells

Proton exchange membrane fuel cell (PEMFC)

This type of fuel cell consists of a proton-conducting electrolyte squeezed between two electrodes. The principle of operation of PEM fuel cells is described in the previous subchapter with the corresponding electrochemical reactions (4.1-4.3). In addition, a layer with catalyst particles conventionally made up of platinum is used to speed up the electrochemical reactions. The management of waste products, namely heat and water, is crucial for the cell's efficiency. PEM fuel cells operate in the temperature range of 70-90°C producing a wide power range (1W-500kW) [57, 58, 59, 61]. For this reason, they can be used in a plethora of applications such as power storage and transportation [62, 63, 64, 65, 66, 67, 68].

Direct alcohol fuel cell (DAFC)

In PEMFCs, the hydrogen supplied in the anode must be free of impurities. Among the hotly debated issues concerning the commercialization of fuel cells are hydrogen storage and distribution. This situation has given a huge impetus to the development of Direct Alcohol Fuel cells (DAFCs) parallel to PEMFCs. In particular, except for hydrogen, alcohols such as ethanol and methanol can also be fed to the anode in devices known as Direct Ethanol/Methanol Fuel Cells (DEFC/DMFC). Compared with hydrogen, methanol and ethanol have higher power densities and are more convenient because they are liquid fuels. DAFCs operate at temperatures up to 100°C and are suitable for applications with power output below 250W. Among the main problems that must be addressed are the costly materials used as catalysts, i.e., Pt and Ru, as well as the degradation of performance due to the fuel crossover moving from the anode to the cathode [61, 69, 70, 71, 72, 74, 75]. The electrochemical reactions that take place in DEFCs are given by the following equations [59, 73].

Anode: $C_2H_5OH + 3H_2O \rightarrow 2CO_2 + 12H^+ + 12e^-$ (4.4)

Cathode: $3O_2 + 12H^+ + 12e^- \rightarrow 6H_2O$ (4.5)

Total reaction: $C_2H_5OH + 3O_2 \rightarrow 2CO_2 + 3H_2O$ (4.6)

Alkaline fuel cell (AFC)

Another type of fuel cell is the alkaline fuel cell also known as anion exchange membrane fuel cell (AEMFC). Alkaline fuel cells have considerably low operation temperatures, specifically 23-70°C, and contrary to PEMFCs, they conduct OH^- anions from the cathode to the anode through an alkaline electrolyte such as KOH or NaOH. The electrochemical reactions happening in the anode and cathode of an AFC are [59],

Anode: $H_2 + 2OH^- \rightarrow 2H_2O + 2e^-$ (4.7)

Cathode: $H_2O + {}^1/_2\, O_2 + 2e^- \rightarrow 2OH^-$ (4.8)

Phosphoric acid fuel cell (PAFC)

The principle of operation of phosphoric acid fuel cells as well as the electrochemical reactions at the electrodes are common with PEMCs. However, PEMFs use phosphoric acid (H_3PO_4) as an electrolyte and operate at a higher temperature range (150°C-220°C). Among the different types of fuel cells, PAFCs are the most commercially used. In addition, their high operation temperatures enable their application in combined heat and power systems (CHP) producing increased efficiency. On the other side of the coin, they also use Pt catalyst which increases the cost [59].

Molten Carbonate fuel cell (MCFC)

Molten carbonate fuel cells are considered devices operating at intermediate temperatures, namely 550-700°C. Conventionally, the electrolyte in these devices consists of lithium and potassium carbonate and conducts CO_3^{2-} ions from the cathode to the anode. MCFCs are flexible as regards the fuel type, using hydrogen carriers such as natural gas. Furthermore, they have opened a new window for carbon capture and storage because they use CO_2 as an oxidant. The higher operating temperatures have remarkable advantages, such as no requirement for noble materials and the potential for exploitation of waste heat. However, these temperatures entail corrosion and limitations in materials. The following equations (4.9-4.10) express the electrochemical reactions of MCFCs [59].

Anode: $CO_3^{2-} + H_2 \rightarrow H_2O + 2e^- + CO_2$ (4.9)

Cathode: $CO_2 + 2e^- + {}^1/_2\, O_2 \rightarrow CO_3^{2-}$ (4.10)

Solid oxide fuel cell

Solid oxide fuel cells (SOFC) are rapidly gaining ground because they have a plethora of advantages such as high efficiency, flexibility in fuels, and cost-effectiveness. To begin with, they are composed of a solid electrolyte, typically made up of YSZ, which allows their operation at the highest temperatures among fuel cells (600-1100℃). The anode and cathode sides consist of nickel-based YSZ and Lanthanum Strontium Manganite (LSM) respectively, with the former accelerating the hydrogen oxidation reaction [59]. The distinguishing characteristic of SOFCs is their versatility in fuel choice. More precisely, several options such as hydrogen, methanol, ethanol, methane, gasoline and ammonia can be used in SOFCs, offering a sustainable source of power generation. For instance, in the case of methane, steam reforming transforms the methane into a mixture of CO_2 and H_2 which is subsequently supplied to the anode. Since this is an endothermic process, the required heat can be exploited by the SOFC electrochemical section (internal reforming) or by partial fuel combustion (external reforming) [76, 77, 78, 79, 80, 81]. The electrochemical reactions of SOFCs and steam reforming process can be simplified as follows,

Methane steam-reforming: $$CH_4 + H_2O \rightarrow CO + 3H_2 \quad (4.11)$$

Gas shift reaction: $$CO + H_2O \rightarrow CO_2 + H_2 \quad (4.12)$$

Anode: $$H_2 + O^{2-} \rightarrow H_2O + 2e^- \quad (4.13)$$

Cathode: $$^1/_2\, O_2 + 2e^- \rightarrow O^{2-} \quad (4.14)$$

Table 1: Types of fuel cells [59].

Types of fuel cells	Operating temperatures	Fuel	Membrane/ Electrolyte	Cell's electrical efficiency	Power range	Applications
PEMFC	70-90℃	H_2	Nafion	50-70%	1W-500KW	Transportation, backup power, portable power
DAFC	<100℃	CH_3OH C_2H_5OH	Nafion	20-30%	100mW-1kW	Electronic devices
AFC	23-70℃	H_2	Alkaline	60-70%	10W-200kW	Spacecraft, Military, Backup power
PAFC	150-220℃		Phosphoric acid	55%	50kW-1MW	Distributed generation
MCFC	550-700℃	H_2/CO/CH	Molten carbonate	55%	<1kW-1MW	Auxiliary power, Distributed generation
SOFC	600-1100℃		YSZ	60-65%	5kW-3MW	

4.2 Batteries

4.2.1 Introduction

Batteries are defined as electrochemical devices able to store energy. The science and technology of batteries have been developed by leaps and bounds since their invention by Alessandro Volta more than 200 years ago. Nowadays, batteries are considered by the scientific and industrial sectors as a key element for the removal of fossil fuels from the global energy mix. Conventionally, a battery includes stacks of electrochemical cells arranged in series or parallel. Each cell constitutes two electrical conducting electrodes separated by an electronically insulating and ion-conductive electrolyte. The electricity is produced by the movement of electrons between the electrodes via the external circuit. At the same time, the movement of ions across the electrolyte ensures electroneutrality in the cell. These electrons and ions are generated by the electrochemical reactions taking place at the electrodes. The redox reactions determine the current flow in the sense that if one of the reactions stops, the movement of electrons stops. In a secondary battery, also called rechargeable, an applied external current can reverse the process resulting in the recharge of the battery. In contrast, this process isn't feasible in the primary batteries, which are also known as non-rechargeable batteries [82].

4.2.2 Lithium-ion batteries

Among several types of batteries, lithium-ion batteries have drawn vast attention dominating the global battery market. Due to their remarkable properties, these batteries have a plurality of applications ranging from portable devices to transportation. In 1991, Sony paved the way by presenting the first lithium-ion battery. Typically, the anode of a lithium-ion battery is composed of a graphite host structure accommodating lithium (LiC_6). The cathode constitutes a metal lithium oxide such as $LiCoO_2$, at which different combinations of components, conventionally Ni and Mg, are often substituted to enhance the cell's performance. In most cases, the electrolyte is a liquid solution made up of a lithium salt that is dissolved in different solvents. Additionally, the electrodes are separated by an electrically insulated membrane in order to prevent short circuits. During the use of the battery (discharge), the electrons flow from the anode to the cathode through the external circuit producing the electric current. Simultaneously, the lithium ions travel across the electrolyte to the cathode. Conversely, during the charge, the ions and electrons are detached due to the externally connected power source moving to the anode through the electrolyte and the external circuit, respectively. In **Figure 4b**,

the basic cell structure of a lithium-ion battery is demonstrated. In addition, the reactions taking place in the system are,

Cathode: $$LiCoO_2 \rightarrow Li_{1-x}CoO_2 + xLi^+ + xe^- \quad (4.15)$$

Anode: $$xLi^+ + xe^- + xC_6 \rightarrow xLiC_6 \quad (4.16)$$

Overall reaction: $$LiCoO_2 + xC_6 \rightarrow Li_{1-x}CoO_2 + xLiC_6 \quad (4.17)$$

When the battery is charged the reactions at the electrodes follow the direction of the previous equations. Conversely, the reactions follow the opposite direction during the discharge [83, 84, 85, 86, 87, 88, 89, 90].

4.2.3 Solid state batteries

The liquid electrolyte that is commercially used in lithium-ion batteries accumulates serious disadvantages. Firstly, the organic solvent included in the liquid electrolyte is toxic to the human body in the case of leakage, creating concerns about the safety of lithium-ion batteries. Moreover, the flammability and the low boiling point of the electrolyte are responsible for serious problems such as thermal runaway and limited operating temperatures. It is crystal clear that a liquid electrolyte cannot offer high energy density in conjunction with flexibility in operating temperatures. On the contrary, batteries based on solid electrolytes are a promising technology that can solve the safety and performance limitations of conventional lithium-ion batteries. More precisely, they have the potential for higher energy density, longer life expectancy and safer operation. For these reasons, the industrial and scientific sectors have oriented their efforts to the optimization of solid-state batteries, accelerating their large-scale commercialization [91, 92, 93].

4.3 Capacitors-supercapacitors

4.3.1 Conventional capacitors

Except for batteries, the capacitors are also devices that store energy and contain two electrically conductive plates, also known as electrodes, separated by a dielectric layer. Typically, glass, ceramic, plastic, and aluminum oxide are used in the dielectric layer because they are electrical insulators. As an external power source is connected to the electrodes, the voltage pushes the electrons, accumulating them on one electrode. Thus, negative, and positive charges are built up at the electrodes, charging in this way the capacitor. During discharge, the electrons are released to the connective load and the capacitor distributes its stored energy. Consequently, the capacitor returns to the neutral phase, where it has an equal number of electrons in the electrodes [94]. The amount of stored energy in a capacitor is quantified by the capacitance (C) given by equation (2.40),

$$C = \varepsilon_O \varepsilon_r \frac{A}{D} \tag{4.18}$$

As it is observed by the previous equation, capacitance (C) is proportional to the plates' surface area (A) and inversely proportional to the thickness of the dielectric layer (D). ε_r and ε_o are dielectric constants of insulating material and free space, respectively. A capacitor is featured by its energy and power density. The energy density (E) is expressed as,

$$E = \frac{1}{2} C V^2 \tag{4.19}$$

Where V is the essential applied potential difference to charge the capacitor. Additionally, the maximum power of a capacitor is expressed by the equation (4.20), where the R is referred as the equivalent series resistance of the circuit in **Figure 4c** [95].

$$P_{max} = \frac{V^2}{4 \cdot R} \tag{4.20}$$

4.3.2 Supercapacitors

Generally, conventional capacitors have low energy density and high power density in comparison to batteries and fuel cells. For these reasons, a capacitor can store less energy than a battery, but it can quickly release high power. The limitations of conventional capacitors have oriented scientific research toward new materials enhancing the performance [95]. Thus, a new type of capacitor, known as electrochemical capacitor or supercapacitor, has been developed. Contrary to conventional capacitors, supercapacitors contain two porous electrodes with increased surface area and less distance between them, resulting in higher capacitance. Moreover, instead of the dielectric layer, there is an electrolyte (liquid or solid) and a very thin separator. The interfaces between the electrolyte and the electrode are called electric double layer. Due to the high surface area of these interfaces, supercapacitors can store greater amounts of energy than dielectric capacitors**.** As **Figure 4d** shows, an applied voltage induces the electrodes with opposite polarity, resulting in the formation of the electric double layer at the interfaces [95].

Generally, supercapacitors are used in cases requiring promptly increased amounts of energy. At present, the electrolytes used in supercapacitors are aqueous, ionic liquid, or organic liquids, offering high ionic conductivity and adequate performance. However, they limit the operating temperatures and present a high risk for leakage. Thus, replacing liquid electrolytes with solid electrolytes seems to be a promising solution. A Solid electrolyte cannot only operate as an ionic conducting medium in the device but also as a separator. Additionally, it offers an extended range of operation, no leakage risk, and freedom in design [94, 97].

Chapter 5

Experimental techniques for materials and sensors characterization

Abstract

In the present chapter, the fundamental principles of experimental techniques used by the researchers for the characterization of materials are demonstrated. Initially, the techniques for electrochemical characterization are provided. These techniques are performed with the aid of a three-electrode system. The basic electrochemical techniques presented in this chapter are voltammetry techniques (CV, LSV, SWV, CA), EIS and RDE. In the second part of the chapter, some of the conventional physicochemical techniques are analyzed, such as SEM, TEM, XPS and RS. These techniques provide an extensive analysis of materials' surfaces.

5.1 Electrochemical techniques

Electrochemical techniques are a key component of an electrochemical study because they contribute to a deeper comprehension of the electrochemical behavior of materials. The performance of materials applied in electrochemical devices, namely sensors and energy storage devices, can be assessed through electrochemical techniques. Additionally, these techniques provide information about the mechanisms involved in electrochemical devices such as ion and electron transport. Thus, a growing number of researchers incorporate electrochemical characterization into their studies in order to enhance the reliability of their research [98-106].

5.1.1 The three-electrode system

The electrochemical techniques are based on measurements of potential or current used to characterize the reactivity of an analyte or ascertain its concentration. The measured values are electrochemical signals operating as analytical signals, and thus, they are considered the fundamental experimental designs for every electrochemical characterization technique. As mentioned in section 2.1.2 Electrochemical cell, an electrochemical cell generates current and voltage utilizing chemical reactions or activates chemical reactions through an applied electrochemical signal. An electrochemical cell can be formed by different kinds of electrode

systems, such as the two-electrode and three-electrode systems, through which electrochemical characterization can be carried out. The two-electrode system comprises the working electrode and the counter electrode. The working electrode's surface is the place where the electrochemical reactions happen due to its contact with the analyte solution. The potential applied at the working electrode generates electrons flowing through the externally connected circuit and arrive at the counter electrode completing the circuit. The working electrode's potential, which is sensitive to the concentration of the analyte solution, is measured in comparison with that of the counter electrode. However, the counter electrode must maintain a stable potential as reference potential and simultaneously complete the circuit. This is difficult to be achieved and thus, the three-electrode system is mostly used for electrochemical characterization [100, 107].

In **Figure 5a**, a three-electrode cell is schematically illustrated, consisting of the working or sensing electrode, the counter or auxiliary electrode, the reference electrode, and the liquid electrolyte. In this system, the voltage is measured between the working electrode and the reference electrode, with the current flowing through the working and counter electrodes. Concerning the reference electrode, it must provide stable and certain potential in order to monitor any change in the working electrode's potential. Additionally, it is placed close to the working electrode, minimizing the effect of cell resistance. Typically, the three-electrode system uses the hydrogen electrode (SHE), the silver/silver chloride electrode, or the calomel electrode as a reference electrode. In terms of the auxiliary electrode, inert conducting materials (platinum or graphite) are used, with larger surface areas than the other electrodes. Voltammetry methods are a typical example of electrochemical techniques where the three-electrode system is used. In these methods, a time-dependent potential is applied to a three-electrode system in order to study the current response with respect to the applied potential. The observed results are plotted in a voltammogram through which the electrochemical characterization is accomplished [100, 107].

5.1.2 Cyclic voltammetry (CV)

Cyclic voltammetry is a foremost, simple, and fast electrochemical test used in electrochemical investigations. This versatile method provides quantitative and qualitative features of electrochemical processes. For instance, the mechanisms and kinetics of redox reactions can be understood through the CV. During the cyclic voltammetry experiment, a linear potential sweep is applied to the sensing electrode at a constant scan rate, ranging from

few mVs^{-1} to several hundred Vs^{-1}. This means that the potential passes from an initial value of potential V_1 to a final value V_2, and subsequently is applied in the reverse direction returning to the initial value. Thus, the voltage measured between the working electrode and reference electrode and the resulting current measured between the working and counter electrodes are plotted in a diagram known as the cyclic voltammogram [100, 107, 108].

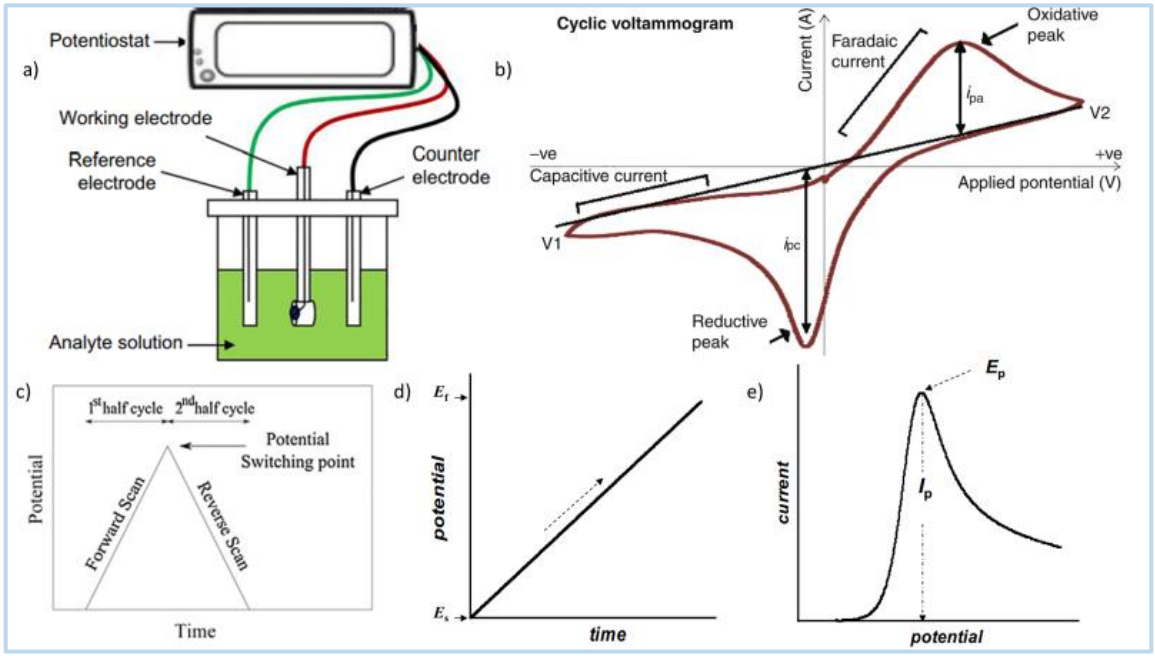

Figure 5: a) Schematic representation of a three-electrode cell [107]; **b)** Potential-time function of a cyclic voltammetry experiment [100]; **c)** Schematic illustration of a typical cyclic voltammogram [108]; **d)** Schematic representation of the potential-time function of the linear sweep voltammetry [111] and **e)** Illustration of a voltammogram obtained at the linear sweep voltammetry [111].

Figure 5b shows the input potential signal of the cyclic voltammetry experiment as a function of time and in **Figure 5c**, a conventional cyclic voltammogram is presented. The major characteristic of the latter diagram is that it presents an oxidation and a reduction peak. As the potential increases from the initial value V_1 to value V_2, the current also increases until the potential reaches a certain value called anodic (oxidative) peak potential E_{pa}. Further increase of potential leads to the decrease of current, reaching the final value of potential.

During the reverse cycle, the potential passes from V_2 to V_1, and the current increases in the negative direction until a certain value of potential called cathodic (reductive) peak potential E_{pc}. The analysis of the cyclic voltammogram provides important information about the properties of materials (capacitive nature) as well as the system behavior (reversibility). Except for the anodic and cathodic potentials, anodic and cathodic peak currents are also essential parameters in CV. These currents can be calculated by the Randles-Sevcik equation,

$$i_p = 2.69 \times 10^5 n^{3/2} AC\sqrt{\nu D} \quad (5.1)$$

Where i_p (A) is the peak current, n expresses the number of transferred electrons in the redox reactions, A is the sensing electrode's area (cm^2) is the scan rate (V/s), D represents the diffusion coefficient (cm^2/s), and C is the bulk concentration of the reactants (mol cm^{-3}) [100, 107, 108, 109].

5.1.3 Linear sweep voltammetry (LSV)

Linear sweep voltammetry is a voltammetry method akin to cyclic voltammetry. A linearly with time voltage is applied at the sensing electrode on both methods. However, in LSV, the applied voltage starts from a primary value of voltage E_i and ends up in a final value of voltage E_f without following the reverse direction. The voltage E_i corresponds to a situation where no electrochemical reaction happens at the electrode, while the voltage E_f corresponds to a situation where a redox reaction takes place. Just as in CV, so too in LSV, the current increases with voltage reaching a peak. When the voltage surpasses this peak, the reactant has difficulty reaching the electrode's surface due to the presence of the product's diffusion layer, resulting in the decrease of current. The general potential-time function for linear sweep voltammetry is given in **Figure 5d**, and a linear sweep voltammogram is presented in **Figure 5e** [109, 110].

5.1.4 Square-wave voltammetry (SWV)

Square-wave voltammetry is a technique that enhances the sensitivity and the quality of the measurements. The continuous potential ramp of the abovementioned techniques is replaced by a staircase potential function, along with small potential pulses. During SWV, the voltage is advanced in the shape of a square wave which increases in time linearly **Figure 6a (left)**. At each potential step, the forward and reverse pulses drive the reaction in anodic and cathodic directions, respectively. The current is measured at the end of each pulse, with the difference between them, denoting the net current. A typical voltammogram of SWV illustrates the net current (I_{net}) against the potential step (E_{step}), as is shown in **Figure 6a (right)**. SWV is an advanced method that can predict the adsorbed electroactive molecules on the electrode's surface [100, 111].

5.1.5 Chronoamperometry (CA)

Among voltammetric methods, chronoamperometry has been extensively used due to its simplicity and reliability. The basic concept of this method is based on the application of a single voltage step and the measurement of the current resulting from this potential. In its most uncomplicated form, chronoamperometry contains the working and counter electrodes

along with the electrolyte solution that includes just the analyte's oxidized form, O, at a concentration of C_o. Initially, a potential is applied between the electrodes in such a way that no redox reactions occur at the surface of the working electrode and no net current exists. After that, at time t_o, a new potential is applied such that the main percentage of O at the surface of the working electrode is immediately reduced to R. Additionally, any O reaching the electrode by means of diffusion is also reduced, resulting in negligible concentration of O at the electrode's surface. After a time, t_s, the applied voltage returns at a value that allows the oxidation of R to O, and the experiment is accomplished. In **Figure 6b (left)**, a typical potential-time plot of chronoamperometry is schematically presented.

The charge transferred (Q) during the reaction is estimated by Faraday's law as follows,

$$Q = n \cdot F \cdot N \cdot A \tag{5.2}$$

Where F is the Faraday's constant, A is the electrode's area, n is the number of electrons involved in the reaction, and N expresses the moles of O reduced to R. An equation for the faradic current can be extracted by differentiating the equation (5.2) and using the Fick's law.

$$i_f = -nFAD \left(\frac{\partial(x,t)}{\partial x}\right)\Big|_{x=0} \tag{5.3}$$

This equation can be modified in the Cottrell equation and is plotted in the **Figure 6b (right)**. Cottrell equation relates the current response of a redox reaction with the time as follows,

$$i_f(t) = \frac{nFAC_0\sqrt{D}}{\sqrt{\pi t}} \tag{5.4}$$

Where C_o is the concentration of the reactant and D is the diffusion constant. Equation (5.4) shows that when the potential is applied at time t_o, the current response (i_f) is infinite. After that time, it immediately drops and approaches zero [110].

5.1.6 Electrochemical impedance spectroscopy (EIS)

The ability of a circuit to resist the flow of electrons is described by the electric resistance and measured by Ohm's law (R=E/I). Even though it is a famous equation, it is only applicable to the ideal resistor. In practice, resistors differ from the ideal behavior described by Ohm's law as the ideal resistor entails many simplifying properties. Initially, it obeys Ohm's law at all applied voltage and current values. The resistance of a perfect resistor is frequency independent with the AC current and potential across this resistor being in phase. However, the actual circuit elements cannot be described by these simplifying properties, so impedance is used in systems with complex behavior. Impedance expresses the ability of a system to resist the movement of

electrons without the limitations of the abovementioned simplifying properties. The measurement of impedance is carried out by applying an AC voltage to an electrochemical system and recording the resulting current. These measurements are produced over an extended range of frequencies, forming an experimental technique called impedance spectroscopy [112].

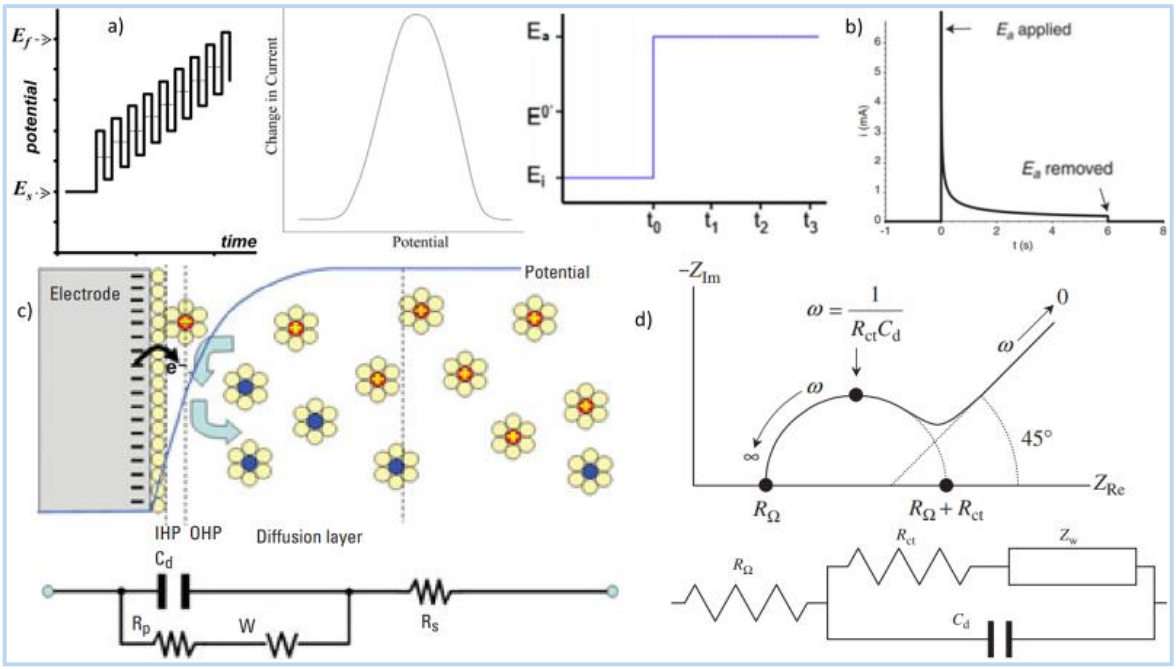

Figure 6: a) Typical input potential in square-wave voltammetry (left) [100] and the current response in square-wave voltammetry (right) [111]; **b)** Typical potential-time plot of chronoamperometry [19], ii) The ideal current response to potential step of E_a in chronoamperometry [110]; **c)** Schematic illustration of an electrified interface together with the equivalent circuit [114] and **d)** A conventional Nyquist plot in conjunction with the equivalent circuit [115].

In a typical electrochemical cell, the electrochemical process between the electrode and the electrolyte involves different characteristics such as the concentration of electroactive species, mass transfer between the bulk solution and the electrode, and charge transfer. In EIS, these features can be represented by an equivalent electrical circuit that comprises resistances, capacitors, or pinions. For instance, an electrified electrode-electrolyte interface and the equivalent electric circuit are given in **Figure 6c**. The positively charged ions (oxidants) reach the electrode's surface through diffusion, gain electrons at the surface (reductants), and diffuse to the bulk solution. The circuit that represents each component in the solution and at the surface is composed of a double layer capacitor (C_d) connected in parallel with a Warburg impedance (W or Z_w) and a polarization resistor (R_p or R_{ct}), connected in series with the solution resistance (R_s or R_Ω). The complexity of the equivalent circuit depends on the electrochemical reactions taking place at the surface. During these reactions, Faradaic and non-Faradaic components arise. The faradaic current describes the

mass transport and the rate of electron transfer, while the non-Faradaic current occurs due to the formation of the electric double layer. In the described circuit, the electron transfer is expressed by the polarization resistance (R_p) and the mass transport by the Warburg impedance (W) [113, 114].

In EIS, a small amplitude periodic perturbation (AC) is applied in the electrochemical cell, providing a measurement of impedance response. By acquiring the impedance data over a wide range of frequencies, information about the features of the electrochemical processes can be obtained. Nyquist plot and Bode plot are conventional ways of presenting the impedance data. In electrochemical investigations, Nyquist plots are a useful tool that can be easily connected with electric models. As expressed by equation (3.5), the impedance is a complex number that contains the real part (Z_{RE}) and the imaginary part (Z_{IM}) [114, 115].

$$Z_{cell} = Z_{Re} + i \cdot Z_{Im} \tag{5.5}$$

Accordingly, the Nyquist plot occurs by plotting the real part on X-axis and the imaginary part on the Y-axis. It must be mentioned that the imaginary part of the Y-axis is negative ($-Z_{IM}$). In the Nyquist plot, each point is the impedance at a certain frequency, with the right side of the plot containing low frequencies and the left side of the plot higher frequencies. A conventional Nyquist plot is presented in **Figure 6d** along with the equivalent circuit. From this plot, information about the polarization resistance, the solution resistance, and the double layer capacitance can be extracted. For instance, the intercept on the X-axis at the region of high frequencies shows the solution resistance (R_Ω) and the diameter of the plotted circle shows the polarization resistance (R_{ct}). Additionally, the double-layer capacitance (C_d) is extracted by the frequency at the top of the plotted circle [113, 115].

EIS is a broadly used technique as it can provide in situ information about the electrochemical mechanisms occurring at the surface of the electrode and the electrolyte. These mechanisms are involved in practical applications such as batteries, fuel cells, and the corrosion of alloys and metals. EIS also enables the understanding of adsorption on the electrode's surface and the kinetics of homogenous or heterogeneous electrochemical reactions. Concerning gas sensors, EIS has been reported as a tool that assesses the sensing ability of gas sensors and predicts the sensing mechanisms taking place [116, 117].

5.1.7 Rotating disk electrode (RDE)

In electrochemical systems, the chemical reactions that take place in the anode and the cathode involve electron transfer across the interface between the electrode and the electrolyte. This process requires a continuous supply of reactant at the electrode's surface and continuous removal of product. Accordingly, mass transport is a contributing factor to the effectiveness of electrochemical processes, and it can be characterized by three forms in electrochemistry. The first is diffusion in which the movement of a species is caused by a concentration gradient. The second is the convention which can occur because of an external mechanical energy such as electrode rotation. Lastly, the migration due to a voltage gradient is also a form of mass transport that only affects the charged species [118].

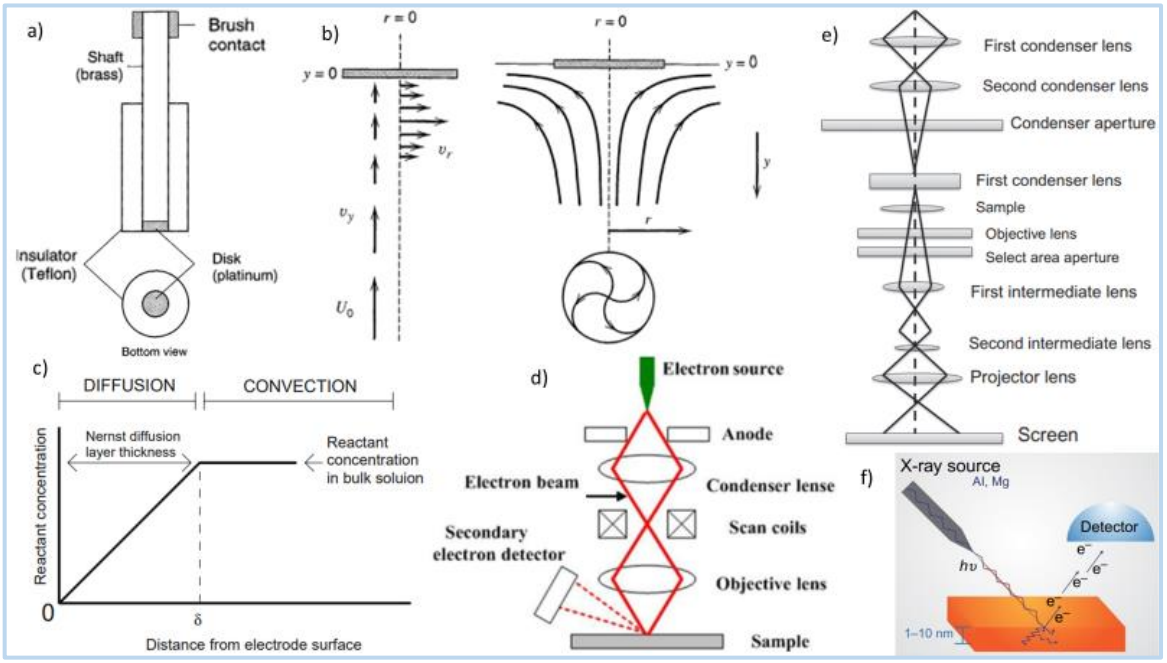

Figure 7: a) Illustration of the basic RDE set up [119]; **b)** The profiles of velocity (left) and mass transfer (right) in RDE [119]; **c)** Nernst's diffusion layer model [118]; **d)** Illustration of the major components in SEM [128]; **e)** A typical configuration of TEM [131] and **f)** Schematic illustration of principles of XRS [132].

In laboratory experiments, the researchers try to attain experimental conditions in which the mass transfer is well defined in order to develop accurate measurements. Rotating disk electrode (RDE) is a typical hydrodynamic method used to create a well-defined solution flow pattern, where the convention is almost the sole mechanism of mass transport. The arrangement of the RDE comprises a disc electrode set into an insulating surround. This structure is rotated about its perpendicular axis in a range between 400 and 10000 rpm, resulting in a steady-state laminar flow. **Figure 7a** illustrates a classical RDE setup. RDE provides precise control of diffusion and

convection of reactant to the electrode, so it can be used to investigate the kinetics at the surface of the electrode. Additionally, it is an effective way to calculate parameters of mass transport, such as the diffusion coefficient. **Figure 7b** shows the profiles of velocity and mass transfer in the RDE. The forced convection of RDE causes the limitation of the diffusion layer, which increases the limiting current density [115, 118, 119].

Nernst diffusion layer model assumes that the electrolyte can be split into two regions, as it is shown in **Figure 7c**. The first zone includes the region close to the electrode's surface, where it is supposed that there is a stagnant layer, and thereby, only diffusion occurs. In RDE, the solution close to the electrode's surface can be assumed as stationary because it has the same angular velocity as the electrode. In the second region, convection dominates, with the concentrations of the reactants remaining constant. The thickness of the diffusion layer δ_o is calculated by the following equation,

$$\delta_O = 1.61 \cdot D_O^{1/3} \cdot \omega^{-1/2} \cdot \nu^{1/6} \quad (5.6)$$

Where D_O expresses the diffusion coefficient, ω is the rotation velocity and v is the viscosity of the solution [115, 118, 119].

The Levich's experiment uses a RDE in conjunction with linear sweep voltammetry at a low scan rate (1-10 mVs^{-1}) and over a range of rotation velocities. Initially, the applied potential at RDE doesn't cause electrochemical reactions. As the applied potential increases and the steady-state conditions are attained, the reactant's concentration at the surface of the electrode decreases due to the existence of the electrochemical reaction. When the concentration of the reactant close to electrode is zero, the progress of the reaction depends on the reactant's diffusion through the diffusion layer. The current response under these conditions is the limiting current and is given by Levich's equation,

$$i_L = 0.62 \cdot n \cdot F \cdot A \cdot D^{2/3} \cdot \omega^{1/2} \cdot \nu^{-1/6} \cdot C \quad (5.7)$$

Where n is the electrons involved in the reaction, F is the Faraday's constant, A is the electrode area and C is the reactant's concentration. The results of the Levich's experiment are demonstrated in a plot of the limiting current against the square root of rotation speed [115, 118, 119].

5.2 Physicochemical techniques

Physicochemical techniques aiming at defining materials' physical and chemical properties, such as composition, quality and stability. Physicochemical characterization focuses on the

surface of materials. Thus, important information about the chemistry of materials can be extracted [120, 121, 122, 123, 124, 125, 126, 127].

5.2.1 Scanning electron microscopy (SEM)

Scanning electron microscopy is a commonly used technique for the depiction of the morphology and the microstructure of the materials. In this method, a focused electron beam is emitted to the sample and scans its surface. As the beam hits and enters the sample, several photos and electrons are produced. These produced signals are detected by the detectors above the sample, resulting in the formation of an image. In **Figure 7d**, the basic arrangement of SEM is illustrated. Initially, the electron gun generates the electron beam, which is accelerated and diverged by means of the anode. Subsequently, the electron beam is focused on the specimen by the condenser and objective lenses. The impact of the electron beam generates different types of signals such as backscattered electrons, secondary electrons, and auger electrons. In most cases of SEM, only secondary and backscattered electrons are detected by solid-state BSE detectors and ET (Everhart-Thornley) detectors, respectively. Note that a high vacuum system is a key element of SEM because it protects from the contamination of the components and the scattering on the electron beam. SEM is a method that can produce images with a resolution of 1nm [128, 129].

5.2.2 Transmission electron microscopy (TEM)

Transmission electron microscopy (TEM) is a widely used physicochemical technique that reveals the microstructure of materials. This technique offers direct images with high resolution, surpassing the level of atomic dimensions (<1nm). The arrangement of TEM is similar to that of SEM, containing components such as the electron gun and the electromagnetic lenses. The difference between the two methods lies in the position of the sample and in the way that the signals are gathered by the sample. In the basic form of TEM, the produced by the electron gun electron beam is transmitted through an extremely thin sample (<50nm). During this interaction between the electron beam and the sample's material, the incident electrons are converted into scattered or unscattered electrons. These electrons are focused on a screen via a series of electromagnetic lenses generating the image. Compared with SEM, TEM offers higher spatial resolution, and it can be combined with other analytical methods for better chemical analysis. On the other side of the coin, the ultra-thin sample and the high vacuum environment are important limitations of TEM that must be mentioned. Additionally, the high-voltage electron beams can cause extensive damage to the sample.

Lastly, SEM produces 3D images, while TEM is a technique providing 2D images of the sample. The basic configuration of TEM is presented in **Figure 7e** [130, 131].

5.2.3 Raman spectroscopy (RS)

Raman spectroscopy (RS) is a frequently used physicochemical technique characterizing the chemical structure of materials. C.V. Raman laid the foundation for this technique after his discovery that during the passage of light through a transparent material, there is a portion of reflected light undergoing changes in its wavelength. More precisely, a monochromatic light can be absorbed, reflected, or scattered, as it hits the sample. A small part of the scattered light is inelastic and possesses a different frequency in comparison with that of incident light. In RS, the measurement of the difference between the frequencies of inelastic scattered and incident photos is suitably connected with the chemical structure of the material. Consequently, several investigations use RS to make accurate measurements of a material's surface [130, 131]

5.2.4 X-ray photoelectron spectroscopy (XPS)

X-ray photoelectron spectroscopy (XPS) is a well-known and convenient method employed to characterize the material's surface. In particular, it can reveal the atomic composition of the specimen, providing information for all the elements found on the surface except H and He. This technique, also called X-ray photoemission spectroscopy, exploits the photoelectron effect of materials. The photoelectron effect was noticed by Heinrich Hertz in 1987 and was thoroughly described by Albert Einstein in 1905. The material emits electrons when interacts with electromagnetic radiation, such as light. In XPS, the surface of the sample is bombarded by X-rays, which penetrate the material to a depth of about 1-10 nm. Then, the detectors examine the atomic composition of the surface by measuring the kinetic energy of the emitted electrons. Thus, there are a plethora of materials that can be investigated by XPS, as it is a surface-sensitive and non-destructive technique. However, its high sensitivity and the requirement of vacuum conditions make the XPS an expensive technique. The basic features of X-ray photoelectron spectroscopy are presented in **Figure 7f** [132, 133, 134].

Chapter 6

Electrochemical gas sensors

Abstract

The present chapter introduces the theoretical background of electrochemical gas sensors. Their history and principles of operation are briefly discussed. Additionally, some of the most well-known types of electrochemical gas sensors, such as potentiometric and amperometric sensors, are presented.

6.1 Introduction

Electrochemical devices pique the interest of both scientific and industrial sectors, as they offer sustainable energy production and storage. Apart from fuel cells, batteries, and supercapacitors, electrochemical gas sensors also play a vital role in humanity's endeavor to find cleaner energy sources. Generally, electrochemical gas sensors (EGSs) have powerfully entered several fields, calculating the concentration of different gases, substances concerning food safety analysis, as well as agriculture and health sectors. These sensors deserve notice in comparison with other sensing technologies because they combine in situ measurements with simple design, low cost, accuracy, and adequate selectivity. The analysis of gas composition occurs through redox reactions. Consequently, the response of these reactions can provide information about the concentration of the gaseous species [135, 136, 137, 138, 139].

6.2 Brief history

The need for gas detection has been created since the 19th century. In this period, while the industrial revolution was in progress, coal miners had been trying to detect harmful gases. In particular, they used a torch across the mine, with the ignition of the torch being a signal of combustible gases, such as methane. Additionally, coal miners used canaries as a form of gas alarm system. The health of the canaries operated as a criterion for the safety of the atmosphere in the mine. Later in 1815, Humphry Davy invented the first artificial gas sensor

called Davy's lamp. This device was frequently used by coal miners for the detection of methane and oxygen. However, these methods are not safe and reliable because they cannot predict the type and the concentration of detected gas, resulting in many accidents [140].

Despite the fundamental advances in electrochemistry during the 19th century, the first electrochemical gas sensor was invented one century later, in the 1950s, for oxygen detection. After twenty years, the oxygen sensor, also called lambda sensor, was developed for emission control in gasoline-based vehicles. In the following decades until the 1980s, the intense research in gas sensing technologies broadened the range of toxic gases that can be detected, resulting in their commercial use. Currently, with the unprecedented need for gas sensing, electrochemical gas sensors have penetrated almost every field, from automotive and industries to medical applications [141].

6.3 Principle of operation

Conventionally, an electrochemical gas sensor (EGS) comprises at least two electrodes, a working and a counter electrode, immersed in an electrolyte. This electrode-electrolyte configuration is placed inside the sensor housing together with a hydrophobic membrane, which is only permeable by the target gas. In many cases, a third electrode, called the reference electrode, can be added. The capillary diffusion barrier allows only the passage of the target gas into the sensor, preventing the penetration of liquid or dust molecules. The gas of interest diffuses through the hydrophobic membrane, which also operates as a deterrent against electrolyte leakage, and reaches the working electrode. In this electrode, also known as the sensing electrode, an electrochemical reaction is carried out, namely oxidation or reduction reaction. The former forces the electrons to move from the working to the counter electrode, while the reduction reaction moves them conversely. The produced electric signal can show the amount of target gas that gets oxidized or reduced, providing direct information about the gas concentration [142, 143].

According to their principle of operation, EGSs can be divided into two general categories. In the first category are contained the active sensors, in which the potential difference between the electrodes acts as the sensing signal. Equilibrium potentiometric sensors, as well as mixed potential sensors, are active sensors. The second category includes the passive sensors, which require an externally applied voltage at the sensing electrode to drive an electrochemical reaction. The produced current of this reaction is the measured signal (amperometric sensors). The continuous redox reactions taking place at the electrode can disturb the sensing

signal, limiting, in this way, the sensor's performance. For this reason, a reference electrode is placed close to the sensing electrode, maintaining a constant potential [141, 142, 143].

6.4 Types of electrochemical sensors

Electrochemical gas sensors are divided into different types depending on their principle of operation and configuration. These types are potentiometric (equilibrium and non-equilibrium), amperometric, combined amperometric-potentiometric, resistive and impedance-based gas sensors [2].

6.4.1 Equilibrium potentiometric gas sensors

A typical potentiometric gas sensor configuration comprises an electrolyte, in the shape of a tube closed at one end, whose sides are covered by two electrodes. Particularly, the reference electrode (RE) and the sensing electrode (SE) are placed on the internal and external sides of the electrolyte, respectively. Potentiometric gas sensors assign the sensing signal, namely the potential difference between these two electrodes, to the concentration of the target gas. Both electrodes contain a catalyst coating, conventionally made up of platinum, to increase the redox reactions speed, resulting in enhanced sensor performance [142, 143, 144].

Potentiometric gas sensors operate by measuring the potential difference between the electrodes when there is no electrical current flow through the sensor. This voltage corresponds to open-circuit voltage (OCV) or formerly referred as electromotive force (EMF). The electrode/electrolyte configuration of potentiometric sensors represents a concentration cell whose sides have different chemical potentials of ionic species. Nernst Equation is used to calculate the open-circuit voltage and it is given by the equation 6.1.

$$E = -t_i \frac{RT}{zF} \ln \frac{p'_{gas}}{p''_{gas}} \tag{6.1}$$

where t_i is the ion transference number, R the universal gas constant, z the number of electrons that are involved in redox reactions at electrodes, T the absolute temperature, F Faraday's constant, and p_{gas} the partial pressure of the gas on the inside atmosphere (p'_{gas}) and the outside atmosphere (p''_{gas}) of the sensor. Consequently, the composition of the target gas is determined by knowing the open-circuit voltage and the characteristics corresponding to the gas of the reference atmosphere [141, 144].

Among the potentiometric sensors, oxygen sensors with ceramic ion-conducting electrolytes are maybe the most widely used. A common example of these sensors is the lambda sensor

employed for controlling the combustion process in automotive applications. They follow the abovementioned principle to measure the oxygen concentration in exhaust gases. During their operation, the oxygen gas oxidizes at RE and reduces at SE, resulting in an equilibrium potential given by Equation 6.4.

Reduction: $$O_2 + 4e^- \rightarrow 2O^{2-} \quad (6.2)$$

Oxidation: $$2O^{2-} \rightarrow O_2 + 4e^- \quad (6.3)$$

$$E = -\frac{RT}{4F} \ln \frac{p'_{O_2}}{p''_{O_2}} \quad (6.4)$$

Where t_O=1 because of the oxygen ion conductor electrolyte, z=4 and $p_{o_2}$is oxygen partial pressure for inside and outside atmospheres. A typical lambda sensor is displayed in **Figure 8a** [144, 145, 146].

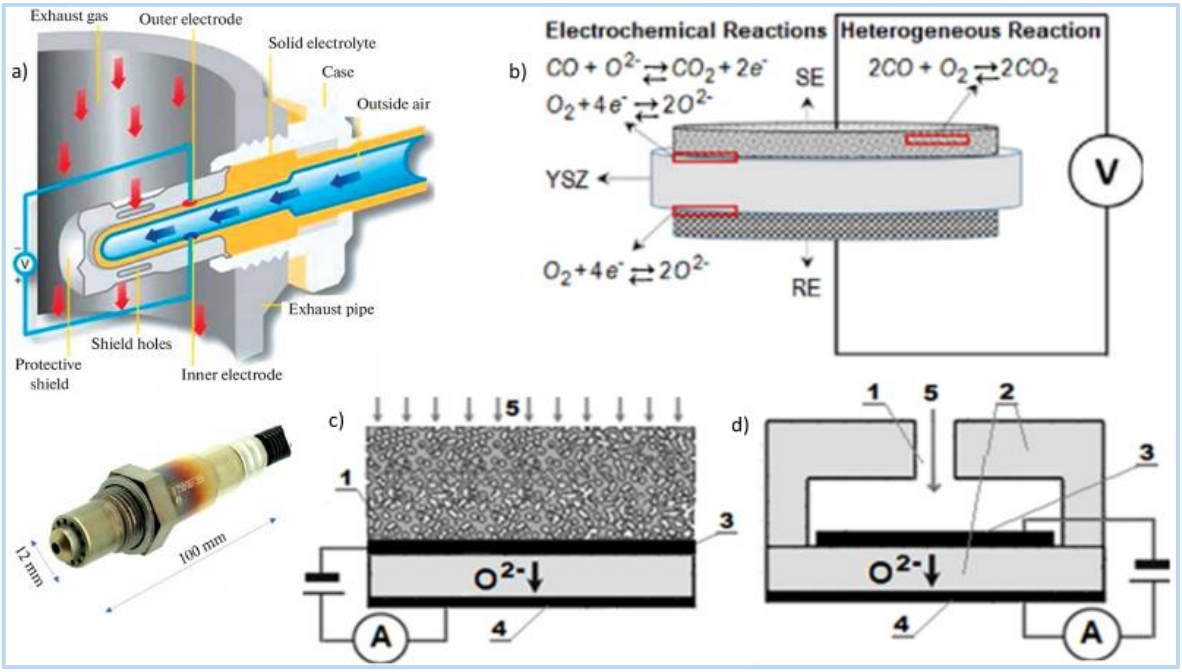

Figure 8: **a)** Schematic illustration of lambda sensor [145]; **b)** a typical configuration of a mixed potential sensor [149]; **c)** schematically illustration of an amperometric sensor equipped with a porous medium: 1) diffusion barrier (porous medium), 2) solid electrolyte, 3) electrode of cathode, 4) electrode of the anode, and 5) tested gas [153] and **d)** a typical configuration of an amperometric sensor equipped with a capillary barrier: 1) diffusion barrier (capillary barrier), 2) solid electrolyte, 3) electrode of cathode, 4) electrode of the anode, and 5) tested gas [151].

6.4.2 Mixed potential sensors

This type of electrochemical sensor is similar to the abovementioned equilibrium potential sensor in terms of its configuration and principle of operation. As the gas mixture, including oxygen, is supplied to an equilibrium potentiometric sensor, a steady potential resulting from

the oxygen redox reactions at the electrode/electrolyte interface is established. Nevertheless, the sensing mechanism of mixed potential sensors involves more than one reaction leading to the establishment of a mixed potential. This behavior, known as non-Nernstian, was not comprehensible until 1980 when Okamoto et al. presented the notion of mixed potential sensors [147]. This type of gas sensor is appropriate for detecting non-equilibrium gas mixtures, including H_2, CO, CO_2, HC, nitric oxides (NO_X), NH_3, SO_2, and H_2S. In **Figure 8b**, a mixed potential sensor for carbon monoxide detection is schematically illustrated. CO-sensor is a representative example of a mixed potential sensor providing an overview of its configuration and operation principle. Particularly, it is used an YSZ electrolyte surrounded by a platinum reference electrode and a sensing electrode designed according to the target gas. During its operation, the supplied gas mixture reaches the SE and activates two redox reactions, or rather the cathodic reaction (6.5) and the anodic reaction (6.6).

$$O_2 + 4e^- \rightarrow O^{2-} \tag{6.5}$$

$$CO + O^{2-} \rightarrow CO_2 + 2e^- \tag{6.6}$$

Note that the former generates oxygen ions consumed in the latter reaction. Thus, a mixed potential emerges when these reactions reach a state where the reactions' currents are equal (steady-state). In parallel, the equilibrium potential of reaction 6.5 is established at the RE/YSZ interface. Note that the RE can be exposed to the reference atmosphere, conventionally air, or exposed directly to the sample gas if it is inactive to the gas of interest. The resulting electrode potential is only contingent on the oxygen concentration. Consequently, the measured potential difference between the SE and RE constitutes the sensor signal. As the kinetics of the reactions (6.5) and (6.6) taking place on SE affects the sensor response, the material choice for SE constitutes a critical factor for the sensor performance [144, 148, 149, 150].

6.4.3 Amperometric sensors

Amperometric sensors follow a different principle compared to potentiometric sensors. Being passive sensors, they work under an externally applied voltage, through which specific electrochemical reactions are activated at electrodes. As it is demonstrated in **Figure 8c** and **Figure 8d**, a typical amperometric sensor configuration contains a diffusion barrier that regulates the target gas flow reaching the electrode. This barrier can be a porous medium or a capillary that leads into the inner chamber of the sensor. When an amperometric sensor is exposed to the tested atmosphere, the gas of interest reaches the electrode's surface by means

of the porous medium or the capillary filling the sensor's cavity. The gas molecules reaching the electrode react due to the applied voltage and diffuse through the electrolyte in the external space of the sensor. For instance, the corresponding electrochemical reaction in an amperometric oxygen sensor is the reaction (6.5). Consequently, there is a dynamic balance between the flow of analyzed gas pumped out from the internal space and the flow of analyzed gas that diffuses through the diffusion barrier [151]. Faraday's law determines this process correlating the generated electrical current and the diffusion flow of gas of interest,

$$J(gas) = \frac{I}{nF} \tag{6.7}$$

where I, n, and F are the observed current, the number of electrons participating in the reaction, and the Faraday's constant, respectively. As the applied voltage rises, the flow of target gas pumped out, represented by the reaction rate, rises too. This increase continues until a specific value of voltage, where the amount of analyzed gas concentrated inside the sensor is insignificant. Thus, a further increase in voltage does not induce changes in the observed current. This current is known as the limiting current (I_{lim}) and relates to the mole fraction of gas of interest (X_{gas}) as follows [152],

$$I_{lim} = -\frac{zFD_{gas}PA}{RTL}\ln(1 - X_{gas}) \tag{6.8}$$

where z and F have been defined in equation (6.7), D_{gas} is the diffusion coefficient, P the absolute pressure, T is the temperature, R is the ideal gas constant, and L, A are the length and area of the diffusion barrier, respectively. Based on the operating conditions, the diffusion coefficient can be calculated according to the Chapman-Enskog theory:

$$D_{gas} = D_O(\frac{T}{T_O})^m \frac{P_O}{P} \tag{6.9}$$

here, P_O, T_O, D_O represent the absolute pressure, absolute temperature, and diffusion coefficient, respectively, at standard conditions (1 atm and 25°C), while P and T are the corresponding variables at operating conditions and m is constant taking values between 1.5 and 1.9 [144].

Contrary to potentiometric sensors, amperometric sensors don't require a reference atmosphere for their operation. In some cases, such as the hydrogen potentiometric sensors, a reference atmosphere cannot be effective as their operating environments include temperatures above 600°C. Under this condition, there is difficulty in establishing a stable reference potential. As presented by equation (6.8), the limiting current in an amperometric

sensor is linearly proportional to the gas concentration. For this reason, amperometric sensors have a considerable advantage over potentiometric sensors concerning their accuracy in intermediate as well as high gas concentrations. However, the sensitivity of potentiometric sensors at such concentrations is considerably decreased in comparison to amperometric sensors because of the logarithmic relation between the sensing signal and gas concentration. By combining a plethora of materials with different geometries, amperometric sensors can detect a multitude of gases, including H_2, O_2, CO, CH_s, NO_x, and NH_3 [2, 144].

6.4.4 Combined amperometric-potentiometric gas sensors

This type of gas sensor is more advanced than pure amperometric and potentiometric sensors, combining their configuration and principles. Combined sensors are composed of two electrochemical cells, namely, an amperometric and a potentiometric one. The former operates by pumping the target gas inside or outside the sensor and measuring the limiting current. The latter measures the EMF in order to evaluate the operation of the first cell (amperometric) or to indicate the concentration of the analyzed gas. Despite the complicated principle of operation, compared with the abovementioned types, this type of sensor has the potential to increase the reliability of the sensor due to its ability to measure the limiting current and EMF at the same time [144, 154].

6.4.5 Impedimetric gas sensors

Impedimetric sensors have accumulated vast interest due to their alternative principle for detecting the target gas. Based on impedance spectroscopy, an experimental technique thoroughly described in 5.1.6 Electrochemical impedance spectroscopy (EIS)these sensors apply a sinusoidal voltage and measure the resulting current. Thus, with the previous parameters known, the impedance is calculated in the frequency domain. Their design is akin to non-equilibrium potentiometric sensors but in the latter, the voltage is measured instead of applied. Sensors based on solid electrolyte or semiconductor-based sensors can use impedance-based techniques for gas detection. For instance, impedimetric sensors using YSZ have been reported for the detection of water vapor, NO_x, and CO [2, 144].

Chapter 7

Electrochemical gas sensors based on solid electrolytes

Abstract

The present chapter constitutes an analytical description of electrochemical gas sensors using solid oxide electrolytes. The below discussed sensors are analyzed depending on their structural materials, mainly the electrolytes, the configuration, and the principles of operation. Combustible gas sensors detecting hydrocarbons, carbon monoxide, and carbon dioxide are demonstrated. The reported sensors operate at high temperatures ranging from 300°C to 1000°C.

7.1 Detection of Combustible Gasses

7.1.1 Detection of CO and C_nH_{2n+2} Hydrocarbons (HCs)

Nowadays, more and more governments strive to eliminate air pollution by applying austere policies. Toxic and flammable gases originating from industrial and domestic sources have detrimental effects on human health and the environment. At present, the monitoring of emissions in internal combustion engines is mostly accomplished using solid-state oxygen sensors. For instance, the previously mentioned oxygen sensor based on YSZ is a widespread technology frequently used in gasoline-powered vehicles since 1990. However, the ever-increasing environmental pressures for restricting gas emissions require electrochemical sensors able to detect more pollutants such as CO and HCs. Among the different pollutants, carbon monoxide gas is responsible for severe air poisoning in several countries. CO is emitted from incomplete combustion of HCs such as natural gas and gasoline in cars. Concentrations of CO at approximately 10 ppm are enough to cause headache, while at higher concentrations, such as 600 ppm, carbon monoxide can lead to severe physical symptoms and even to death. The control of CO is feasible only by using appropriate gas sensors because it is tasteless, odorless, and colorless. From a different viewpoint, in-situ data about the efficiency of the combustion process can be extracted by monitoring the

concentration levels of CO. These data can upgrade the combustion process because the firing process can be controlled and adjusted, resulting in higher efficiencies and decreased emissions. Ideally, a solid-state sensor of should be able to operate in extremely aggressive environments at temperatures up to 1000℃, detecting the gas of interest at low concentrations, namely at a few ppm [144, 155, 156].

Mixed Potential Combustible Gas sensors

The detection of CO and hydrocarbons is mainly carried out by the mixed potential gas sensors, where the sensor response is the potential difference between the RE and SE. Concerning the applied solid electrolytes in these sensors, YSZ has the lion's share, with a few reports also suggesting β-alumina [157] or $Ce_{0.8}Ga_{0.2}O_{1.9}$ (CGO) [150]. The selection of electrolytes in mixed potential sensors is mostly based on their ability to facilitate the kinetics of the electrochemical reactions at the three-phase boundary. As depicted in **Figure 8b,** the small region between the YSZ electrolyte/electrode (SE or RE) interface and the analyzed gas is the three-phase boundary. As mixed potential sensors work under non-equilibrium conditions, their optimum working temperatures range between 500 and 600 ℃. By increasing temperature, the mixed potential response decreases because the system approaches equilibrium. The research has principally shifted towards the development of electrode materials for these sensors. Conventionally, electrodes in mixed potential sensors contain noble metals such as Pt and Au [159]. There are also reports for electrodes made up of single metal oxides, with the most popular being WO_3 for CO detection [160] and Nb_2O_5 [161, 162] for HC/CO detection, at 450-700℃. Recently, Nickel oxide (NiO) was used as a sensing electrode for CO detection in an YSZ-based MPS, demonstrating decent sensitivity at 1000℃ [156]. Alternative materials that have been proposed as sensing materials are doped oxides and perovskites such as $LaMnO_3$, $LaCoO_3$, and $LaFeO_3$ [163, 164, 165]. However, except for the need for a reference atmosphere, mixed potential sensors show poor selectivity due to their principles of operation. Additionally, they present high cross-sensitivity because of the reactions of HCs and CO with oxygen [144]. Note that, the cross-sensitivity is caused when interfering gases react in the sensor, disturbing its response.

Amperometric combustible sensors

The analysis of combustible gases can be also accomplished by YSZ-based amperometric sensors. These sensors sidestep major requirements of potentiometric sensors, such as the establishment of a reference atmosphere and an equilibrium potential. However,

amperometric sensors using oxygen-ion conductors as solid electrolytes are barely reported in the literature for combustible gas analysis. In 2015, G. Fadeyev et al. [166] presented an amperometric sensor able to detect H_2, CO, and CH_4 in N_2-atmosphere at 450°C. Note that, the detection of combustible gases in their mixtures with N_2 possesses practical significance as most thermal catalytic analyzers require oxygen atmospheres for their effective operation. As demonstrated in **Figure 9a**, the configuration of the previously mentioned amperometric sensor contains two cells employing 9YSZ (0.91 ZrO_2+ 0.09 Y_2O_3) as a solid electrolyte. These cells are designed as square plates (11x11x1 mm) with 0.5 mm deep grooves and are hermetically sealed by glass sealant. The chamber formed between the cells is connected to outer space by a diffusion barrier. As previously mentioned, the use of capillary as a diffusion barrier in preference to the porous medium provides some considerable advantages, such as the potential for decent reproducibility. This sensor uses a metallic capillary with a thin inner diameter (0.1mm) as a diffusion barrier. The Pt electrodes are placed on the internal and external surfaces of one of the cells along with the current wire leads [144, 166].

This sensor operates under the principles of amperometric sensors that have been described in 6.4.3 Amperometric sensorsMore precisely, steam reacts at the external electrode of the sensor due to the positive potential applied at the internal electrode. Steam exists in the analyzed gas mixture in the form of residual humidity, approximately 10 ppm, and its decomposition is expressed by the following reaction:

$$H_2O + 2e^- \rightarrow H_2 + O^{2-} \quad (7.1)$$

The generated oxygen anions (O^{2-}) are conducted to the sensor's chamber through the YSZ electrolyte. Reaching the inner electrode, they react with the target gas, in this case, H_2, CH_4 and CO, as follows:

$$H_2 + O^{2-} \rightarrow H_2O + 2e^- \quad (7.2)$$

$$CO + O^{2-} \rightarrow CO_2 + 2e^- \quad (7.3)$$

$$CH_4 + 4O^{2-} \rightarrow CO_2 + 2H_2O + 8e^- \quad (7.4)$$

During the realization of the abovementioned reactions, the concentration of target gas (H_2, CH_4, and CO) inside the sensor's chamber is reduced. The current response increases with the applied voltage, reaching a maximal achievable limit corresponding to the limiting current. At this point, the concentration of combustible gases approaches zero. Limiting current indicates the target gas concentration and is given by the following equation:

$$I_{lim,k} = \frac{PAF}{RTL} D_k X_k z_k \quad (7.5)$$

where, except for the values described in 6.4.3 Amperometric sensorsk expresses the corresponding gas of interest (k= H_2, CH_4, or CO), D_k is the diffusion coefficient, X_k is the mole fraction of detected gas, and z_k is the number of involved electrons in the reactions (z_k=2 for H_2, CO, and z_k=8 for CH_4). This equation can also be modified for the calculation of the diffusion coefficient D_k:

$$D_k = \frac{R \cdot T \cdot L \cdot I_{lim,k}}{P \cdot A \cdot F \cdot X_k \cdot z_k} \quad (7.6)$$

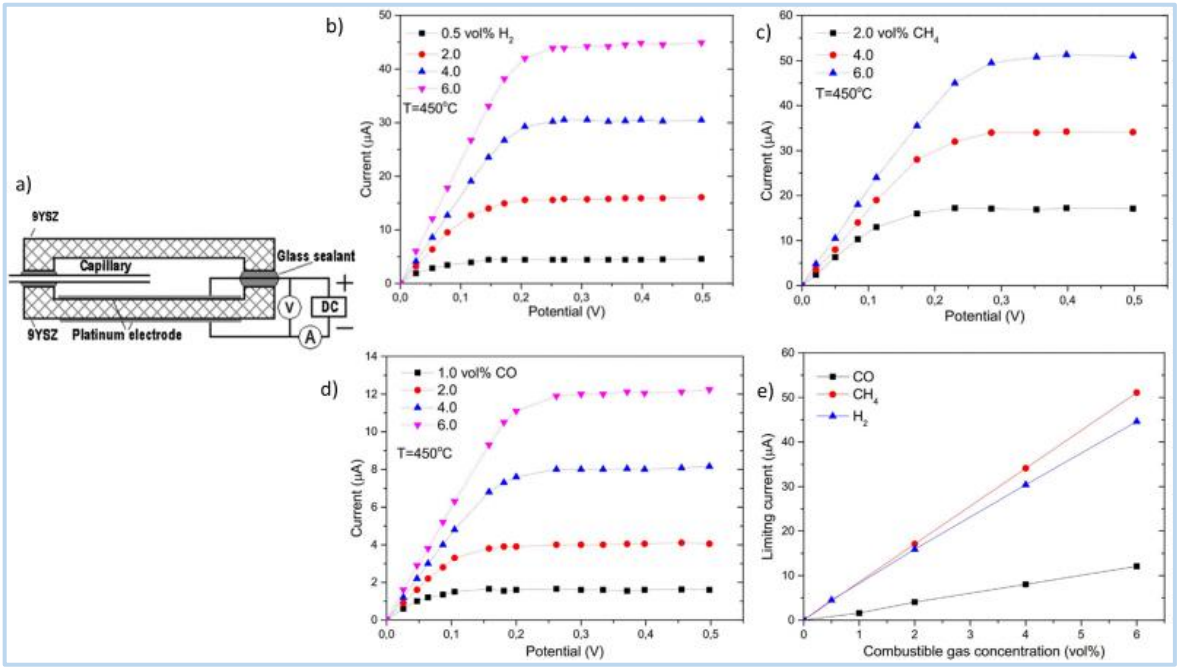

Figure 9: **a)** Schematic illustration of an amperometric gas sensor [166]; **b)** I-V curves for the N_2 + H_2 mixture tested at different concentrations (0.5, 2, 4, and 6 vol% H_2) and 450°C [166]; **c)** I-V curves for the N_2 + CH_4 mixture tested at different concentrations (2, 4, and 6 vol % CH_4) and 450°C [166]; **d)** I-V curves for the N_2 + CO mixture tested at different concentrations (1, 2, 4, and 6 vol% CO) and 450°C [166] and **e)** The limiting current plotted against the concentration of the detected combustible gases [166].

The discussed sensor was exposed to different compositions of combustible gas+N_2, and subsequently, its current-voltage behavior was analyzed. In **Figure 9b**, the plot of current response and applied voltage for some N_2+H_2 mixtures is demonstrated. Note that, the plateau region of I-V curves indicates the establishment of limiting current. As it can be seen, for all N_2+H_2 mixtures (0.5, 2, 4, and 6 vol% H_2), the plateau region starts at 0.2-0.25 V. Additionally, the sensor's total resistance can be determined by the slope of the I-V curve before the plateau region. The total resistance of the sensor for the N_2+6% H_2 mixture is approximately 4 kΩ and contains the electrolyte's resistance (0.5 kΩ) as well as the polarization resistance of the electrodes. Similarly,

the I-V curves displayed in **Figure 9c** for various mixtures of N_2+CH_4 exhibit the same behavior as N_2+H_2 mixtures. More precisely, their plateau region is observed at 0.2-0.25V and the sensor's total resistance for N_2+ 6% CH_4 is approximately 5 kΩ. **Figure 9d** presents the I-V curves for the mixture of N_2+CO, at 1, 2, 4, and 6 vol% CO. The observed values of limiting current are considerably lower than those of the abovementioned mixtures at the same compositions of H_2 and CH_4. This behavior is mainly due to the significantly lower diffusion rate of carbon monoxide in nitrogen in comparison with that of hydrogen and methane. Additionally, the sensor exhibits high total resistance (16 kΩ), in the case of N_2+6%CO, owing to the high polarization resistance of electrodes. **Figure 9e** indicates the linear dependence between limiting current and the concentration of combustible gases, up to 6 vol%, in nitrogen. Last, in the discussed investigation, the diffusion coefficients of detected combustible gases are calculated by means of the equation (7.6). The resulting values are 1.02 ± 0.5, 0.97 ± 0.5, and 3.54 ± 0.6 cm^2/s for CH_4, CO, H_2, respectively [144, 166].

Recently, Kalyakin et al. [167] fabricated an amperometric sensor able to detect CO and CO_2 in N_2 simultaneously. Given that the carbon oxides coexist in many applications, this investigation possesses practical significance offering a more convenient and cost-effective way of sensing compared to two separate devices. This sensor, schematically illustrated in **Figure 10a**, is composed of two electrically isolated cells using YSZ (ZrO_2 + 8mol% Y_2O_3) as an electrolyte along with Pt electrodes. The two cells are identically designed, with the detection of CO taking place in one of the cells and the detection of CO_2 in the other. A dual inner chamber is formed between the cells connected with the outer space through alumina ceramic capillaries. The designed sensor is placed into a tube furnace where the gaseous mixture, N_2 + CO_2 + CO, is supplied. The behavior of the sensor was tested at temperatures between 600°C and 750°C, with the concentration of carbon oxides reaching 10% [167].

In **Figure 10b**, a more detailed schematic illustration of the discussed sensor is presented. As the gaseous mixture (N_2 + CO_2 + CO) is fed to the furnace tube, the sensor fills the inner chambers with the analyzed mixture through the capillaries. The DC source connected with the sensor applies DC voltages to the cells producing oxygen anions. These anions move across the YSZ electrolyte and activate an electrochemical reaction in the interface between YSZ and Pt electrode. More precisely, the applied voltage causes the electrolysis of CO_2 at electrodes 4 and 6 (negatively charged) according to the reaction,

$$CO_2 + 2e^- \rightarrow CO + O^{2-} \quad (7.7)$$

Subsequently, CO is oxidized at electrodes 5 and 7 (positively charged) of the sensor by the produced oxygen ions as follows,

$$CO + O^{2-} \rightarrow CO_2 + 2e^- \tag{7.8}$$

As the voltage applied to the electrodes increases, the sensor current increases, reaching a stationary value corresponding to the limiting current. At this point, the consumption rates of CO and CO_2 are equal to their diffusive supply. At small concentrations of detected gas in the analyzed mixture (below 10%), the limiting current given by the equation (7.5) can be modified as follows [167],

$$I_{lim} = \frac{2FPA}{RTL} D_k X_k \tag{7.9}$$

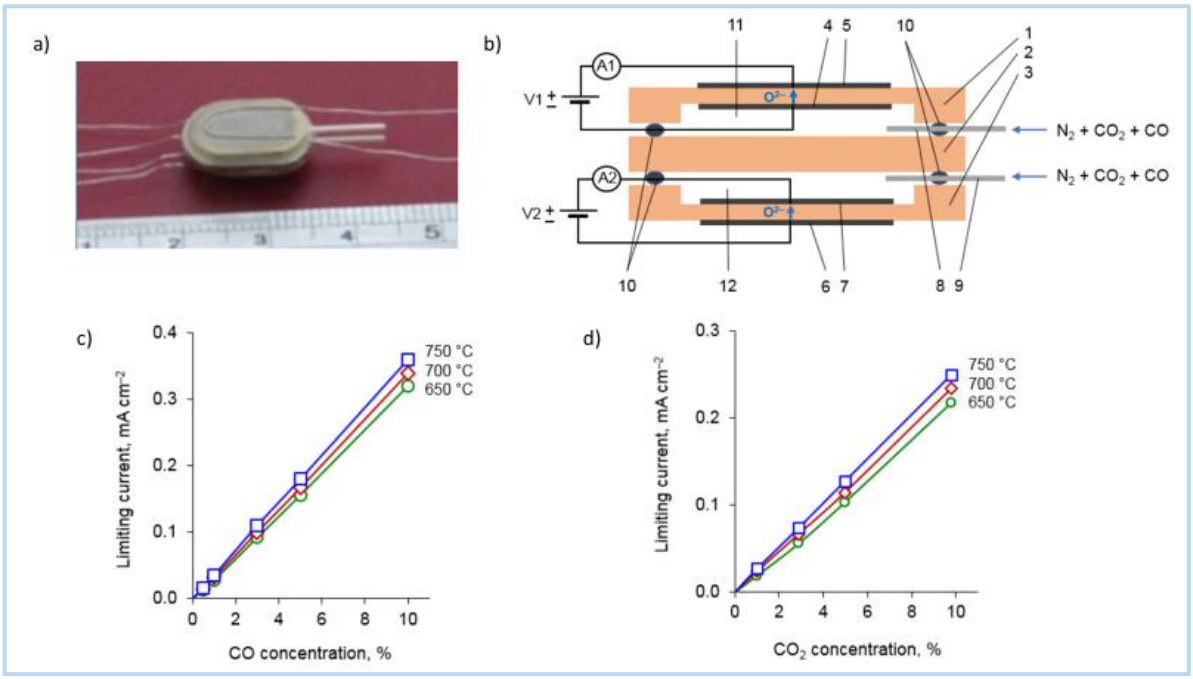

Figure 10: **a)** An image of the produced dual-chamber amperometric sensor [167]; **b)** Schematic illustration of major components of the sensor: (1), (2), and (3) YSZ plates, (4), (5), (6), and (7) Pt electrodes, (8), and (9) alumina ceramic capillaries, (10) sealing glass, (11), and (12) formed inner chambers [167]; **c)** The limiting current plotted against the CO concentration in the tested gaseous mixture of N_2 + CO [167] and **d)** The limiting current plotted against the CO_2 concentration in the tested gaseous mixture of N_2 + CO_2 [167].

Consequently, there is linear dependence between the sensor's limiting current and the concentration of CO and CO_2. This is clearly illustrated in **Figure 10c, d** where the limiting current is plotted against the CO and CO_2 concentrations in N_2 +CO and N_2 + CO_2 gaseous mixtures, respectively. The investigated sensor exhibited adequate long-term stability maintaining stable readings for about 2000h, with a scatter below 1%. Additionally, the

sensor’s transient time didn’t surpass 6min, showing a decent dynamic response. The simultaneous sensing capability of this sensor opens the possibility for applications ranging from food preservation and energy storage to pharmaceutical and medical industries [167].

7.1.2 Carbon Dioxide (CO_2) Sensors

From an environmental viewpoint, the in-situ detection of CO_2 has become a challenge of paramount importance. The uncontrollable emissions of carbon dioxide that are released from combustion processes could be correlated with the ever-increasing number of natural disasters such as flooding and heat waves. Thus, the production of reliable and durable sensors directly detecting CO_2 in aggressive environments plays a vital role in reducing CO_2 emissions. Electrochemical sensors based on solid electrolytes have emerged for carbon dioxide detection due to their considerable advantages against other sensing technologies. The most used electrolytes in CO_2 sensors are NASICON, sodium aluminosilicate glass, and Na-β-alumina. However, the decreased voltage stability of sodium ion conductors as well as the inadequate production process for Na reference electrodes tackle the further development of these sensors. Researchers have tried to create a suitable auxiliary electrode using the abovementioned materials along with Na_2CO_3 as an auxiliary electrode [168]. **Figure 11a** demonstrates the results of sensors employing different materials as auxiliary electrodes [169].

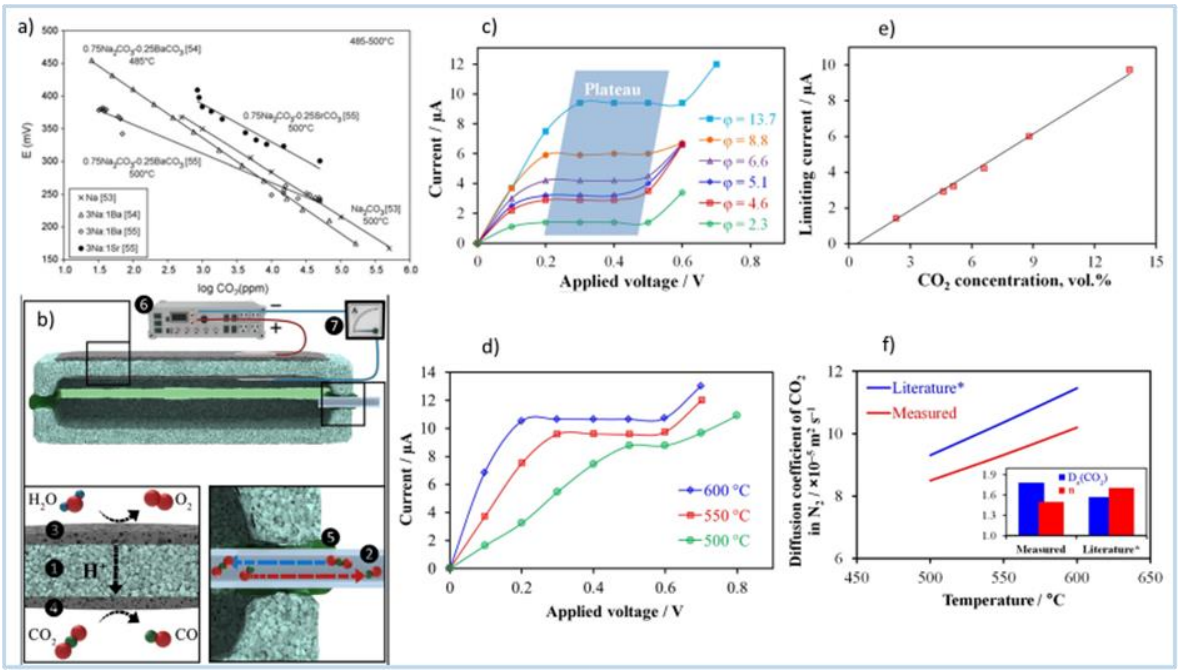

Figure 11: a) Experimental results from sodium ion electrolytes along with auxiliary electrodes based on Na_2CO_3 [169]; **b)** Schematic representation of the carbon dioxide sensor: 1) solid electrolyte ($La_{0.9}Sr_{0.1}YO_{3-\delta}$), 2) capillary, 3) inner Pt electrode, 4) outer Pt electrode, 5) high-temperature glass sealant, 6) DC source, and 7) amperometer [170]; **c)** The I-V curves obtained for different CO_2 concentrations (2.3-13.7 vol %) at 550°C [170]; **d)** The I-V curves for the gas mixture of 84.3% N_2 + 13.7% CO_2 + 2% H_2O at different temperatures [170]; **e)** The limiting current plotted against carbon dioxide concentration [170], and **f)** Comparison of diffusion coefficients obtained by experimental measurements and literature data [170].

Recently, a proton-conducting electrolyte has been reported by Kalyakin et al. for carbon dioxide detection at 500-600°C. More precisely, a Sr-doped $LaYO_3$ ($La_{0.9}Sr_{0.1}YO_{3-\delta}$) electrolyte was manufactured and tested in an amperometric CO_2 sensor. The investigated electrolyte material was prepared and applied to the sensor in the form of square plates in conjunction with platinum electrodes in one of the manufactured plates. A high-temperature glass sealant is used to seal the inner chamber between the plates. Thus, the interaction between the inner chamber and the outside atmosphere is realized exclusively through the capillary. The sensor is heated to reach the suitable operating temperature and then is exposed to the N_2+2% H_2O+CO_2 gas mixture. The operation procedure starts with applying a DC voltage to the electrodes, as shown in **Figure 11b**. Thus, water reacts at the external electrode generating protons, electrons, and oxygen. The protons penetrate the sensor's chamber via the proton-conducting electrolyte and participate in the reduction of CO_2. The water decomposition at the external electrode and the reduction of CO_2 are expressed by the following reactions,

$$H_2O \rightarrow \frac{1}{2}O_2 + 2H^+ + 2e^- \qquad (7.10)$$

$$2H^+ + CO_2 \rightarrow H_2O + CO - 2e^- \quad (7.11)$$

As the applied voltage increases, the current response and the rate of hydrogen permeation in the sensor also increase. In parallel, the concentration of carbon dioxide inside the chamber constantly lessens. Considering that there is moisture in the analyzed gas, the water decomposition can continuously happen at the external electrode. Nevertheless, the reduction of CO_2 (7.11) is limited by the CO_2 content inside the sensor and by the CO_2 supply through the capillary. At an applied voltage, the limiting current is observed, indicating the establishment of steady-state conditions. The mathematical expression of limiting current is given by the following equation [170],

$$I_{lim} = \frac{2FPA}{RTL} D_{co_2} X_{co_2} p_{co_2} \quad (7.12)$$

Figure 11c presents the I-V curves plotted at different carbon dioxide concentrations (2.3-13.7 vol%). As shown, all the characteristic curves form a plateau region at the applied voltage values ranging from 0.2 to 0.4V, with the limiting current reaching values up to 10μA. This figure also indicates that the increase in CO_2 concentration results in the formation of a plateau region at higher voltage values. **Figure 11d** demonstrates the I-V curves for the gas mixture containing the highest investigated CO_2 content (84.3% N_2 + 13.7% CO_2 + 2% H_2O) at different temperatures. As observed, at a range of applied voltage between 0.2 and 0.5 V, all curves form a plateau region corresponding to the limiting current. Note that the increase in temperature broadens the width of the plateau region, reaching steady-state conditions at lower voltages. **Figure 11e** depicts the calibration curve obtained by collecting the values of limiting current at the plateau region for the studied CO_2 concentrations. The linear dependence between the limiting current and CO_2 content enables the measurement of carbon dioxide in gas mixtures with unknown concentrations. Generally, the diffusion coefficient of equation (7.12) can be calculated by knowing the temperature and pressure at the operating conditions as follows,

$$D_{CO_2} = D_0(CO_2) \cdot \frac{P_0}{P} \left(\frac{T_0}{T}\right)^n \quad (7.13)$$

where P_0, T_0, and D_o are the pressure, temperature, and diffusion coefficient at standard conditions, respectively. In **Figure 11f**, the measured diffusion coefficient is plotted against the temperature and combined with the diffusion coefficient obtained by literature data. In addition, the comparison between experimental and literature results is realized for the diffusion coefficient under standard conditions. As shown, there is an agreement between the

measured and literature results verifying the reliability and the prospects of the discussed method of diffusion coefficient calculation [170].

Chapter 8

High temperature sensors for hydrogen detection

Abstract

Hydrogen sensors, especially those operating at high temperatures, are an indispensable element of the emerging hydrogen economy. In the present review, the electrochemical hydrogen sensors detecting hydrogen at high temperatures and harsh environments are thoroughly discussed. Their technology is now regarded as one of the most reliable and efficient, with adequate prospects for further development. Emphasis is given to hydrogen sensors based on solid oxide electrolytes, in particular oxygen ion and proton conductors. The review is devoted to potentiometric, amperometric, and combined amperometric-potentiometric hydrogen sensors, analyzing their configuration, principle of operation, and the applied solid electrolytes and electrodes. The experimental data of investigations working on these sensors are also presented and analyzed. Additionally, an amperometric sensor designed to detect hydrogen and steam in atmospheric air through a two-stage procedure is presented. The configuration of the fabricated YSZ-based amperometric sensor operating at 700°C and the obtained experimental data are described.

8.1 Introduction

Among the reducing gases, hydrogen (H_2) is undoubtedly regarded by the scientific and industrial communities as one of the most important. Participating in many chemical processes, hydrogen includes a plethora of applications in industries such as power generation, petrochemical, transportation, and medical. Currently, hydrogen is gaining widespread interest as a sustainable energy carrier used in fuel cells for power generation and automotive applications. The emissions of fuel cells are considerably less polluting than those of fossil fuels contributing to the mitigation of environmental pollution. Thus, hydrogen as a fuel has the potential to meet the energy demands and, simultaneously, ensure environmental and human safety. The development of hydrogen sensing technologies is an integral part of the hydrogen energy future. More precisely, hydrogen sensors are required to detect hydrogen leaks and measure hydrogen content during

storage, production, and transportation. Consequently, hydrogen sensors can be used in various applications such as hydrogen production plants, storage tanks, and automotive vehicles, playing a vital role in their operation [171, 172].

Hydrogen possesses unique properties compared with combustible gases, such as propane, methane, and gasoline vapor. More precisely, it is the lightest element having a low boiling point (20.39 K) and, simultaneously, high buoyancy. Concerning its combustion properties, hydrogen has a considerably higher heat of combustion than other combustible gases (142 KJ/g H_2), with the ignition temperature in air ranging from 520 to 580 °C. Hydrogen also has minimum ignition energy of about 0.02 mJ combined with a broad flammable range (4-75 vol %) when mixed with air. Thus, in case of a leak, hydrogen can be easily ignited. The detection of hydrogen and the quantification of its concentration are only realized through suitably designed sensors as it is an odorless, colorless, and tasteless gas. These sensors should provide accurate, fast, and selective measurements of hydrogen gas under the operating conditions of the corresponding application. However, many industrial fields such as metallurgy, petrochemical, nuclear, and manufacturing require hydrogen sensors able to operate at high temperatures and aggressive environments. For instance, hydrogen monitoring is essential in molten aluminum during the casting process [173, 174] or in nuclear power stations for the safety of nuclear reactors [171, 172].

Several hydrogen sensing technologies have emerged because of the ongoing scientific research. Electrochemical hydrogen sensors are among the well-established technologies, having a considerable impact on the hydrogen sensor market. These sensors use solid electrolytes based on oxide ion and proton-conducting materials to detect hydrogen in high-temperature environments. Generally, the gas sensors utilizing oxide ion and proton conductors as solid electrolytes find application in many industries such as automotive and steelmaking. This widespread use arises from the remarkable properties of solid-state electrolytes. More precisely, they are stable compounds able to withstand harsh operating conditions [175]. In addition, they present increased ionic conductivity because of the elevated working temperatures.

Depending on the response signal, electrochemical hydrogen sensors can be divided into potentiometric, amperometric, and combined amperometric-potentiometric sensors. The potentiometric hydrogen sensors include the equilibrium potentiometric sensors (Nernst type) and the non-equilibrium potentiometric sensors (mixed potential sensors). In potentiometric

hydrogen sensors, the voltage between the electrodes is the response signal and is logarithmically related to the concentration of hydrogen. In amperometric hydrogen sensors, the output current caused by an externally applied voltage provides information about the hydrogen content in the sensor. The detection of hydrogen with potentiometric sensors using oxygen-conducting solid electrolytes has been thoroughly investigated by researchers. The well-established YSZ along with selective oxide electrodes have been intensively reported for hydrogen measurement [176]. Despite the numerous investigations, the detection of hydrogen with these devices remains problematic. The problem mainly pertains to the selection of a reference electrode designed to maintain a stable potential throughout the sensor's operation. This is not easy, given that the operating temperatures of these sensors exceed 600°C [144, 177].

On the contrary, the detection of hydrogen by means of proton-conducting solid electrolytes is gaining more and more attention from several research groups. This class of solid electrolytes presents adequate physical and chemical durability under harsh working environments, expanding the range of high-temperature applications. For instance, high-temperature proton conductors have been implemented in hydrogen sensors and examined for application in steelmaking and aluminum casting processes [178, 179]. Generally, the investigation of proton conductors has mainly been focused on oxide materials based on $BaCeO_3$ and $BaZrO_3$ because they combine high conductivity and stability [18, 29, 47, 48]. Nevertheless, alternative solid-state materials with lower proton conductivity, such as $LaNbO_4$ and $Ba_2In_2O_5$, have also drawn vast attention. Note that the abovementioned materials should meet strict requirements to be used as electrolytes in hydrogen sensors. More precisely, they should present pure ionic conductivity, high stability in aggressive environments, and similar thermal expansion with the sensor's components [151].

8.2 Types of hydrogen sensors

8.2.1 Potentiometric hydrogen sensors

Equilibrium potentiometric sensors

Iwahara et al. [180] fabricated and tested a Nernstian-type hydrogen sensor using a proton conducting electrolyte based on $BaCeO_3$ at 200-900°C. More precisely, the ceramic material, with the chemical composition of $BaCe_{0.9}Nd_{0.1}O_{3-\delta}$ (BCN), was applied in a concentration cell including two platinum electrodes (Pt | BCN | Pt). The manufactured sensor used pure hydrogen (pH_2 =1 atm) as a reference atmosphere and a mixture containing hydrogen and argon ($pH_2 = 10^{-4}$-1 atm) as the analyzed atmosphere. The experimental measurements of EMF values conformed

to the theoretical values given by the Nernst equation, differing, however, from cell to cell. Subsequently, Iwahara's group used the composite $AlPO_4 \cdot xH_2O$-$La_{0.4}Sr_{0.6}CoO_3$ (AP-LSC) as a solid standard material, and the proton-conducting electrolyte $CaZr_{0.9}ln_{0.1}O_{3-\delta}$ (CZI) in order to construct a Nernstian-type hydrogen sensor. The produced sensor based on the H_2 + Ar, Pt | CZI | Pt, AP-LSC cell proved suitable for hydrogen concentration analysis, showing high accuracy, fast response, and stable EMF response even in CO_2-containing gas atmospheres [181]. Recently, Mn-doped $CaZrO_3$ (CZM) was examined by Okuyama et al. [182] for application as an electrolyte in an EMF-type hydrogen sensor. They constructed and evaluated a galvanic cell where the reference atmosphere is wet air, and the analyzed atmosphere is a wet mixture containing hydrogen and argon. The obtained experimental data of the wet H_2 + Ar, Pt | $CaZr_{0.95}Mn_{0.05}O_{3-\delta}$ | Pt, wet air cell were in agreement with the operation principles of a hydrogen sensor based on the Nernst equation. Considering also its fast dynamic response, the developed sensor with the proton-conducting electrolyte (CZM) has the potential to detect hydrogen in hydrogen-rich atmospheres [53, 141].

Mixed potential sensors

During the last decades, many research groups have been devoted to the detection of hydrogen via mixed potential sensors. The majority of reported mixed potential hydrogen sensors use YSZ as a solid electrolyte and platinum as a reference electrode (RE). Thus, the investigations on these sensors have mainly focused on the development of suitable sensing electrodes. Vogel et al. [183] tested different sensing materials concluding that the Pt/Au electrode is appropriate for SE in these sensors.

Later, Tan et al. [184] coated a Pt sensing electrode with a catalyst layer containing a mixture of CuO, ZnO, and Al_2O_3. The produced hydrogen sensor operates at 415-600 ℃ and can detect hydrogen at a few ppm (0-150 ppm). However, the considerable cost of noble metals-based SEs shifted the scientific research towards the use of simple metal oxides such as ZnO as SEs [185, 186]. Following this line, Fadeyev et al. [187] tested different simple oxides-based SEs, such as SnO_2-SE and Cr_2O_3-SE, using an YSZ-based electrochemical sensor with a silver reference electrode.

Yamaguchi et al. fabricated a mixed potential sensor for hydrogen detection at high temperatures (600 ℃) using a pair of SEs made up of SnO_2 (+30 wt. % YSZ) and NiO-TiO_2. This sensor demonstrated adequate H_2 selectivity and sensitivity, reducing, at the same time, the response of C_3H_8 [188]. The same group also applied a catalyst layer of Cr_2O_3 in the

previously used SnO_2 (+30 wt. % YSZ) SE and an intermediate layer of Al_2O_3 that prevented the contact between the catalyst layer and the SE [189]. Among other examined SEs, indium tin oxide (ITO) has been intensively used and tested in mixed potential hydrogen sensors [190, 191, 192]. Furthermore, metal tungstates such as $ZnWO_4$ [193], $MnWO_4$ [194], $CdWO_4$ [195], and $COWO_4$ [196] have been reported as alternative SEs [148, 149] .

8.2.2 Amperometric hydrogen sensors

Amperometric hydrogen sensors are gathering momentum due to their specific advantages over potentiometric sensors. Their principle of operation is based on a linear dependence between the observed limiting current and the hydrogen concentration. This relation facilitates the measurement of hydrogen content, allowing the use of a calibration curve. Thus, they offer adequate accuracy in analyzing gases with medium and high hydrogen content. In addition, the fact that they don't need a reference atmosphere enhances, in some cases, their reliability. Note that, amperometric sensors are equipped with a diffusion barrier, which plays a vital role in their operation, as it determines the diffusion flow of the analyzed gas from the outer to the inner chamber of the sensor. Conventionally, the diffusion barrier can be the porosity of the solid electrolyte or a laser-drilled hole.

Recent reports have fabricated different diffusion barriers in the form of a dense layer with materials exhibiting mixed ionic-electronic conductivity [197, 198, 199, 200]. However, the parameters of this type of diffusion barrier are not easily controlled and reproduced. This is an important limitation, given that the characteristics of the sensor, such as the limiting current, are determined by these parameters [177].

Proton-conducting solid electrolytes were used by Kalyakin et al. in order to synthesize three amperometric H_2 sensors. More precisely, the sensors made up of $La_{0.95}Sr_{0.05}YO_3$, $CaTi_{0.95}Sc_{0.05}O_3$, and $CaZr_{0.9}Sc_{0.1}O_3$ were tested in the gas mixture of H_2 + N_2 + H_2O at 800°C. The three manufactured sensors have the same configuration, except for the applied solid electrolyte, as shown in **Figure 12a**. Glass sealant was used to connect the two plates of the solid electrolyte, synthesizing an inner chamber between them. The plate of one of the solid electrolytes is composed of Pt electrodes installed on its internal and external sides. The diffusion barrier of these sensors is the leaked gas mixture between the sealant cells and across the porous solid electrolyte. The sensors are installed in a furnace to acquire the required operating temperature, which is about 800°C [177].

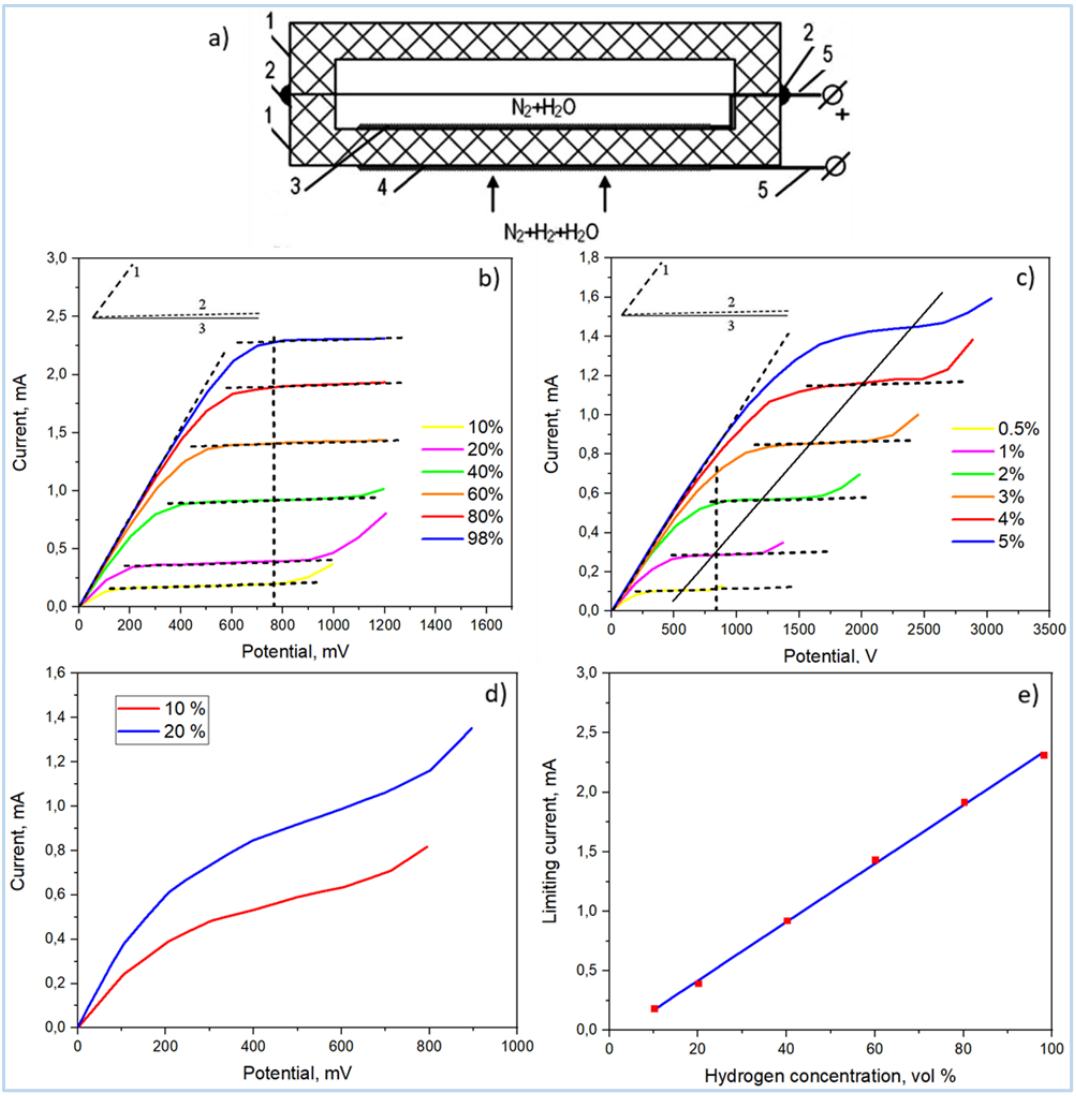

Figure 12: **a)** Schematic illustration of the discussed amperometric hydrogen sensor: 1- solid electrolyte (proton conductor), 2- glass sealant, 3- internal Pt electrodes, 4- external Pt electrode, and 5- Pt leads [177]; **b)** The I-V curves for sensor 1 using $La_{0.95}Sr_{0.05}YO_3$ as solid electrolyte at different hydrogen concentrations in the gas mixture of N_2+2%H_2O+H_2 (800°C) [177]; **c)** I-V curves for the sensor 2 using $CaZr_{0.9}Sc_{0.1}O_3$ as solid electrolyte at different hydrogen concentrations in the gas mixture of N_2+2%H_2O+H_2 (800°C) [177]; **d)** I-V curves for the sensor 3 using $CaTi_{0.95}Sc_{0.05}O_3$ as solid electrolyte at different hydrogen concentrations in the gas mixture of N_2+2%H_2O+H_2 (800°C) [177] and **e)** The limiting current of sensor 1 plotted against the hydrogen concentration [177].

The sensor is exposed to the gas mixture of N_2 + H_2O + H_2 and fills its inner chamber. Subsequently, a DC voltage is applied to the platinum electrodes in order to electrochemically pump hydrogen out of the sensor's inner space. Thus, the hydrogen is oxidized, producing protons and electrons at the inner electrode according to the following reaction,

$$H_2 \rightarrow 2H^+ + 2e^- \tag{8.1}$$

The producing protons are transported to the external electrode via the proton conductor and form hydrogen molecules in conjunction with the electrons as follows,

$$2H^+ + 2e^- \rightarrow H_2 \quad (8.2)$$

The rate of hydrogen pumped out increases with the applied voltage increase, resulting in the decrease of hydrogen amount in the inner chamber of the sensor. The occurred voltage-current curves of these sensors are affected by different parameters. More precisely, the ohmic resistance of the solid electrolyte and the polarization resistance of electrodes control the slope of V-I curves. In addition, the features of the sensor's diffusion barrier and the composition of the studied gas mixture affect the limiting current. The decrease of hydrogen amount at the first stage of operation leads to an increase in the electrode polarization resistance and consequently, to an increase in the cell resistance. For this reason, the slope of V-I curves lessens as the applied voltage increases. **Figure 12(b-d)** demonstrate the V-I curves of the sensors 1, 2, and 3 with the applied solid electrolytes $La_{0.95}Sr_{0.05}YO_3$, $CaZr_{0.9}Sc_{0.1}O_3$, and $CaTi_{0.95}Sc_{0.05}O_3$, respectively. As seen in **Figure 12b**, sensor 1 was tested at high H_2 concentrations (10-98%) and reaches a plateau area representing the limiting current. Similarly, sensor 2 tested at lower H_2 concentrations <5% reaching a plateau region shown in **Figure 12c**. However, the V-I curves presented in **Figure 12d** for sensor 3 don't show a plateau area because of the appearance of electronic conductivity in the solid electrolyte. Thus, the sensor based on $CaTi_{0.95}Sc_{0.05}O_3$ is not applicable for hydrogen sensing. **Figure 12e** reveals the linear dependence between the limiting current and the hydrogen concentration for sensor 1. Consequently, the studied amperometric sensor can be used for hydrogen detection at high temperatures; the solid electrolyte $La_{0.95}Sr_{0.05}YO_3$ is suitable for gas mixtures with high hydrogen concentration and the $CaZr_{0.9}Sc_{0.1}O_3$ is more effective for low hydrogen concentrations [177].

8.2.3 Combined Amperometric-Potentiometric H_2 Sensors

In 2015, the proton conducting material, $La_{0.9}Sr_{0.1}YO_{3-\delta}$, was examined for application in a hydrogen amperometric sensor. The properties of this material allow its application together with an oxygen-conducting electrolyte. More precisely, the discussed sensor comprises two electrochemical cells, one is made up of the well-known YSZ, while the other one is composed of the $La_{0.9}Sr_{0.1}YO_{3-\delta}$. These materials play the role of the electrolyte and have the form of discs with a recess on one of their sides. Each cell employs platinum electrodes placed on its opposite sides. The inner chamber, created by the two cells, is connected with the analyzed gas through a ceramic capillary. **Figure 13a** demonstrates the configuration of the present amperometric sensor and **Figure 13b** shows the fabricated sensor [151].

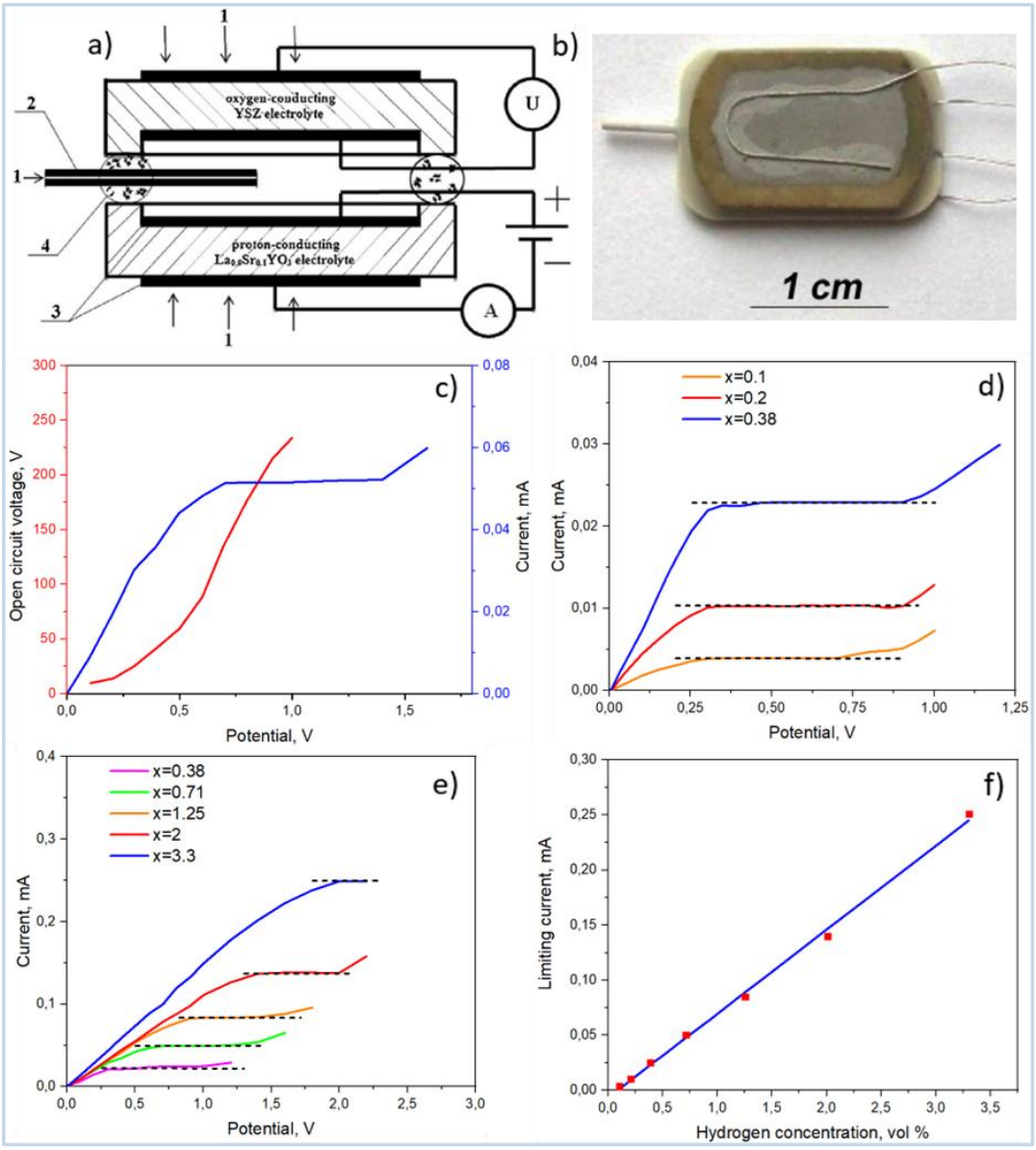

Figure 13: **a)** The configuration of the amperometric H_2 sensor: 1) the analyzed gas, 2) ceramic capillary, 3) Pt electrodes, and 4) glass sealant [151]; **b)** photo of the fabricated sensor [151]; **c)** I and OCV related to the voltage for 0.7 vol % H_2 + N_2 at the temperature of 550°C [151]; **d)** I-V curves for low hydrogen concentration (0.1-0.38 vol % H_2) at 550 °C [151]; **e)** I-V curves for the hydrogen concentrations ranging from 0.38 to 3.3 vol % H_2 in the H_2 + N_2 at 550°C [151] and **f)** The limiting current plotted against the hydrogen concentration [151].

The application of a DC voltage at the electrodes of the cell with the LSY electrolyte starts the process described above, known as hydrogen electrochemical pumping. The hydrogen content inside the sensor chamber constantly lessens until a negligible value. At this point, the observed current corresponds to the limiting current, which can be calculated by the equation (7.5) (k=H_2 and z=2) as follows,

$$I_{lim} = \frac{2FPAD_{H_2}}{RTL} X_{H_2} \qquad (8.3)$$

The cell with the YSZ-electrolyte operates as an oxygen concentration cell, detecting the changes in oxygen partial pressure in the analyzed gas inside the sensor chamber. Oxygen is included in the analyzed gas not in the form of molecular oxygen, but as bonded oxygen because of the presence of steam according to the reaction:

$$H_2O \overset{K}{\rightarrow} H_2 + 0.5O_2 \tag{8.4}$$

The oxygen partial pressure, pO_2, is given by the following equation:

$$p_{O_2} = \left(\frac{Kp_{H_2O}}{p_{H_2}}\right)^2 \tag{8.5}$$

where K expresses the equilibrium constant of the reaction (8.4), and pH_2O and pH_2 are the partial pressures of steam and hydrogen, respectively. The continuous decrease of hydrogen content in the sensor chamber causes the decrease of hydrogen partial pressure. The second cell continuously monitors this change through the generated open circuit voltage (OCV), obeying the Nernst equation. The water vapor partial pressure inside and outside the sensor's chamber are equal, so the Nernst equation can be modified by substituting equation (8.5) as follows [151],

$$E = -\frac{RT}{2F}\ln\left(\frac{p''_{H_2}}{p'_{H_2}}\right) \tag{8.6}$$

Figure 13c demonstrates the current and the measured OCV of equation (8.6) against the applied voltage for the gas mixture of 0.7 vol % H_2 + N_2 at 550°C. As it can be seen, the current produced in the LSY-based cell increases with the applied voltage. At a voltage value, U~0.7 V, the current stabilizes in the so-called limiting current, where the hydrogen concentration is estimated at 8ppm. However, the current increases again when the applied voltage surpasses the value of 1.5 V. This phenomenon can be explained either by the presence of electrical conductivity in the LSY or by the beginning of the material's partial decomposition. Concerning the measured OCV, the applied voltage induces a smooth increase in OCV at the beginning of the sensing process. However, OCV quickly increases when the hydrogen content inside the chamber tends to zero.

In **Figure 13d**, the I-V curves of the discussed sensor are presented for low hydrogen concentrations (0.10-0.38 vol % H_2) in the H_2 +N_2 gas mixture at 550°C. Similarly, **Figure 13e** presents the I-V curves for higher hydrogen concentrations (0.38-3.3 vol % H_2). As it is observed, the applied voltage in which the curves stars forming a plateau region increases with the hydrogen concentration increase. Thus, the present sensor is suitable for the detection of small hydrogen amounts (0.1-3.3 vol %) in N_2 atmospheres at 500-600°C. This is

verified by **Figure 13f**, which demonstrates the linear dependence between hydrogen amount in the gas mixture and the limiting current [151].

In 2016, Kalyakin et al. fabricated a combined-amperometric potentiometric hydrogen sensor aiming to investigate the behavior of $BaCe_{0.7}Zr_{0.1}Y_{0.2}O_{3-\delta}$ as a solid electrolyte in this device. $BaCe_{0.7}Zr_{0.1}Y_{0.2}O_{3-\delta}$ (BZCY) was selected for electrolyte as it is regarded as one of the most promising high-temperature proton conductors. More precisely, it shows high ionic conductivity and sufficient stability in aggressive environments. The sensor was designed for measuring the hydrogen content in wet (2% H_2O) mixtures of N_2 + H_2 at 450-550°C. The configuration of the sensor contains two electrochemical cells composed of the BZCY-based electrolyte and platinum electrodes. The capillary connects the inner chamber formed between the cells with the analyzed gas mixture. In addition, a high-temperature glass sealant is employed in order to seal the inner chamber of the sensor and separate the two solid electrolytes [144, 201].

Figure 14a presents the amperometric mode of the sensor, and **Figure 14b** exhibits the potentiometric one. Cell-1 is designed to work in amperometric regime acting as an electrochemical hydrogen pump, whereas cell-2 is the potentiometric part of the sensor. The polarity of the voltage applied on cell-1 determines the operating mode of the sensor (amperometric or potentiometric). During the potentiometric mode of the sensor, a DC voltage is applied to the electrodes of cell 1, forcing hydrogen to electrochemically permeate from the outer space of the sensor to the inner chamber. This process is expressed as follows,

External electrode: $$H_2 \rightarrow 2H^+ + 2e^- \quad (8.7)$$

Internal electrode: $$2H^+ + 2e^- \rightarrow H_2 \quad (8.8)$$

The hydrogen content inside the sensor increases, displacing N_2 through the capillary. Thus, an atmosphere with pure hydrogen is established in the sensor's chamber, namely $p_{H_2}^{in} = 1$. The constant electrochemical pumping of hydrogen generates a difference in hydrogen partial pressures between the inner chamber and the outer atmosphere of the sensor. Cell-2 detects an electric potential difference (EMF) caused by this difference in partial pressures. This potential obeys the Nernst equation described by the equation (8.6). As there is only hydrogen inside the sensor's chamber, the measured EMF indicates the concentration of hydrogen in the analyzed gas. The dependence between the observed EMF and the applied voltage at cell-1 is demonstrated in **Figure 14c**. The EMF-V curves are plotted for different hydrogen concentrations at 500°C. As shown, in the first stage, the increase in applied voltage results in a noticeably increase in EMF. This is due to the ever-increasing difference in hydrogen partial

pressure generated by the hydrogen pumping inside the chamber. Subsequently, at an applied voltage of about 2-2.5, the EMF maintains a steady and maximum value owing to the pure hydrogen atmosphere in the chamber [144, 201].

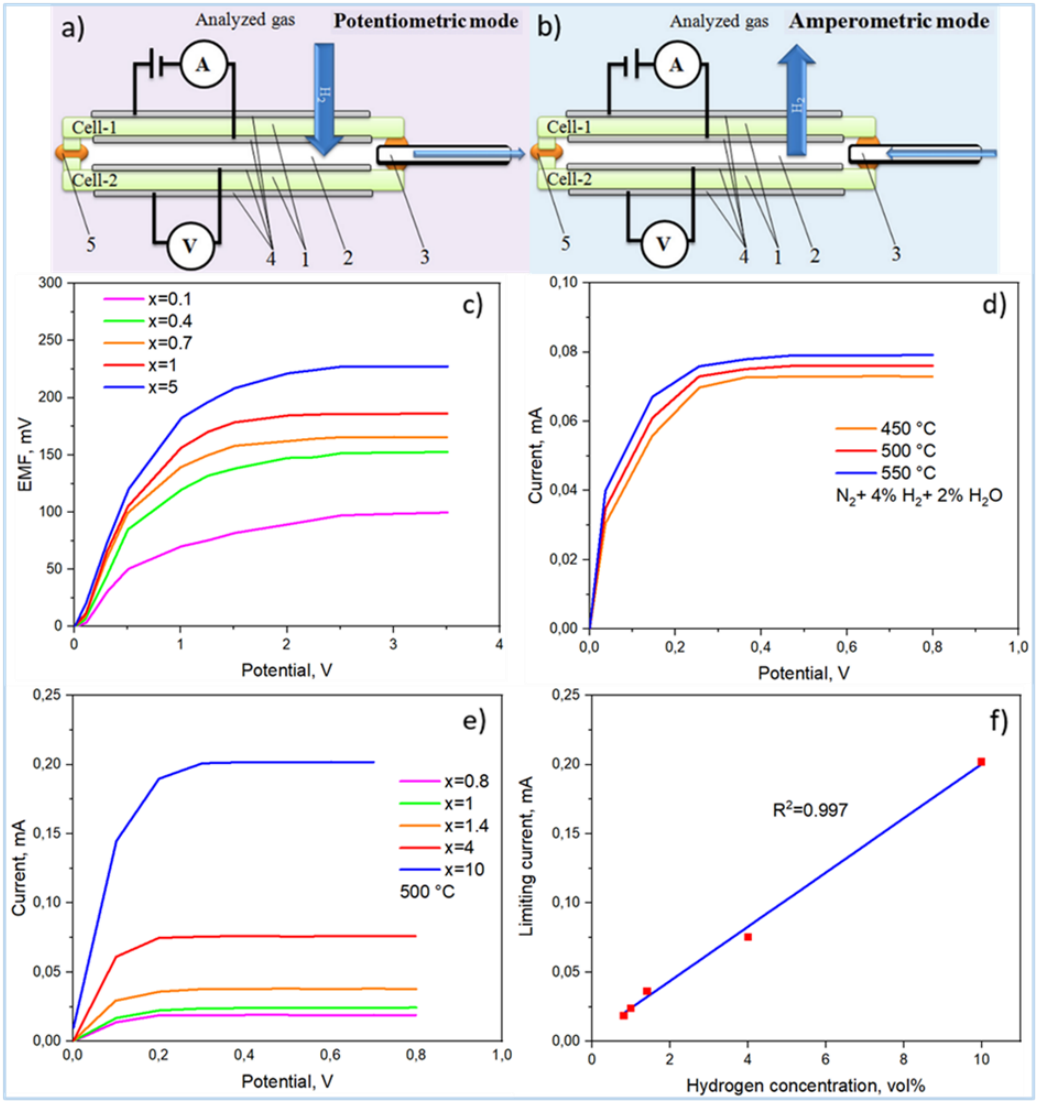

Figure 14: **a)** Schematic illustration of the potentiometric mode of the sensor: 1) solid electrolyte based on BZCY, 2) inner chamber, 3) ceramic capillary, 4) Pt electrodes, 5) high-temperature glass sealant [201]; **b)** Schematic illustration of the amperometric mode of the sensor [201]; **c)** EMF-V curves plotted for different hydrogen concentrations (x=0.1-5 vol% H_2) at 500°C [201]; **d)** I-V curves of the amperometric part for the gas mixture N_2 + 4%H_2 + 2%H_2O at different operating temperatures [201]; **e)** I-V curves plotted for different hydrogen concentrations (x=0.8-10 vol% H_2) at 500°C [201] and **f)** The limiting current response of the amperometric mode against the hydrogen concentration [201].

In the amperometric mode of the sensor, the applied DC voltage at cell-1 removes the hydrogen from the inner chamber of the sensor. More precisely, the reaction (8.7) is realized on the internal electrode of cell-1 and the reaction (8.8) on the external electrode. **Figure 14d** exhibits the I-V curves of the amperometric mode for the gas mixture N_2 + 4%H_2 + 2%H_2O at different temperatures. The limiting current increases with temperature, which is explained

by the proportional dependence between the temperature and diffusion coefficient given by equation (7.6). **Figure 14e** presents the I-V curves for the mixture of N_2 + x%H_2 + 2%H_2O at 500°C. The limiting current response is plotted against the hydrogen concentration in **Figure 14f**. As it can be seen, there is linear dependence between these two parameters. Therefore, the amperometric mode can also be used for hydrogen analysis [201].

8.3 Amperometric sensor for hydrogen and steam detection

The detection of hydrogen through electrochemical sensors working under the potentiometric or amperometric regime has been thoroughly discussed in the previous subchapter. Concerning the detection of steam, there are several reports of sensors using oxygen-ion [202] and proton conductors [203- 209] as solid electrolytes. Recently, Kalyakin et al. [210] constructed and tested an amperometric sensor that successfully detects water vapor and hydrogen in the air at 700°C. This sensor uses a solid electrolyte composed of the well-known oxygen ion conductor, YSZ, with the composition $0{,}9ZrO_2+0{,}1Y_2O_3$. The configuration and photograph of the discussed amperometric sensor are demonstrated in **Figure 15a** and **Figure 15b**, respectively. One of the YSZ plates that form the solid electrolyte is equipped with Pt electrodes at its opposite sides, along with Pt wires as current leads. The inner chamber between the plates is sealed by a high-temperature glass sealant, while a thin ceramic capillary plays the role of the diffusion barrier.

As is shown in **Figure 15a**, the discussed sensor works under the amperometric regime. More precisely, a positive potential is applied to the outer electrode, causing the electrochemical pumping of oxygen out of the sensor's chamber. This process is expressed by the following reactions,

Internal electrode: $$^1/_2\, O_2 + 2e^- \rightarrow O^{2-} \quad (8.9)$$

External electrode: $$O^{2-} \rightarrow {}^1/_2\, O_2 + 2e^- \quad (8.10)$$

As the applied voltage increases, the rate of transferred oxygen ions through the YSZ electrolyte increases. Thus, the sensor current increases until a specific voltage value, where the limiting current appears. If this current is known, the concentration of oxygen in the analyzed gas mixture is calculated as follows,

$$I_{lim} = -\frac{4FD_{O_2}SP}{RTL}\ln(1 - X_{O_2}) \quad (8.11)$$

where I_{lim} is the limiting current, Xo_2 is the mole fraction of oxygen, Do_2 is the diffusion coefficient of oxygen, P is the absolute gas pressure, T is the absolute temperature, F is the Faraday constant, R is the gas constant, L is the length of the diffusion barrier, and S is the area of the diffusion barrier. For oxygen concentrations of about Xo_2=0.2, the equation (8.11) is simplified as follows,

$$I_{lim} = \frac{4kFD_{O_2}SP}{RTL} X_{O_2} \tag{8.12}$$

where k is a coefficient that expresses the logarithmic dependence between the limiting current and oxygen concentration. The standard oxygen concentration in dry air is 20.9 vol % or Xo_2=0.209 expressed as a mole fraction. The presence of steam and/or hydrogen in the analyzed gas mixture decreases the oxygen concentration in the air. Therefore, the limiting current also decreases as steam and hydrogen concentrations increase. Nevertheless, the detection of hydrogen in a gas mixture containing both hydrogen and steam is a difficult process. The problem lies in the presence of steam which causes a further decrease in the oxygen concentration in comparison with the dry air-hydrogen mixture. A possible solution for hydrogen detection is air-drying before the analysis using zeolite or phosphorus pentoxide P_2O_5. However, Kalyakin et al. proposed a two-stage procedure through which the concentrations of steam and hydrogen in atmospheric air can be calculated. In the first stage, the limiting current is measured in atmospheric air, while in the second stage, the limiting current is measured in dried atmospheric air. Thus, the observed limiting currents are used for the calculation of oxygen concentrations in a wet mixture of H_2 + atmospheric air and dried hot atmospheric air as follows [210],

$$X'''_{O_2} = X^0_{O_2} \frac{I_{lim}(X'''_{O_2})}{I_{lim}(X^0_{O_2})} \tag{8.13}$$

$$X''_{O_2} = X^0_{O_2} \frac{I_{lim}(X''_{O_2})}{I_{lim}(X^0_{O_2})} \tag{8.14}$$

where X''_{O_2} is the oxygen concentration in dried atmospheric hot air, X'''_{O_2} is the oxygen concentration in a hydrogen-containing mixture of hot atmospheric air, and $X^0_{O_2}$ is the oxygen concentration in dry air ($X^0_{O_2}$=0.209). Knowing the abovementioned oxygen concentrations, the mole fractions of steam and hydrogen in atmospheric air are calculated by the following equations:

$$X_{H_2O} = \frac{X''_{O_2} - X'''_{O_2}}{X''_{O_2}} \tag{8.15}$$

$$X_{H_2} = 2\frac{X^0_{O_2} - X''_{O_2}}{1 + X^0_{O_2}} \tag{8.16}$$

Moreover, the hydrogen concentration in humid air can be directly calculated if the water-vapor content in the air is known using, for example, a moisture meter. Solving equation (8.15) for oxygen concentration in dried air and substituting in equation (8.16), the mole fraction of hydrogen is given by the following equation:

$$X_{H_2} = 2\frac{X_{O_2}^0 - X_{O_2}^0 X_{H_2O} - X_{O_2}'''}{1 + X_{O_2}^0 - X_{O_2}^0 X_{H_2O} - X_{H_2O}} \tag{8.17}$$

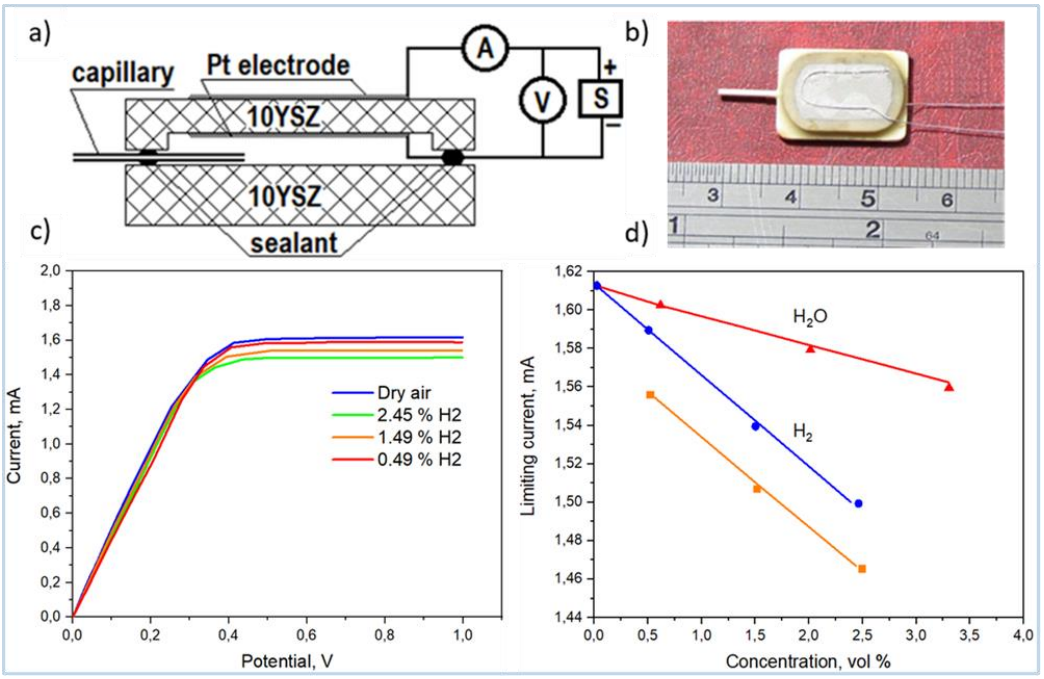

Figure 15: **a)** The configuration of the amperometric sensor for the detection of hydrogen and steam in atmospheric air [210]; **b)** A photograph of the manufactured sensor along with a ruler for the estimation of its dimensions [210]; **c)** V-I curves of the amperometric sensor for the H_2 + dry air mixture plotted at different hydrogen concentrations [210] and **d)** The limiting current plotted against the hydrogen concentration (triangles) in dry air, steam concentration (circles) in air and the hydrogen concentration in the humidified mixture (3.3 %) of H_2 + air [210].

In **Figure 15c**, the obtained V-I curves of the sensor for the gas mixture of hydrogen and dry air are demonstrated for different hydrogen concentrations. As shown, the limiting current area of all the analyzed hydrogen concentrations appears at 0.4 V. The values of limiting current for the examined hydrogen concentrations have subtle differences. Thus, more accurate measurements of limiting currents are required. Analogous measurements were carried out for different steam concentrations in the air, reporting the same behavior in V-I curves. In **Figure 15d**, the limiting current is plotted against the concentration of hydrogen (circles) and steam (rectangles). As can be seen, the limiting current dependence on the concentration of hydrogen is stronger than that on the steam concentration. In addition, the limiting current dependence of the H_2+air mixture (tringles) containing a known amount of humidity (3.3%) is shown. The experimental data expressed by the

symbols are in good agreement with the theoretical data (straight lines) calculated by the following equation [210],

$$I_{lim}(X_{O_2}) = I_{lim}(X^0_{O_2})\frac{X_{O_2}}{X^0_{O_2}} \quad (8.18)$$

8.4 Conclusions

In the present chapter, the electrochemical hydrogen sensors equipped with solid oxide electrolytes are reviewed. The discussed sensors are able to operate at high temperatures using solid electrolytes based on oxygen ion and proton conducting materials. Potentiometric hydrogen sensors, including equilibrium potentiometric and mixed potential sensors, are reported. The majority of studies on these sensors use the well-established oxygen ion conductor YSZ as a solid electrolyte combined with different selective oxide electrodes. On the other hand, amperometric hydrogen sensors using proton-conducting electrolytes are gaining significant attention as, contrary to potentiometric sensors, they don't need a reference atmosphere for their operation.

More precisely, the proton conducting materials $CaZr_{0.9}Sc_{0.10}O_3$ and $La_{0.95}Sr_{0.05}YO_3$ were used in an amperometric hydrogen sensor operating at 850°C for the detection of low (0.5-5%) and high (up to 100%) hydrogen concentrations, respectively. In 2016, the proton conductor, $La_{0.9}Sr_{0.1}YO_3$, was synthesized and tested in an amperometric hydrogen sensor in conjunction with YSZ electrolyte. This sensor operates at 500-600°C, detecting hydrogen in low concentrations (0.1-3.3 vol%). Later in the same year, a combined amperometric-potentiometric sensor based on $BaCe_{0.7}Zr_{0.1}Y_{0.2}O_{3-\delta}$ was designed and manufactured for hydrogen detection in nitrogen. This sensor can successfully detect hydrogen content (0.1-10 vol%) at 450-550°C. Recently, a sensor working under the amperometric regime was constructed and tested for the detection of steam and hydrogen in atmospheric air. The oxygen ion conductor 10YSZ was used in this sensor which can operate at 700°C. The abovementioned sensors are presented in **Table 2**.

Table 2: Electrochemical gas sensor based on oxygen-ion and proton-conducting solid electrolytes.

Type	Target gas	Temperature°C	Electrolyte	Year	Refs
Amperometric	H_2	850	$CaZr_{0.9}Sc_{0.1}O_3$	2014	[177]
Amperometric	H_2	850	$La_{0.95}Sr_{0.05}YO_3$	2014	[177]
Amperometric	H_2	500-600	$La_{0.9}Sr_{0.1}YO_{3-\delta}$	2016	[151]
Combined	H_2	450-550	$BaCe_{0.7}Zr_{0.1}Y_{0.2}O_{3-\delta}$	2016	[201]
Amperometric	H_2, H_2O	700	10YSZ	2022	[210]

References

1. Dhall, S., Mehta, B. R., Tyagi, A. K., Sood, K. A review on environmental gas sensors: Materials and technologies. *Sensors International*, 2021, *2*, 100116.
2. Liu, Y., Parisi, J., Sun, X., Lei, Y. Solid-state gas sensors for high temperature applications–a review. *Journal of Materials Chemistry A*, 2014, *2*(26), 9919-9943.
3. Ciobanu, M., Wilburn, J. P., Krim, M. L., Cliffel, D. E. *Fundamentals. Handbook of Electrochemistry*, 2007, *3–29*.
4. Ebbing, D., Gammon, S. D. Electrochemistry. *General chemistry*. 9th Edition, Houghton Mifflin Company, 770-819, 2007.
5. Perez, N. (Ed.). *Electrochemistry and corrosion science*. Boston, MA: Springer Us, 2004.
6. He, W., Lv, W., Dickerson, J. H. Gas diffusion mechanisms and models. In *Gas Transport in Solid Oxide Fuel Cells*, Springer, Cham, 2014, pp. 9-17.
7. Rickert, H. *Electrochemistry of solids: an introduction* (Vol. 7). Springer Science & Business Media, 2012.
8. Bruce, P. G. (Ed.). *Solid state electrochemistry* (No. 5). Cambridge university press, 1997.
9. Knauth, P., Tuller, H. L. Solid-state ionics: roots, status, and future prospects. *Journal of the American Ceramic Society*, 2002, *85*(7), 1654-1680.
10. Funke, K. Solid State Ionics: from Michael Faraday to green energy—the European dimension. *Science and Technology of Advanced Materials*, 2013, *14*(4), 043502.
11. Möbius, H. H. On the history of solid electrolyte fuel cells. *Journal of solid state electrochemistry*, 1997, *1*(1), 2-16.
12. Kiukkola, K., Wagner, C. Measurements on galvanic cells involving solid electrolytes. *Journal of the Electrochemical Society*, 1957, *104*(6), 379.
13. Kiukkola, K., Wagner, C. Galvanic cells for the determination of the standard molar free energy of formation of metal halides, oxides, and sulfides at elevated temperatures. *Journal of the electrochemical society*, 1957, *104*(5), 308.
14. Weissbart, J., Ruka, R. Oxygen gauge. *Review of Scientific Instruments*, 1961, *32*(5), 593-595.
15. Yao, Y. F. Y., ummer, J. T. Ion exchange properties of and rates of ionic diffusion in beta-alumina. *Journal of Inorganic and Nuclear Chemistry*, 1967, *29*(9), 2453-2475.
16. Virkar, A. N., Maiti, H. S. Oxygen ion conduction in pure and yttria-doped barium cerate. *Journal of power sources*, 1985, *14*(4), 295-303.

17. Mitsui, A., Miyayama, M., Yanagida, H. Evaluation of the activation energy for proton conduction in perovskite-type oxides. *Solid State Ionics*, 1987, *22*(2-3), 213-217.
18. Medvedev, D., Brouzgou, A., Demin, A., Tsiakaras, P. Proton-Conducting Electrolytes for Solid Oxide Fuel Cell Applications. In *Advances in Medium and High Temperature Solid Oxide Fuel Cell Technology*, Springer, Cham, 2017, pp. 77-118.
19. Chloros, D. *Electrochemical gas sensors based on solid electrolytes*. PhD Thesis. University of Thessaly, 2021.
20. Goodenough, J. B. Ceramic solid electrolytes. *Solid State Ionics*, 1997, *94*(1-4), 17-25.
21. Kharton, V. V., Marques, F. M. B., Atkinson, A. Transport properties of solid oxide electrolyte ceramics: a brief review. *Solid State Ionics*, 2004, *174*(1-4), 135-149.
22. Park, C. O., Akbar, S. A., Weppner, W. Ceramic electrolytes and electrochemical sensors. *Journal of Materials science*, 2003, *38*(23), 4639-4660.
23. Preux, N., Rolle, A., Vannier, R. N. Electrolytes and ion conductors for solid oxide fuel cells (SOFCs). In *Functional Materials for Sustainable Energy Applications*, Woodhead Publishing, 2012, pp. 370-401.
24. Smart, L., Moore, E., *Solid State Chemistry: An Introduction*., 3rd edition, CRC Press, 2005.
25. Kumar, P. P., Yashonath, S. Ionic conduction in the solid state. *Journal of Chemical Sciences*, 2006, *118*(1), 135-154.
26. Vouzavalis, A., Georgantas, S., *Fabrication and characterization of electrochemical ammonia sensors*, Dissertation, University of Thessaly, 2018.
27. Skinner, S. J., Kilner, J. A. Oxygen ion conductors. *Materials Today*, 2003, *6*(3), 30-37.
28. Goodenough, J. B. Oxide-ion conductors by design. *Nature*, 2000, *404*(6780), 821-823.
29. Kochetova, N., Animitsa, I., Medvedev, D., Demin, A., Tsiakaras, P. Recent activity in the development of proton-conducting oxides for high-temperature applications. *Rsc Advances*, 2016, *6*(77), 73222-73268.
30. Ota, K. I., Kreysa, G., Savinell, R. F. (Eds.). *Encyclopedia of applied electrochemistry*. New York: Springer, 2014.
31. Liu, T., Zhang, X., Wang, X., Yu, J., Li, L. A review of zirconia-based solid electrolytes. *Ionics*, 2016, *22*(12), 2249-2262.
32. Smith, Q. B. Impedance Spectroscopy Studies of Yttria Stabilized Zirconia Under Extreme Conditions, 2016.

33. Guan, S. H., Shang, C., Liu, Z. P. Resolving the temperature and composition dependence of Ion conductivity for yttria-stabilized zirconia from machine learning simulation. *The Journal of Physical Chemistry C*, 2020, *124*(28), 15085-15093.
34. Zakaria, Z., Kamarudin, S. K. Advanced modification of scandia-stabilized zirconia electrolytes for solid oxide fuel cells application—A review. *International Journal of Energy Research*, 2021, *45*(4), 4871-4887.
35. Jaiswal, N., Tanwar, K., Suman, R., Kumar, D., Upadhyay, S., Parkash, O. A brief review on ceria based solid electrolytes for solid oxide fuel cells. *Journal of Alloys and Compounds*, 2019, *781*, 984-1005.
36. Pikalova, E. Y., Murashkina, A. A., Maragou, V. I., Demin, A. K., Strekalovsky, V. N., Tsiakaras, P. E. CeO2 based materials doped with lanthanides for applications in intermediate temperature electrochemical devices. *international journal of hydrogen energy*, 2011, *36*(10), 6175-6183.
37. Wang, F. Y., Wan, B. Z., Cheng, S. Study on Gd 3+ and Sm 3+ co-doped ceria-based electrolytes. *Journal of Solid State Electrochemistry*, 2005, *9*(3), 168-173.
38. Ishihara, T., Matsuda, H., Takita, Y. Doped LaGaO3 perovskite type oxide as a new oxide ionic conductor. *Journal of the American chemical society*, 1994, *116*(9), 3801-3803.
39. Ishihara, T., Matsuda, H., bin Bustam, M. A., Takita, Y. Oxide ion conductivity in doped Ga based perovskite type oxide. *Solid State Ionics*, 1996, *86*, 197-201.
40. Ishihara, T., Honda, M., Shibayama, T., Minami, H., Nishiguchi, H., Takita, Y. Intermediate Temperature Solid Oxide Fuel Cells Using a New LaGaO3 Based Oxide Ion Conductor: I. Doped as a New Cathode Material. *Journal of the Electrochemical Society*, 1998, *145*(9), 3177.
41. Garche, J., Dyer, C. K., Moseley, P. T., Ogumi, Z., Rand, D. A., Scrosati, B. (Eds.). *Encyclopedia of electrochemical power sources*. Newnes, 2013.
42. Kendrick, E., Islam, M. S., Slater, P. R. Developing apatites for solid oxide fuel cells: insight into structural, transport and doping properties. *Journal of Materials Chemistry*, 2007, *17*(30), 3104-3111.
43. Singh, B., Ghosh, S., Aich, S., Roy, B. Low temperature solid oxide electrolytes (LT-SOE): A review. *Journal of Power Sources*, 2017, *339*, 103-135.
44. Lacorre, P., Goutenoire, F., Bohnke, O., Retoux, R., Laligant, Y. Designing fast oxide-ion conductors based on La2Mo2O9. *Nature*, 2000, *404*(6780), 856-858.

45. Goutenoire, F., Isnard, O., Retoux, R., Lacorre, P. Crystal structure of La2Mo2O9, a new fast oxide− ion conductor. *Chemistry of materials*, 2000, *12*(9), 2575-2580.
46. Singh, B., Ghosh, S., Aich, S., Roy, B. Low temperature solid oxide electrolytes (LT-SOE): A review. *Journal of Power Sources*, 2017, *339*, 103-135.
47. Medvedev, D. A., Lyagaeva, J. G., Gorbova, E. V., Demin, A. K., Tsiakaras, P. Advanced materials for SOFC application: Strategies for the development of highly conductive and stable solid oxide proton electrolytes. *Progress in Materials Science*, 2016, *75*, 38-79.
48. Medvedev, D., Murashkina, A., Pikalova, E., Demin, A., Podias, A., Tsiakaras, P. BaCeO3: Materials development, properties and application. *Progress in materials science*, 2014, *60*, 72-129.
49. Gorbova, E., Maragou, V., Medvedev, D., Demin, A., Tsiakaras, P. Influence of Cu on the properties of gadolinium-doped barium cerate. Journal of Power Sources, 2008, *181*(2), 292-296.
50. Gorbova, E., Maragou, V., Medvedev, D., Demin, A., Tsiakaras, P. Influence of sintering additives of transition metals on the properties of gadolinium-doped barium cerate. *Solid State Ionics*, 2008, *179*(21-26), 887-890.
51. Lagaeva, J., Medvedev, D., Demin, A., Tsiakaras, P. Insights on thermal and transport features of BaCe0. 8− xZrxY0. 2O3− δ proton-conducting materials. *Journal of Power Sources*, 2015, *278*, 436-444.
52. Medvedev, D., Maragou, V., Pikalova, E., Demin, A., Tsiakaras, P. Novel composite solid state electrolytes on the base of BaCeO3 and CeO2 for intermediate temperature electrochemical devices. Journal of Power Sources, 2013, *221*, 217-227.
53. Volkov, A., Gorbova, E., Vylkov, A., Medvedev, D., Demin, A., Tsiakaras, P. Design and applications of potentiometric sensors based on proton-conducting ceramic materials. A brief Review. *Sensors and Actuators B: Chemical*, 2017, *244*, 1004-1015.
54. Mehrer, H. Fast ion conductors. *Diffusion in Solids: Fundamentals, Methods, Materials, Diffusion-Controlled Processes*, 2007, 475-490.
55. Kim, J. J., Yoon, K., Park, I., Kang, K. Progress in the Development of Sodium-Ion Solid Electrolytes. *Small Methods*, 2017, *1*(10), 1700219.
56. Zhang, Y., He, X., Chen, Z., Bai, Q., Nolan, A. M., Roberts, C. A., Banerjee, D., Matsunaga, T., Mo, Y., Ling, C. Unsupervised discovery of solid-state lithium ion conductors. *Nature communications*, 2019, *10*(1), 1-7.

57. Giorgi, L., Leccese, F. Fuel cells: Technologies and applications. *The Open Fuel Cells Journal*, 2013, *6*(1).
58. Barbir, F. Introduction. *PEM Fuel Cells*, 2nd edition, Academic Press, 1–16, 2013.
59. Abdelkareem, M. A., Elsaid, K., Wilberforce, T., Kamil, M., Sayed, E. T., Olabi, A. Environmental aspects of fuel cells: A review. *Science of the Total Environment*, 2021, *752*, 141803.
60. Wang, J., Wang, H., Fan, Y. Techno-economic challenges of fuel cell commercialization. *Engineering*, 2018, *4*(3), 352-360.
61. Brouzgou, A., Song, S. Q., Tsiakaras, P. Low and non-platinum electrocatalysts for PEMFCs: Current status, challenges and prospects. *Applied Catalysis B: Environmental*, 2012, *127*, 371-388.
62. Wu, R., Tsiakaras, P., Shen, P. K. Facile synthesis of bimetallic Pt-Pd symmetry-broken concave nanocubes and their enhanced activity toward oxygen reduction reaction. *Applied Catalysis B: Environmental*, 2019, *251*, 49-56.
63. Brouzgou, A., Seretis, A., Song, S., Shen, P. K., Tsiakaras, P. CO tolerance and durability study of PtMe (Me= Ir or Pd) electrocatalysts for H2-PEMFC application. *International Journal of Hydrogen Energy*, 2021, *46*(26), 13865-13877.
64. Zhu, X., Huang, L., Wei, M., Tsiakaras, P., Shen, P. K. Highly stable Pt-Co nanodendrite in nanoframe with Pt skin structured catalyst for oxygen reduction electrocatalysis. *Applied Catalysis B: Environmental*, 2021, *281*, 119460.
65. Wang, K., Chen, H., Zhang, X., Tong, Y., Song, S., Tsiakaras, P., Wang, Y. Iron oxide@ graphitic carbon core-shell nanoparticles embedded in ordered mesoporous N-doped carbon matrix as an efficient cathode catalyst for PEMFC. *Applied Catalysis B: Environmental*, 2020, *264*, 118468.
66. Chen, Q., Chen, Z., Ali, A., Luo, Y., Feng, H., Luo, Y., Tsiakaras, P., Shen, P. K. Shell-thickness-dependent Pd@ PtNi core–shell nanosheets for efficient oxygen reduction reaction. *Chemical Engineering Journal*, 2022, *427*, 131565.
67. Najam, T., Shah, S. S. A., Ibraheem, S., Cai, X., Hussain, E., Suleman, S., Javed, M. S., Tsiakaras, P. Single-atom catalysis for zinc-air/O2 batteries, water electrolyzers and fuel cells applications. *Energy Storage Materials*, 2022, *45*, 504-540.
68. Molochas, C., Tsiakaras, P. Carbon Monoxide Tolerant Pt-Based Electrocatalysts for H2-PEMFC Applications: Current Progress and Challenges. *Catalysts*, 2021, *11*(9), 1127.

69. Song, S., Maragou, V., Tsiakaras, P. How far are direct alcohol fuel cells from our energy future?. *Journal of Fuel Cell Science and Technology*, 2007, *4*, 203-209.
70. Brouzgou, A., Tzorbatzoglou, F., Tsiakaras, P. Direct alcohol fuel cells: challenges and future trends. In *Proceedings of the 2011 3rd International Youth Conference on Energetics (IYCE)* (pp. 1-6). IEEE, 2011, July.
71. Wang, Y., He, C., Brouzgou, A., Liang, Y., Fu, R., Wu, D., Tsiakaras, P., Song, S. A facile soft-template synthesis of ordered mesoporous carbon/tungsten carbide composites with high surface area for methanol electrooxidation. *Journal of Power Sources*, 2012, *200*, 8-13.
72. Andreadis, G. M., Podias, A. K. M., Tsiakaras, P. E. The effect of the parasitic current on the direct ethanol PEM fuel cell operation. *Journal of Power Sources*, 2008, *181*(2), 214-227.
73. Song, S., Tsiakaras, P. Recent progress in direct ethanol proton exchange membrane fuel cells (DE-PEMFCs). *Applied Catalysis B: Environmental*, 2006, *63*(3-4), 187-193.
74. Wang, K., Wang, Y., Liang, Z., Liang, Y., Wu, D., Song, S., Tsiakaras, P. Ordered mesoporous tungsten carbide/carbon composites promoted Pt catalyst with high activity and stability for methanol electrooxidation. *Applied Catalysis B: Environmental*, 2014, *147*, 518-525.
75. Goula, M. A., Kontou, S. K., Tsiakaras, P. E. Hydrogen production by ethanol steam reforming over a commercial Pd/γ-Al2O3 catalyst. *Applied Catalysis B: Environmental*, 2004, *49*(2), 135-144.
76. Demin, A. K., Tsiakaras, P. E., Sobyanin, V. A., Hramova, S. Y. Thermodynamic analysis of a methane fed SOFC system based on a protonic conductor. *Solid State Ionics*, 2002, *152*, 555-560.
77. Coutelieris, F. A., Douvartzides, S., Tsiakaras, P. The importance of the fuel choice on the efficiency of a solid oxide fuel cell system. *Journal of Power Sources*, 2003, *123*(2), 200-205.
78. Vayenas, C. G., Bebelis, S., Yentekakis, I. V., Tsiakaras, P., Karasali, H. Non-faradaic electrochemical modification of catalytic activity. *Platinum Metals Review*, 1990, *34*(3), 122-130.
79. Tsiakaras, P., Athanasiou, C., Marnellos, G., Stoukides, M., ten Elshof, J. E., Bouwmeester, H. J. Methane activation on a La0. 6Sr0. 4Co0. 8Fe0. 2O3 perovskite: Catalytic and electrocatalytic results. *Applied catalysis A: general*, 1998, *169*(2), 249-261.
80. Tsiakaras, P., Vayenas, C. G. Oxidative coupling of CH4 on Ag catalyst-electrodes deposited on ZrO2 (8 mol% Y2O3). *Journal of Catalysis*, 1993, *144*(1), 333-347.

81. Long, G. F., Wan, K., Liu, M. Y., Liang, Z. X., Piao, J. H., Tsiakaras, P. Active sites and mechanism on nitrogen-doped carbon catalyst for hydrogen evolution reaction. *Journal of Catalysis*, 2017, *348*, 151-159.
82. Palacin, M. R. Recent advances in rechargeable battery materials: a chemist's perspective. *Chemical Society Reviews*, 2009, *38*(9), 2565-2575.
83. Thackeray, M. M., Wolverton, C., Isaacs, E. D. Electrical energy storage for transportation—approaching the limits of, and going beyond, lithium-ion batteries. *Energy & Environmental Science*, 2012, *5*(7), 7854-7863.
84. Gulzar, U., Goriparti, S., Miele, E., Li, T., Maidecchi, G., Toma, A., De Angelis, F., Capiglia, C., Zaccaria, R. P. Next-generation textiles: from embedded supercapacitors to lithium ion batteries. *Journal of Materials Chemistry A*, 2016, *4*(43), 16771-16800.
85. Najam, T., Shah, S. S. A., Peng, L., Javed, M. S., Imran, M., Zhao, M. Q., Tsiakaras, P. Synthesis and nano-engineering of MXenes for energy conversion and storage applications: Recent advances and perspectives. *Coordination Chemistry Reviews*, 2022, *454*, 214339.
86. Shah, S. S., Najam, T., Brouzgou, A., Tsiakaras, P. Alkaline Oxygen Electrocatalysis for Fuel Cells and Metal–Air Batteries. *Encyclopedia of Electrochemistry: Online*, 2007, 1-28.
87. Liang, H., Gong, X., Jia, L., Chen, F., Rao, Z., Jing, S., Tsiakaras, P. Highly efficient Li-O2 batteries based on self-standing NiFeP@ NC/BC cathode derived from biochar supported Prussian blue analogues. *Journal of Electroanalytical Chemistry*, 2020, *867*, 114124.
88. Lyu, D., Yao, S., Ali, A., Tian, Z. Q., Tsiakaras, P., Shen, P. K. N, S Codoped Carbon Matrix-Encapsulated Co9S8 Nanoparticles as a Highly Efficient and Durable Bifunctional Oxygen Redox Electrocatalyst for Rechargeable Zn–Air Batteries. *Advanced Energy Materials*, 2021, *11*(28), 2101249.
89. Jing, S., Ding, P., Zhang, Y., Liang, H., Yin, S., Tsiakaras, P. Lithium-sulfur battery cathodes made of porous biochar support CoFe@ NC metal nanoparticles derived from Prussian blue analogues. *Ionics*, 2019, *25*(11), 5297-5304.
90. Jing, S., Zhang, Y., Chen, F., Liang, H., Yin, S., Tsiakaras, P. Novel and highly efficient cathodes for Li-O2 batteries: 3D self-standing NiFe@ NC-functionalized N-doped carbon nanonet derived from Prussian blue analogues/biomass composites. *Applied Catalysis B: Environmental*, 2019, *245*, 721-732.
91. Liang, H., Zhang, Y., Chen, F., Jing, S., Yin, S., Tsiakaras, P. A novel NiFe@ NC-functionalized N-doped carbon microtubule network derived from biomass as a highly efficient

3D free-standing cathode for Li-CO2 batteries. *Applied Catalysis B: Environmental*, 2019, *244*, 559-567.

92. Zhang, G., Shi, Y., Wang, H., Jiang, L., Yu, X., Jing, S., Xing, S., Tsiakaras, P. A facile route to achieve ultrafine Fe2O3 nanorods anchored on graphene oxide for application in lithium-ion battery. *Journal of Power Sources*, 2019, *416*, 118-124.
93. Li, C., Wang, Z. Y., He, Z. J., Li, Y. J., Mao, J., Dai, K. H., Cheng, Y., Zheng, J. C. An advance review of solid-state battery: Challenges, progress and prospects. *Sustainable Materials and Technologies*, 2021, e00297.
94. Kim, B. K., Sy, S., Yu, A., Zhang, J. Electrochemical supercapacitors for energy storage and conversion. *Handbook of clean energy systems*, 2015, 1-25.
95. Halper, M. S., Ellenbogen, J. C. Supercapacitors: A brief overview. *The MITRE Corporation, McLean, Virginia, USA*, 2006, *1*.
96. Pramitha, A., Raviprakash, Y. Recent developments and viable approaches for high-performance supercapacitors using transition metal-based electrode materials. *Journal of Energy Storage*, 2022, *49*, 104120.
97. Zhong, C., Deng, Y., Hu, W., Qiao, J., Zhang, L., Zhang, J. A review of electrolyte materials and compositions for electrochemical supercapacitors. *Chemical Society Reviews*, 2015, *44*(21), 7484-7539.
98. Yan, L., Zhang, B., Zhu, J., Li, Y., Tsiakaras, P., Shen, P. K. Electronic modulation of cobalt phosphide nanosheet arrays via copper doping for highly efficient neutral-pH overall water splitting. *Applied Catalysis B: Environmental*, 2020, *265*, 118555.
99. Brouzgou, A., Song, S., Tsiakaras, P. Carbon-supported PdSn and Pd3Sn2 anodes for glucose electrooxidation in alkaline media. *Applied Catalysis B: Environmental*, 2014, *158*, 209-216.
100. Choudhary, Y. S., Jothi, L., Nageswaran, G. Electrochemical characterization. In *Spectroscopic Methods for Nanomaterials Characterization*, Elsevier, 2017, pp. 19-54.
101. Liu, D., Song, Z., Cheng, S., Wang, Y., Saad, A., Deng, S., Shen, J., Huang, X., Cai, X., Tsiakaras, P. Mesoporous IrNiTa metal glass ribbon as a superior self-standing bifunctional catalyst for water electrolysis. *Chemical Engineering Journal*, 2022, *431*, 134210.
102. Zhang, B., Shan, J., Wang, W., Tsiakaras, P., Li, Y. Oxygen Vacancy and Core–Shell Heterojunction Engineering of Anemone-Like CoP@ CoOOH Bifunctional Electrocatalyst for Efficient Overall Water Splitting. *Small*, 2022, *18*(12), 2106012.

103. Cen, J., Jiang, E., Zhu, Y., Chen, Z., Tsiakaras, P., Shen, P. K. Enhanced electrocatalytic overall water splitting over novel one-pot synthesized Ru–MoO3-x and Fe3O4–NiFe layered double hydroxide on Ni foam. *Renewable Energy*, 2021, *177*, 1346-1355.
104. Yu, C., Lu, J., Luo, L., Xu, F., Shen, P. K., Tsiakaras, P., Yin, S. Bifunctional catalysts for overall water splitting: CoNi oxyhydroxide nanosheets electrodeposited on titanium sheets. *Electrochimica Acta*, 2019, *301*, 449-457.
105. Zhang, L., Lu, J., Yin, S., Luo, L., Jing, S., Brouzgou, A., Chen, J., Shen, P. K., Tsiakaras, P. One-pot synthesized boron-doped RhFe alloy with enhanced catalytic performance for hydrogen evolution reaction. *Applied Catalysis B: Environmental*, 2018, *230*, 58-64.
106. Yu, C., Xu, F., Luo, L., Abbo, H. S., Titinchi, S. J., Shen, P. K., Tsiakaras, P., Yin, S. Bimetallic Ni–Co phosphide nanosheets self-supported on nickel foam as high-performance electrocatalyst for hydrogen evolution reaction. *Electrochimica Acta*, 2019, *317*, 191-198.
107. Nnamchi, P. S., Obayi, C. S. *Electrochemical Characterization of Nanomaterials. Characterization of Nanomaterials*, 2018, *103–127*.
108. Guy, O. J., Walker, K.-A. D. *Graphene Functionalization for Biosensor Applications. Silicon Carbide Biotechnology*, 2016, *85–141*.
109. Elgrishi, N., Rountree, K. J., McCarthy, B. D., Rountree, E. S., Eisenhart, T. T., Dempsey, J. L. A practical beginner's guide to cyclic voltammetry. *Journal of chemical education*, 2018, *95*(2), 197-206.
110. Franklin, R. K., Martin, S. M., Strong, T. D., Brown, R. B. Chemical and Biological Systems: Chemical Sensing Systems for Liquids, 2016.
111. Mirceski, V., Skrzypek, S., Stojanov, L. Square-wave voltammetry. *ChemTexts*, 2018, *4*(4), 1-14.
112. Instruments, G. Basics of electrochemical impedance spectroscopy. *G. Instruments, Complex impedance in Corrosion*, 2007, 1-30.
113. Magar, H. S., Hassan, R. Y., Mulchandani, A. Electrochemical Impedance Spectroscopy (EIS): Principles, Construction, and Biosensing Applications. *Sensors*, 2021, *21*(19), 6578.
114. Park, S. M., Yoo, J. S. Peer reviewed: electrochemical impedance spectroscopy for better electrochemical measurements, 2003.
115. Denuault, G., Sosna, M., Williams, K. J. Classical experiments. In *Handbook of electrochemistry*, Elsevier, 2007, pp. 431-469.
116. Wang, S., Zhang, J., Gharbi, O., Vivier, V., Gao, M., Orazem, M. E. Electrochemical impedance spectroscopy. *Nature Reviews Methods Primers*, 2021, *1*(1), 1-21.

117. Balasubramani, V., Chandraleka, S., Rao, T. S., Sasikumar, R., Kuppusamy, M. R., Sridhar, T. M. Recent advances in electrochemical impedance spectroscopy based toxic gas sensors using semiconducting metal oxides. *Journal of The Electrochemical Society*, 2020, *167*(3), 037572.
118. Nikolic, J., Expósito, E., Iniesta, J., González-Garcia, J., Montiel, V. Theoretical concepts and applications of a rotating disk electrode. *Journal of Chemical Education*, 2000, *77*(9), 1191.
119. Bard, A. J., Faulkner, L. R. Fundamentals and applications. *Electrochemical methods*, 2001, *2*(482), 580-632.
120. Tan, A. D., Wang, Y. F., Fu, Z. Y., Tsiakaras, P., Liang, Z. X. Highly effective oxygen reduction reaction electrocatalysis: Nitrogen-doped hierarchically mesoporous carbon derived from interpenetrated nonporous metal-organic frameworks. *Applied Catalysis B: Environmental*, 2017, *218*, 260-266.
121. Long, B., Yang, H., Li, M., Balogun, M. S., Mai, W., Ouyang, G., Tong, Y., Tsiakaras, P., Song, S. Interface charges redistribution enhanced monolithic etched copper foam-based Cu2O layer/TiO2 nanodots heterojunction with high hydrogen evolution electrocatalytic activity. *Applied Catalysis B: Environmental*, 2019, *243*, 365-372.
122. Lu, J., Tang, Z., Luo, L., Yin, S., Shen, P. K., Tsiakaras, P. Worm-like S-doped RhNi alloys as highly efficient electrocatalysts for hydrogen evolution reaction. *Applied Catalysis B: Environmental*, 2019, *255*, 117737.
123. Jing, S., Wang, D., Yin, S., Lu, J., Shen, P. K., Tsiakaras, P. P-doped CNTs encapsulated nickel hybrids with flower-like structure as efficient catalysts for hydrogen evolution reaction. *Electrochimica acta*, 2019, *298*, 142-149.
124. Xu, P., Qiu, L., Wei, L., Liu, Y., Yuan, D., Wang, Y., Tsiakaras, P. Efficient overall water splitting over Mn doped Ni2P microflowers grown on nickel foam. *Catalysis Today*, 2020, *355*, 815-821.
125. Saad, A., Gao, Y., Owusu, K. A., Liu, W., Wu, Y., Ramiere, A., Guo, H., Tsiakaras, P., Cai, X. Ternary Mo2NiB2 as a superior bifunctional electrocatalyst for overall water splitting. *Small*, 2022, *18*(6), 2104303.
126. Liang, H., Chen, F., Zhang, M., Jing, S., Shen, B., Yin, S., Tsiakaras, P. Highly performing free standing cathodic electrocatalysts for Li-O2 batteries: CoNiO2 nanoneedle arrays supported on N-doped carbon nanonet. *Applied Catalysis A: General*, 2019, *574*, 114-121.
127. Dunyushkina, L. A., Pankratov, A. A., Gorelov, V. P., Brouzgou, A., Tsiakaras, P. Deposition and characterization of Y-doped CaZrO3 electrolyte film on a porous SrTi0. 8Fe0. 2O3-δ substrate. *Electrochimica Acta*, 2016, *202*, 39-46.

128. Peiris, N. *Microwave-assisted processing of solid materials for sustainable energy related electronic and optoelectronic applications* (Doctoral dissertation, Loughborough University), 2014.
129. Zhou, W., Apkarian, R., Wang, Z. L., Joy, D. Fundamentals of scanning electron microscopy (SEM). In *Scanning microscopy for nanotechnology*, Springer, New York, NY, 2006, pp. 1-40.
130. Lin, P. C., Lin, S., Wang, P. C., Sridhar, R. Techniques for physicochemical characterization of nanomaterials. *Biotechnology advances*, 2014, *32*(4), 711-726.
131. John, N., George, S. Raman spectroscopy. In *Spectroscopic methods for nanomaterials characterization*, Elsevier, 2017, pp. 95-127.
132. Kaliva, M., Vamvakaki, M. Nanomaterials characterization. In *Polymer Science and Nanotechnology*, Elsevier, 2020, pp. 401-433.
133. L'H, Y., Mireles, L. K. X-ray photoelectron spectroscopy (XPS) and time-of-flight secondary ion mass spectrometry (ToF SIMS). In *Characterization of polymeric biomaterials*, Woodhead Publishing, 2017, pp. 83-97.
134. Stevie, F. A., Donley, C. L. Introduction to x-ray photoelectron spectroscopy. *Journal of Vacuum Science & Technology A: Vacuum, Surfaces, and Films*, 2020, *38*(6), 063204.
135. Capone, S., Forleo, A., Francioso, L., Rella, R., Siciliano, P., Spadavecchia, J., Presicce, D. S., Taurino, A. M. Solid state gas sensors: state of the art and future activities. *Journal of optoelectronics and Advanced Materials*, 2003, *5*(5), 1335-1348.
136. Balkourani, G., Damartzis, T., Brouzgou, A., Tsiakaras, P. Cost effective synthesis of graphene nanomaterials for non-enzymatic electrochemical sensors for glucose: a comprehensive review. *Sensors*, 2022, *22*(1), 355.
137. Balkourani, G., Brouzgou, A., Archonti, M., Papandrianos, N., Song, S., Tsiakaras, P. Emerging materials for the electrochemical detection of COVID-19. *Journal of Electroanalytical Chemistry*, 2021, *893*, 115289.
138. Brouzgou, A., Gorbova, E., Wang, Y., Jing, S., Seretis, A., Liang, Z., Tsiakaras, P. Nitrogen-doped 3D hierarchical ordered mesoporous carbon supported palladium electrocatalyst for the simultaneous detection of ascorbic acid, dopamine, and glucose. *Ionics*, 2019, *25*(12), 6061-6070.
139. Yuan, X., Yuan, D., Zeng, F., Zou, W., Tzorbatzoglou, F., Tsiakaras, P., Wang, Y. Preparation of graphitic mesoporous carbon for the simultaneous detection of hydroquinone and catechol. *Applied Catalysis B: Environmental*, 2013, *129*, 367-374.

140. Nadargi, D. Y., Mulla, I. S., Suryavanshi, S. S. Tungsten Oxide Nanocomposites as High-Performance Gas Sensors: Factors Influencing the Sensor Performance. In *Functional Nanomaterials*, Springer, Singapore, 2020, pp. 1-18.
141. Demin, A., Gorbova, E., Brouzgou, A., Volkov, A., Tsiakaras, P. Chapter 6-Sensors based on solid oxide electrolytes. In *Solid Oxide-Based Electrochemical Devices;* La Faro, M., Ed.; Academic Press: Cambridge, MA, USA, 2020, pp. 167-215.
142. Yunusa, Z., Hamidon, M. N., Kaiser, A., Awang, Z. Gas sensors: a review. *Sens. Transducers*, 2014, *168*(4), 61-75.
143. Ali, F. A., Mishra, D. K., Nayak, R., Nanda, B. Solid-state gas sensors: sensing mechanisms and materials. *Bulletin of Materials Science*, 2022, *45*(1), 1-22.
144. Gorbova, E., Tzorbatzoglou, F., Molochas, C., Chloros, D., Demin, A., Tsiakaras, P. Fundamentals and Principles of Solid-State Electrochemical Sensors for High Temperature Gas Detection. *Catalysts*, 2021, *12*(1), 1.
145. Lagutin, A. S., Vasil'ev, A. A. Solid-State Gas Sensors. *Journal of Analytical Chemistry*, 2022, *77*(2), 131-144.
146. López-Gándara, C., Ramos, F. M., Cirera, A. YSZ-based oxygen sensors and the use of nanomaterials: a review from classical models to current trends. *Journal of Sensors*, 2009.
147. Okamoto, H., Obayashi, H., Kudo, T. Carbon monoxide gas sensor made of stabilized zirconia. *Solid State Ionics*, 1980, *1*(3-4), 319-326.
148. Liu, T., Zhang, X., Yuan, L., Yu, J. A review of high-temperature electrochemical sensors based on stabilized zirconia. *Solid State Ionics*, 2015, *283*, 91-102.
149. Ramaiyan, K. P., Mukundan, R. Editors' choice—review—recent advances in mixed potential sensors. *Journal of The Electrochemical Society*, 2020, *167*(3), 037547.
150. Yi, J., Han, H. Analysis of factors affecting response for mixed potential gas sensors. *Electrochimica Acta*, 2021, *379*, 138129.
151. Kalyakin, A., Lyagaeva, J., Medvedev, D., Volkov, A., Demin, A., Tsiakaras, P. Characterization of proton-conducting electrolyte based on La0. 9Sr0. 1YO3–δ and its application in a hydrogen amperometric sensor. *Sensors and Actuators B: Chemical*, 2016, *225*, 446-452.
152. Usui, T., Asada, A., Nakazawa, M., Osanai, H. Gas polarographic oxygen sensor using an oxygen/zirconia electrolyte. *Journal of the Electrochemical Society*, 1989, *136*(2), 534.

153. Morata, A., Dezanneau, G., Tarancon, A., Peiró, F., Morante, J. R. Novel design and preliminary results of YSZ electrolyte-based amperometric oxygen sensors. In *Conference on Electron Devices*, Taragona, Spain, (pp. 585-588). IEEE, 02-04 February 2005.
154. Kalyakin, A., Demin, A., Gorbova, E., Volkov, A., Tsiakaras, P. Combined amperometric-potentiometric oxygen sensor. *Sensors and Actuators B: Chemical*, 2020, *313*, 127999.
155. Koralli, P., Petropoulou, G., Mouzakis, D. E., Mousdis, G., Kompitsas, M. Efficient CO sensing by a CuO: Au nanocomposite thin film deposited by PLD on a Pyrex tube. *Sensors and Actuators A: Physical*, 2021, *332*, 113120.
156. Wang, Y., Ma, L., Li, W., Li, W., Liu, X. A high-temperature mixed potential CO gas sensor for in situ combustion control. *Journal of Materials Chemistry A*, 2020, *8*(38), 20101-20110.
157. Guillet, N., Lalauze, R., Pijolat, C. Oxygen and carbon monoxide role on the electrical response of a non-Nernstian potentiometric gas sensor; proposition of a model. *Sensors and Actuators B: Chemical*, 2004, *98*(2-3), 130-139.
158. Brosha, E. L., Mukundan, R., Brown, D. R., Garzon, F. H., Visser, J. H. Development of ceramic mixed potential sensors for automotive applications. *Solid State Ionics*, 2002, *148*(1-2), 61-69.
159. Zhang, X., Kohler, H., Schwotzer, M., Guth, U. Stability improvement of layered Au, Pt-YSZ mixed-potential gas sensing electrodes by cathodic polarization: Studies by steady state and dynamic electrochemical methods. *Sensors and Actuators B: Chemical*, 2021, *342*, 130065.
160. Di Bartolomeo, E., Grilli, M. L. YSZ-based electrochemical sensors: From materials preparation to testing in the exhausts of an engine bench test. *Journal of the European Ceramic Society*, 2005, *25*(12), 2959-2964.
161. Chevallier, L., Di Bartolomeo, E., Grilli, M. L., Mainas, M., White, B., Wachsman, E. D., Traversa, E. Non-Nernstian planar sensors based on YSZ with a Nb2O5 electrode. *Sensors and Actuators B: Chemical*, 2008, *129*(2), 591-598.
162. Chevallier, L., Di Bartolomeo, E., Grilli, M. L., Traversa, E. High temperature detection of CO/HCs gases by non-Nernstian planar sensors using Nb2O5 electrode. *Sensors and Actuators B: Chemical*, 2008, *130*(1), 514-519.
163. Brosha, E. L., Mukundan, R., Brown, D. R., Garzon, F. H. Mixed potential sensors using lanthanum manganate and terbium yttrium zirconium oxide electrodes. *Sensors and Actuators B: Chemical*, 2002, *87*(1), 47-57.

164. Brosha, E. L., Mukundan, R., Brown, D. R., Garzon, F. H., Visser, J. H., Zanini, M., Zhou. Z., Logothetis, E. M. CO/HC sensors based on thin films of LaCoO3 and La0. 8Sr0. 2CoO3− δ metal oxides. *Sensors and Actuators B: Chemical*, 2000, *69*(1-2), 171-182.
165. Tho, N. D., Huong, D. V., Ngan, P. Q., Thai, Thu, D. T. A., Thu, D. T., Tuoi, N. T. M., Toan, N. N., Giang, H. T. Effect of sintering temperature of mixed potential sensor Pt/YSZ/LaFeO3 on gas sensing performance. *Sensors and Actuators B: Chemical*, 2016, *224*, 747-754.
166. Fadeyev, G., Kalyakin, A., Gorbova, E., Brouzgou, A., Demin, A., Volkov, A., Tsiakaras, P. A simple and low-cost amperometric sensor for measuring H2, CO, and CH4. *Sensors and Actuators B: Chemical*, 2015, *221*, 879-883.
167. Kalyakin, A., Volkov, A., Dunyushkina, L. Solid-Electrolyte Amperometric Sensor for Simultaneous Measurement of CO and CO2 in Nitrogen. *Applied Sciences*, 2022, *12*(9), 4515.
168. Mulmi, S., Thangadurai, V. Editors' Choice—review—solid-state electrochemical carbon dioxide sensors: fundamentals, materials and applications. *Journal of The Electrochemical Society*, 2020, *167*(3), 037567.
169. Fergus, J. W. A review of electrolyte and electrode materials for high temperature electrochemical CO2 and SO2 gas sensors. *Sensors and Actuators B: Chemical*, 2008, *134*(2), 1034-1041.
170. Kalyakin, A. S., Medvedev, D. A., Volkov, A. N. Electrochemical sensors based on proton-conducting electrolytes for determination of concentration and diffusion coefficient of CO2 in inert gases. *Chemical Engineering Science*, 2021, *229*, 116046.
171. Korotcenkov, G., Han, S. D., Stetter, J. R. Review of electrochemical hydrogen sensors. *Chemical reviews*, 2009, *109*(3), 1402-1433.
172. Hübert, T., Boon-Brett, L., Black, G., Banach, U. Hydrogen sensors–a review. *Sensors and Actuators B: Chemical*, 2011, *157*(2), 329-352.
173. Yajima, T., Koide, K., Fukatsu, N., Ohashi, T., Iwahara, H. A new hydrogen sensor for molten aluminum. *Sensors and Actuators B: Chemical*, 1993, *14*(1-3), 697-699.
174. Schwandt, C., Fray, D. J. Hydrogen sensing in molten aluminium using a commercial electrochemical sensor. *Ionics*, 2000, *6*(3), 222-229.
175. Serret, P., Colominas, S., Reyes, G., Abellà, J. Characterization of ceramic materials for electrochemical hydrogen sensors. *Fusion engineering and design*, 2011, *86*(9-11), 2446-2449.
176. Zosel, J., Schiffel, G., Gerlach, F., Ahlborn, K., Sasum, U., Vashook, V., Guth, U. Electrode materials for potentiometric hydrogen sensors. *Solid State Ionics*, 2006, *177*(26-32), 2301-2304.

177. Kalyakin, A., Fadeyev, G., Demin, A., Gorbova, E., Brouzgou, A., Volkov, A., Tsiakaras, P. Application of Solid oxide proton-conducting electrolytes for amperometric analysis of hydrogen in H2+ N2+ H2O gas mixtures. *Electrochimica Acta*, 2014, *141*, 120-125.
178. Yajima, T., Koide, K., Takai, H., Fukatsu, N., Iwahara, H. Application of hydrogen sensor using proton conductive ceramics as a solid electrolyte to aluminum casting industries. *Solid State Ionics*, 1995, *79*, 333-337.
179. Li, Y., Wang, C., Zhang, Z., Wang, J. A Hydrogen Sensor Using SrCe0. 95Yb0. 05O3-α as Proton Conductor and YHx+ YH2− z as Reference Electrode for Determining Hydrogen Pressure in Solid Steel. *Journal of Materials Science & Technology*, 2010, *26*(10), 957-960.
180. Iwahara, H., Uchida, H., Ogaki, K., Nagato, H. Nernstian Hydrogen Sensor Using BaCeO3-Based, Proton-Conducting Ceramics Operative at 200°–900° C. *Journal of The Electrochemical Society*, 1991, *138*(1), 295.
181. Yajima, T., Iwahara, H., Koide, K., Yamamoto, K. CaZrO3-type hydrogen and steam sensors: trial fabrication and their characteristics. *Sensors and Actuators B: Chemical*, 1991, *5*(1-4), 145-147.
182. Okuyama, Y., Nagamine, S., Nakajima, A., Sakai, G., Matsunaga, N., Takahashi, F., Kimata, K., Oshima, T., Tsuneyoshi, K. Proton-conducting oxide with redox protonation and its application to a hydrogen sensor with a self-standard electrode. *RSC advances*, 2016, *6*(40), 34019-34026.
183. Vogel, A., Baier, G., Schüle, V. Non-Nernstian potentiometric zirconia sensors: screening of potential working electrode materials. *Sensors and Actuators B: Chemical*, 1993, *15*(1-3), 147-150.
184. Tan, Y., Tan, T. C. Characteristics and modeling of a solid state hydrogen sensor. *Journal of The Electrochemical Society*, 1994, *141*(2), 461.
185. Lu, G., Miura, N., Yamazoe, N. High-temperature hydrogen sensor based on stabilized zirconia and a metal oxide electrode. *Sensors and Actuators B: Chemical*, 1996, *35*(1-3), 130-135.
186. Miura, N., Sato, T., Anggraini, S. A., Ikeda, H., Zhuiykov, S. A review of mixed-potential type zirconia-based gas sensors. *Ionics*, 2014, *20*(7), 901-925.
187. Fadeyev, G., Kalyakin, A., Demin, A., Volkov, A., Brouzgou, A., Tsiakaras, P. Electrodes for solid electrolyte sensors for the measurement of CO and H2 content in air. *International journal of hydrogen energy*, 2013, *38*(30), 13484-13490.

188. Yamaguchi, M., Anggraini, S. A., Fujio, Y., Breedon, M., Plashnitsa, V. V., Miura, N. Selective hydrogen detection at high temperature by using yttria-stabilized zirconia-based sensor with coupled metal-oxide-based sensing electrodes. *Electrochimica acta*, 2012, *76*, 152-158.
189. Yamaguchi, M., Anggraini, S. A., Fujio, Y., Sato, T., Breedon, M., Miura, N. Stabilized zirconia-based sensor utilizing SnO2-based sensing electrode with an integrated Cr2O3 catalyst layer for sensitive and selective detection of hydrogen. *International journal of hydrogen energy*, 2013, *38*(1), 305-312.
190. Martin, L. P., Glass, R. S. Hydrogen sensor based on YSZ electrolyte and tin-doped indium oxide electrode. *Journal of the Electrochemical society*, 2005, *152*(4), H43.
191. Martin, L. P., Pham, A. Q., Glass, R. S. Electrochemical hydrogen sensor for safety monitoring. *Solid State Ionics*, 2004, *175*(1-4), 527-530.
192. Sekhar, P. K., Brosha, E. L., Mukundan, R., Nelson, M. A., Williamson, T. L., Garzon, F. H. Development and testing of a miniaturized hydrogen safety sensor prototype. *Sensors and Actuators B: Chemical*, 2010, *148*(2), 469-477.
193. Tang, Z., Li, X., Yang, J., Yu, J., Wang, J., Tang, Z. Mixed potential hydrogen sensor using ZnWO4 sensing electrode. *Sensors and Actuators B: Chemical*, 2014, *195*, 520-525.
194. Li, Y., Li, X., Tang, Z., Tang, Z., Yu, J., Wang, J. Hydrogen sensing of the mixed-potential-type MnWO4/YSZ/Pt sensor. *Sensors and Actuators B: Chemical*, 2015, *206*, 176-180.
195. Li, Y., Li, X., Tang, Z., Wang, J., Yu, J., Tang, Z. Potentiometric hydrogen sensors based on yttria-stabilized zirconia electrolyte (YSZ) and CdWO4 interface. *Sensors and Actuators B: Chemical*, 2016, *223*, 365-371.
196. Li, Y., Li, X., Wang, J., Jun, Y., Tang, Z. A cobalt tungstate compound sensing electrode for hydrogen detection based upon mixed-potential type sensors. *RSC advances*, 2017, *7*(5), 2919-2925.
197. Zhang, X., Liu, T., Yu, J., Gao, X., Jin, H., Wang, X., Wang, C. A limiting current oxygen sensor with La0. 8Sr0. 2 (Ga0. 8Mg0. 2) 1-x Fe x O3-δ dense diffusion barrier. *Journal of Solid State Electrochemistry*, 2017, *21*(5), 1323-1328.
198. Liu, T., Jin, H., Li, L., Yu, J. A novel method for preparing dense diffusion barrier limiting current oxygen sensor. *Journal of the American Ceramic Society*, 2018, *101*(4), 1537-1543.
199. Zhang, X., Liu, T., Zhang, H., Yu, J., Jin, H., Wang, X., Wang, C., Gao, X. Limiting current oxygen sensors with La0. 8Sr0. 2Ga0. 8Mg0. 2O3-δ electrolyte and La0. 8Sr0. 2 (Ga0. 8Mg0. 2) 1-x Co x O3-δ dense diffusion barrier. *Ionics*, 2018, *24*(3), 827-832.

200. Yang, W., Wang, L., Li, Y., Zhou, H., He, Z., Liu, H., Dai, L. A limiting current hydrogen sensor based on BaHf0. 8Fe0. 2O3-δ dense diffusion barrier and BaHf0. 7Sn0. 1In0. 2O3-δ protonic conductor. *Ceramics International*, 2022.
201. Kalyakin, A., Volkov, A., Lyagaeva, J., Medvedev, D., Demin, A., Tsiakaras, P. Combined amperometric and potentiometric hydrogen sensors based on BaCe0. 7Zr0. 1Y0. 2O3− δ proton-conducting ceramic. *Sensors and Actuators B: Chemical*, 2016, *231*, 175-182.
202. Yagi, H., Ichikawa, K. Humidity sensing characteristics of a limiting current type planar oxygen sensor for high temperatures. *Sensors and Actuators B: Chemical*, 1993, *13*(1-3), 92-95.
203. Iwahara, H., Uchida, H., Kondo, J. Galvanic cell-type humidity sensor using high temperature-type proton conductive solid electrolyte. *Journal of Applied Electrochemistry*, 1983, *13*(3), 365-370.
204. Katahira, K., Matsumoto, H., Iwahara, H., Koide, K., Iwamoto, T. A solid electrolyte steam sensor with an electrochemically supplied hydrogen standard using proton-conducting oxides. *Sensors and Actuators B: Chemical*, 2000, *67*(1-2), 189-193.
205. Taniguchi, N., Kuroha, T., Nishimura, C., Iijima, K. Characteristics of novel BaZr0. 4Ce0. 4In0. 2O3 proton conducting ceramics and their application to hydrogen sensors. *Solid State Ionics*, 2005, *176*(39-40), 2979-2983.
206. Kalyakin, A. S., Lyagaeva, J. G., Chuikin, A. Y., Volkov, A. N., Medvedev, D. A. A high-temperature electrochemical sensor based on CaZr0. 95Sc0. 05O3–δ for humidity analysis in oxidation atmospheres. *Journal of Solid State Electrochemistry*, 2019, *23*(1), 73-79.
207. Kalyakin, A. S., Volkov, A. N., Gorshkov, M. Y. An electrochemical sensor based on zirconia and calcium zirconate electrolytes for the inert gas humidity analysis. *Journal of the Taiwan Institute of Chemical Engineers*, 2020, *111*, 222-227.
208. Kalyakin, A. S., Danilov, N. A., Volkov, A. N. Determining humidity of nitrogen and air atmospheres by means of a protonic ceramic sensor. *Journal of Electroanalytical Chemistry*, 2021, *895*, 115523.
209. Medvedev, D., Kalyakin, A., Volkov, A., Demin, A., Tsiakaras, P. Electrochemical moisture analysis by combining oxygen-and proton-conducting ceramic electrolytes. *Electrochemistry Communications*, 2017, *76*, 55-58.
210. Kalyakin, A., Demin, A., Gorbova, E., Volkov, A., Tsiakaras, P., Sensor based on solid oxide electrolyte for measuring water-vapor and hydrogen content in air. Accepted for publication to the Journal of Solid State Ionics, 2022.